

Contact-Implicit Modeling and Simulation of a Snake Robot on Compliant and Granular Terrain

A Thesis Presented

by

Haroon Hublikar

to

The Department of Electrical and Computer Engineering

in partial fulfillment of the requirements

for the degree of

Master of Science

in

Electrical and Computer Engineering

Northeastern University

Boston, Massachusetts

December 2025

Contents

List of Figures	iii
List of Tables	v
List of Acronyms	vi
Acknowledgments	viii
Abstract	ix
1 Introduction	1
1.1 Background and Motivation	1
1.2 Overview of the COBRA Platform	4
1.2.1 Body Module Design	4
1.2.2 Head Module and Onboard Computation	6
1.2.3 Latching Mechanism	6
1.2.4 Electronics Architecture	6
1.2.5 Summary	6
1.3 Related Work	7
1.4 Thesis Contributions and Outline	10
1.4.1 Primary Contributions	10
1.4.2 Thesis Outline	11
2 Literature Review	12
3 Methodology	20
3.1 Modeling	21
3.2 Sidewinding Gait Analysis	25
3.3 MATLAB Simulink Simulation for Rigid Ground	26
3.4 Project Chrono	28
3.5 Setting up Project Chrono	29
3.6 Deformable SCM (Soil Contact Model)	30
3.7 SCM Terrain Mathematical Formulation	32
3.8 Empirical Parameters from Simulation Code	35

3.8.1	SCM Terrain and Soil Properties	36
3.8.2	Robot Geometry and Contact Material	38
3.8.3	Motion Control and Gait Execution	39
3.8.4	Numerical Solver and Visualization	39
3.9	Simulation Loop	40
3.10	Simulation Details	42
3.10.1	Core Components	42
3.10.2	Required Input Assets	43
3.10.3	Simulation Execution Pipeline	43
3.10.4	Logging and Output Data	43
3.11	Hardware Tests	44
3.11.1	Laboratory Rigid-Ground Experiments	44
3.11.2	Loose-Sand Experiments with Onboard VIO	45
3.11.3	Gaits and Test Conditions	47
3.11.4	Dataset Summary	47
3.12	Tumbling Gait Analysis	47
3.13	MATLAB Simulink Tumbling Model for Rigid Ground	49
3.14	Introduction to Project Chrono DEM-Engine	51
3.15	DEM Terrain Workflow	52
3.15.1	Simulation Workflow Overview	54
3.15.2	Particle-Particle Contact Mechanics	55
3.15.3	DEM Clump Types	56
3.16	DEM Terrain Mathematical Formulation	57
3.17	Empirical Parameters from Simulation Code	59
3.17.1	Material Parameters	60
3.17.2	Gravitational and World Settings	60
3.17.3	Particle-Based Terrain Settings	61
3.17.4	Time Integration Settings	62
3.17.5	Wheel Actuation in Tumbling Mode	62
3.17.6	Output Logging	62
3.18	Simulation Loop	63
3.19	Simulation Details	64
4	Results	66
4.1	Qualitative Gait Replication in Simulation	67
4.2	Contact Mechanics and Load Redistribution	68
4.3	Head Trajectory Comparisons	70
4.4	Summary of Findings	71
4.5	Tumbling Gait Results: Chrono DEM Engine	72
5	Conclusion	76
5.0.1	Future Work	77
5.0.2	Final Remarks	77

List of Figures

1.1	COBRA robot performing sidewinding motion across loose sandy terrain.	2
1.2	Overview of the COBRA hardware platform. (A) Full-body configuration showing alternating yawing and pitching joints across a 1.7 m serial chain. (B) Body module assembly including the Dynamixel XH540-W270-R servo, voltage regulator, and battery interface. (C) Exploded view of the head module illustrating the Jetson Orin NX computer, RealSense D435i RGB-D camera, latching mechanism, and electronics layout. (D) System electronics architecture with distributed power and data buses along the RS-485 daisy chain. <i>Image courtesy of Adarsh Salagame.</i> [16]	5
1.3	Gap function computation from the Master’s Project (April 2025), showing projection lines from each COBRA segment to the terrain surface for real-time distance and contact estimation.	9
3.1	Closeup view of robot sand surface interactions. <i>Image courtesy of Adarsh Salagame</i>	21
3.2	Hard-ground contact simulation results in MATLAB: normal and tangential force behavior during rigid surface interaction.	26
3.3	SCM simulation showing vertical deformation of terrain nodes under the COBRA robot during sidewinding. The mesh illustrates permanent soil depressions, shear displacement, and berm accumulation across multiple gait cycles.	31
3.4	Software architecture of the Chrono-based SCM simulation environment for COBRA.	42
3.5	Snapshots of the snake robot operating in rigid laboratory conditions using motion capture and on loose outdoor sand using onboard visual–inertial odometry. Both setups are used to benchmark the predicted behavior from rigid and deformable terrain simulations. <i>Image courtesy of Adarsh Salagame.</i>	45
3.6	Onboard sensing during loose-sand tests. The RGB stream, depth reconstruction, and the visual–inertial odometry pose estimation illustrate how robot motion is tracked in environments where external motion capture is not feasible. <i>Image courtesy of Adarsh Salagame.</i>	46
3.7	Comparison of terrain–interaction models during downhill tumbling. Left: Rigid inclined surface dominated by rotational inertia and hard impact. Center: Granular medium with depth-dependent sinkage and slip. Right: Compliant deformable material exhibiting spring–damper response and terrain reshaping due to mass wasting. <i>Image courtesy of Adarsh Salagame.</i> [16]	49

3.8	Conceptual dual-thread GPU architecture used by the DEM Engine. The Kinematic Thread supplies robot geometry and motion, while the Dynamic Thread resolves particle contacts and integrates the granular system. Inspired by [37].	53
3.9	Conceptual workflow of a DEM simulation including grain generation, clump instantiation, boundary settling, and motion prescription. Adapted from [37].	55
3.10	Conceptual representation of DEM particle contact mechanics, showing normal and tangential components of the interaction. Inspired by [37].	56
4.1	SCM simulation snapshots for Gait 1 (0.4 Hz). Blue shading highlights terrain depression caused by link loading. <i>Image courtesy of Adarsh Salagame.</i>	67
4.2	SCM simulation snapshots for Gait 2 (0.3 Hz). Increased amplitudes lead to greater sinkage and lateral soil displacement. <i>Image courtesy of Adarsh Salagame.</i>	67
4.3	Contact distribution over one gait cycle. Deformable terrain results in wider and more diffused loading regions.	68
4.4	Comparison of ground reaction forces. Deformable terrain decreases peak forces and spreads loading temporally.	69
4.5	Contact pressure and permanent terrain depression over a gait cycle in Chrono SCM. Node-level sinking and smoothing are visible.	70
4.6	Comparison of head trajectories for Gait 1. Rigid-ground simulations closely match rigid-ground experiments; SCM captures compliant-ground trends.	71
4.7	Normalized head trajectories over a gait cycle showing similar stationary and sweeping phases across all environments.	72
4.8	Chrono DEM simulation of COBRA tumbling downslope on loose granular terrain (24° inclination). Terrain deformation, mass-wasting, and body sinkage are visible. <i>Image courtesy of Adarsh Salagame.</i> [16]	73
4.9	Comparison of tumbling dynamics across three models: Simscape stiff ground (blue), Simscape compliant ground (green), and Chrono DEM granular terrain (magenta). DEM results replicate body sinkage, dissipative energy loss, and reduced impact impulses observed in real sand. <i>Image courtesy of Adarsh Salagame.</i> [16] . .	74

List of Tables

3.1	SCM deformable soil model parameters used in simulation.	36
-----	--	----

List of Acronyms

- COBRA** Crater Observing Bio-inspired Rolling Articulator. A snake-like articulated robotic platform designed for flexible locomotion and object interaction in complex environments.
- GJK** Gilbert-Johnson-Keerthi. A geometric algorithm used for computing the shortest distance between convex shapes, commonly applied in collision detection and contact estimation.
- IMU** Inertial Measurement Unit. A sensor module that measures acceleration and angular velocity, typically used for motion tracking and orientation estimation in robotics.
- KD** k-Dimensional. Refers to data structures such as KD-trees that organize points in k-dimensional space for efficient nearest-neighbor and spatial queries.
- RGB-D** Red-Green-Blue and Depth. Refers to combined visual and depth data captured by sensors like Intel RealSense, enabling perception of 3D structure and color.
- SLAM** Simultaneous Localization and Mapping. A technique that allows a robot to build a map of an unknown environment while simultaneously tracking its own location within that map.
- STL** Standard Tessellation Language. A widely used file format for 3D models that describes surface geometry using triangular facets, common in 3D printing and CAD.
- MPC** Model Predictive Control. An optimization-based control strategy that predicts future system behavior over a finite horizon and computes optimal control actions by solving a constrained optimization problem at each time step.
- VIO** Visual-Inertial Odometry. A state estimation technique that fuses visual features tracked across camera frames with inertial measurements to provide robust pose estimation, particularly effective when GPS is unavailable.
- SCM** Soil Contact Model. Chrono's physics-based deformable terrain model that simulates particle-body interactions using pressure-sinkage relationships and Janosi-Hanamoto shear stress formulation for granular media locomotion.
- ODE** Ordinary Differential Equations. Mathematical equations describing continuous-time system dynamics where state derivatives depend on current states and inputs, fundamental to modeling rigid-body robot dynamics.

- DAE** Differential Algebraic Equations. A system combining differential equations with algebraic constraints, essential for modeling mechanical systems with contact forces and kinematic constraints in robotics.
- LiPo** Lithium Polymer. Rechargeable battery technology using polymer electrolytes, offering high energy density and flexible form factors ideal for mobile robotics applications.
- DEM** Discrete Element Method. A numerical technique used to model and simulate the motion and interaction of large numbers of particles, commonly applied to granular media, soil mechanics, and contact-rich environments in robotics simulations (e.g., Chrono DEM).
- CUDA** Compute Unified Device Architecture. A parallel computing platform and programming model developed by NVIDIA, enabling general-purpose computation on GPUs for high-performance scientific simulation, robotics, and real-time perception workloads.
- URDF** Unified Robot Description Format. An XML-based representation used to describe the kinematic structure, physical properties, visuals, and collision geometry of robots for simulation and control in frameworks such as ROS and Chrono.
- VSG** Vulkan Scene Graph. A high-performance graphics rendering framework based on the Vulkan API, used in Chrono for efficient real-time terrain deformation and robot visualization.
- CPU** Central Processing Unit. The primary compute engine responsible for executing general-purpose instructions in robotic systems.
- GPU** Graphics Processing Unit. A parallel compute architecture optimized for high-throughput operations such as contact resolution and terrain simulation.

Acknowledgments

I would like to express my heartfelt gratitude to Prof. Alireza Ramezani, my thesis advisor, for his exceptional mentorship, continuous encouragement, and insightful guidance throughout my Master's research journey. His expertise has shaped my approach to scientific thinking and has been instrumental in the successful completion of this thesis. I would also like to thank all members of the Silicon Synapse Lab at Northeastern University for fostering a supportive and innovative research environment that made this journey both productive and enjoyable. I am especially grateful to Adarsh Salagame, who has been a tremendous source of guidance as both a collaborator and mentor. His leadership, technical contributions, and continuous support have been central to my growth as a researcher. I have learned a great deal from working alongside him, and I truly value the time and effort he has invested in helping me succeed. I extend my sincere appreciation to my thesis committee members, Prof. Seth Hutchinson and Prof. Derya Aksaray, for their constructive feedback and thoughtful discussions during the defense process. Their perspectives greatly strengthened the technical quality and clarity of this work. Finally, I am deeply grateful to my parents and family for their unconditional love, patience, and constant encouragement. Their belief in me has been my greatest source of motivation. This Thesis marks an important milestone in my academic and professional path, and I look forward to contributing further to the field of robotics.

Abstract

Contact-Implicit Modeling and Simulation of a Snake Robot on Compliant and Granular Terrain

by

Haroon Hublikar

Master of Science in Electrical and Computer Engineering

Northeastern University, December 2025

Dr. Alireza Ramezani, Adviser

This thesis presents a unified modeling and simulation framework for analyzing sidewinding and tumbling locomotion of the COBRA snake robot across rigid, compliant, and granular terrains. A contact-implicit formulation is used to model distributed frictional interactions during sidewinding, and validated through MATLAB Simscape simulations and physical experiments on rigid ground and loose sand. To capture terrain deformation effects, Project Chrono's Soil Contact Model (SCM) is integrated with the articulated multibody dynamics, enabling prediction of slip, sinkage, and load redistribution that reduce stride efficiency on deformable substrates. For high-energy rolling locomotion on steep slopes, the Chrono DEM Engine is used to simulate particle-resolved granular interactions, revealing soil failure, intermittent lift-off, and energy dissipation mechanisms not captured by rigid models. Together, these methods span real-time control-oriented simulation and high-fidelity granular physics. Results demonstrate that rigid-ground models provide accurate short-horizon motion prediction, while continuum and particle-based terrain modeling becomes necessary for reliable mobility analysis in soft and highly dynamic environments. This work establishes a hierarchical simulation pipeline that advances robust, terrain-aware locomotion for robots operating in challenging unstructured settings.

Chapter 1

Introduction

1.1 Background and Motivation

Locomotion in contact-rich environments remains a central challenge in modern robotics. Unlike wheeled or legged systems with discrete and typically well-structured contact events, snake robots generate propulsion through a continuous distribution of frictional interactions that vary along the body. These dense and highly coupled contacts make modeling and control nontrivial, yet they enable terrain-adaptive motion and access to confined spaces that are infeasible for more conventional platforms. As a result, snake robots have demonstrated significant potential in applications such as search and rescue [1], industrial inspection, medical procedures [2], and planetary exploration [3].

Beyond advancing limbless robot design, the study of snake locomotion also offers insights relevant to dexterous manipulation. Contact-rich locomotion and multi-fingered manipulation share a common requirement: coordinating many simultaneous or intermittent contacts while respecting nonpenetration and frictional constraints [4], [5], [6]. This duality has motivated research into unified, optimization-based frameworks capable of reasoning over large sets of possible contact states without predefined sequencing or timing.

However, most classical analyses of snake locomotion assume rigid terrain and Coulomb friction [7], [8], [9]. In real-world environments such as sand, soil, mud, or snow, the ground is deformable, compliant, and often particulate. In these conditions, terrain deformation and body motion are tightly coupled, leading to effects such as sinkage, slip, shear displacement, and resistive drag that rigid ground models fail to capture. Accurate modeling of this coupling is essential for enabling reliable locomotion in unstructured outdoor and exploratory environments where deforma-

bility dominates [10], [11].



Figure 1.1: COBRA robot performing sidewinding motion across loose sandy terrain.

The physics of granular media occupy a regime between solid and fluid mechanics, where particle contacts form and break dynamically, producing nonlinear resistance, hysteresis, and anisotropic force transmission. Modeling this behavior in a computationally tractable manner requires balancing physical realism with numerical stability. Compliant-contact formulations address this need by replacing hard complementarity constraints with spring–damper reactions. These approaches retain differentiability for optimization-based solvers while capturing first-order deformation effects such as penetration depth, shear lag, and energy dissipation, making them suitable for both motion analysis and control.

Recent advances in contact-implicit trajectory optimization (CITO) have demonstrated that contact dynamics can be embedded directly into the optimization problem [12], [13], [14]. Rather than representing contact as discrete mode transitions, CITO formulates forces and kinematics as continuous variables that evolve within constraints representing frictional, unilateral interaction.

Building on these ideas, our earlier IEEE RA-L 2026 paper (under review), titled “Contact-Implicit Modeling of Snake Robot Sidewinding on Compliant and Granular Terrain”, extended Moreau’s time-stepping differential inclusion framework [15] to incorporate compliant surface in-

CHAPTER 1. INTRODUCTION

teractions. In that work, normal and tangential contact forces were modeled using spring–damper relationships, enabling limited ground indentation (negative gap) and velocity-dependent damping within the contact manifold. This compliant extension supported simulation of sidewinding propulsion on deformable substrates and provided a unified structure for modeling locomotion across rigid, compliant, and granular terrains. Hardware experiments performed with the COBRA modular snake robot confirmed that even simplified compliant-ground models can recover key locomotion characteristics on sand, including phase-locked traction patterns and propagation of traveling-wave kinematics.

This thesis investigates two distinct locomotion modes demonstrated by the Crater Observing Bio-inspired Rolling Articulator (COBRA) robot, each requiring a different terrain modeling approach based on the level of ground deformation involved:

- **Sidewinding Gait:** analyzed using Simscape Multibody for rigid-ground behavior and Chrono Soil Contact Model (SCM) for compliant surface interaction, complemented by hardware experiments performed on both flat laboratory flooring and loose sand.
- **Tumbling Gait:** investigated using a MATLAB Simulink rigid-ground formulation together with particle-resolved granular simulations in the Chrono Discrete Element Method (DEM) Engine, capturing the high-energy, deep-substrate interactions characteristic of deformable particulate terrain.

While the compliant model captured critical qualitative behaviors such as sinkage and reduced stride length, it did not fully represent the distributed deformation and soil-pressure response modeled by Project Chrono’s Soil Contact Model (SCM). In earlier work, Chrono-based simulations were used primarily for validation, but the detailed simulation architecture, solver configuration, contact mechanics, and soil-parameter choices were not described in depth. This thesis closes that gap by presenting a complete account of the Chrono SCM setup, including soil formulation, the simulation pipeline, and the associated data-processing methods, in order to provide a higher-fidelity continuum-based terrain representation that supports locomotion modeling.

Beyond continuum-style compliance modeling, this thesis incorporates granular simulation using the Chrono DEM Engine (DEME). While SCM represents soft soil through a deformable surface mesh and empirical pressure sinkage laws, DEME resolves the terrain as a collection of discrete particles whose collisions generate frictional and normal reactions at the grain scale. This makes it possible to analyze sliding, toppling, and mass rearrangement during high-energy behaviors such as tumbling.

CHAPTER 1. INTRODUCTION

Together, SCM and DEME establish a dual-scale modeling strategy: SCM provides a computationally efficient approximation for steady sidewinding on deformable ground, whereas DEME offers high-fidelity evaluation of granular mechanics critical to tumbling stability and down-slope behavior. This combined framework supports a comprehensive investigation of how substrate mechanics affect propulsion, contact distribution, and locomotion robustness across both gait modalities, forming a core foundation for the analyses presented in this thesis.

1.2 Overview of the COBRA Platform

The robotic system studied in this thesis is the *Crater Observing Bioinspired Rolling Articulator (COBRA)*, a modular snake robot composed of twelve interconnected segments, including eleven actuated joints and a head payload module. The modules are arranged in an alternating yaw–pitch sequence, enabling the robot to generate coupled lateral and vertical curvatures along its 1.7 m structure. This kinematic configuration supports traveling-wave motions that underlie sidewinding and other gaits on rigid and deformable terrains [16].

1.2.1 Body Module Design

Each body module houses a Dynamixel XH540-W270-R servo motor enclosed within a Markforged Onyx composite housing that provides high stiffness and heat resistance. A PLA outer shell encloses the local electronics and facilitates cable routing. The module includes thrust bearings, washers, and a standardized joint-mating connector for mechanical continuity between adjacent links. Power is supplied by a 4S 850 mAh 75C Li-Po battery regulated through an LM2596 buck converter providing 14 V to each servo. The power and data lines run along an RS-485 bus, maintaining low-latency actuation and synchronized communication across all modules.

CHAPTER 1. INTRODUCTION

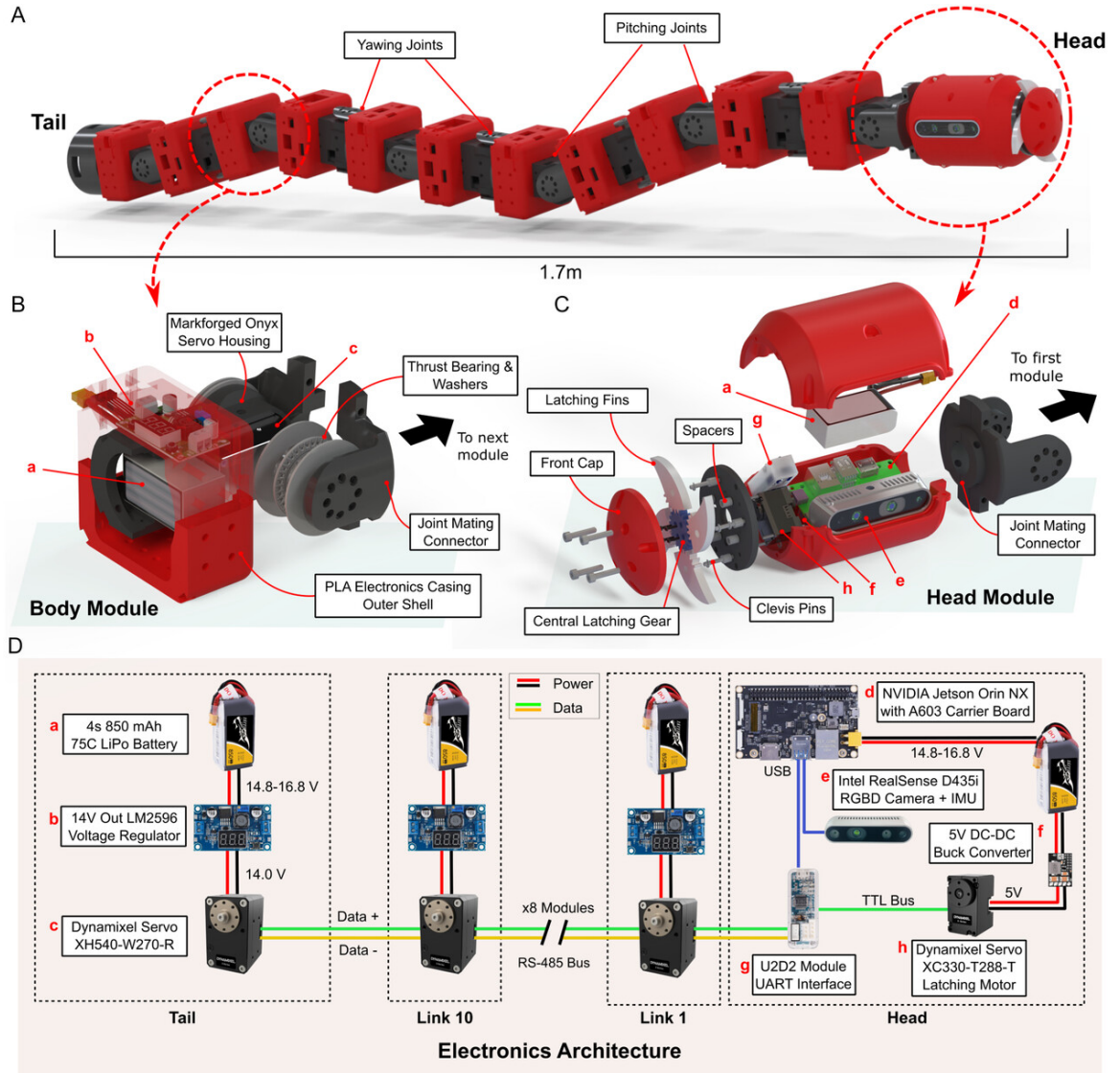


Figure 1.2: Overview of the COBRA hardware platform. (A) Full-body configuration showing alternating yawing and pitching joints across a 1.7 m serial chain. (B) Body module assembly including the Dynamixel XH540-W270-R servo, voltage regulator, and battery interface. (C) Exploded view of the head module illustrating the Jetson Orin NX computer, RealSense D435i RGB-D camera, latching mechanism, and electronics layout. (D) System electronics architecture with distributed power and data buses along the RS-485 daisy chain. *Image courtesy of Adarsh Salagame. [16]*

1.2.2 Head Module and Onboard Computation

The head module integrates computation, sensing, and an active latching mechanism. An NVIDIA Jetson Orin NX with an A603 carrier board executes high-level perception, planning, and control processes. It interfaces with the RS-485 network via a U2D2 USB-to-TTL interface and receives visual-inertial data from an Intel RealSense D435i camera, which provides RGB-D imagery and IMU readings for 6-DoF pose estimation and environment mapping. Power is distributed through a 5 V DC-DC buck converter and monitored across both computation and sensing subsystems.

1.2.3 Latching Mechanism

The head incorporates a compact mechanical latching system actuated by a Dynamixel XC330-T288-T servo. The mechanism employs a central latching gear that synchronously drives four latching fins, allowing the head to securely connect or release from other modules or environmental fixtures. This functionality enables modular reconfiguration, anchoring, and locomotion behaviors, such as transitioning between sidewinding and rolling (tumbling) gaits [16].

1.2.4 Electronics Architecture

The distributed electronics system connects all servos and sensors through a unified RS-485 communication bus (data) and a parallel 14 V power line (power). As shown in Fig. 1.2D, power is provided by a Li-Po source at the tail and regulated locally at each module. The architecture supports real-time operation at control frequencies up to 500 Hz, with feedback from servo encoders (position, velocity, and torque) and inertial sensors. This configuration enables precise gait control, real-time state estimation, and robust outdoor operation without reliance on external motion-capture systems.

1.2.5 Summary

In summary, the COBRA platform combines modular mechanical design, high-bandwidth distributed control, and integrated perception into a single architecture suitable for both terrestrial and extraterrestrial locomotion studies. Its combination of mechanical adaptability and computa-

tional autonomy makes it an effective testbed for developing and validating contact-implicit control and perception-driven planning algorithms on deformable terrains.

1.3 Related Work

The COBRA platform has undergone several generations of research that progressively expanded its capabilities in locomotion, modeling, perception, and terrain interaction. Early work demonstrated open-loop gait generation using coupled sinusoidal patterns across its alternating yaw–pitch joint structure, enabling sidewinding and lateral undulation on flat and moderately uneven terrain [7], [8], [17]. These studies showed that continuous traveling-wave motions can be produced reliably along a serially actuated body, highlighting the role of phase coordination, distributed contacts, and curvature modulation in achieving stable propulsion on rigid surfaces.

Further investigation extended COBRA to compliant surfaces and sloped environments. Experiments on loose sand and inclined terrain showed that distributed body contacts enable propulsion even when parts of the robot lose support, similar to biological sidewinders [18], [19]. These results emphasized how contact placement and load distribution influence normal forces, revealing that selective lifting of body segments improves traction and reduces slip on soft ground. This motivated the development of modeling frameworks capable of capturing the interplay between body curvature, contact distribution, and terrain yielding.

Research on snake robots more broadly has continued to expand in locomotion modeling, gait synthesis, and control. Foundational work established serpenoid curvature parametrization and coordinated phase-gait generation for hyper-redundant systems [9], [20], [21]. These principles were later adapted to obstacle-rich environments and manipulation tasks through methods that leveraged frictional interactions, redundancy resolution, and shape control [22], [23], [24], [25]. Rhythmic controllers, hybrid CPG–MPC approaches, and learning-based strategies further improved adaptation to uncertainty and environmental variation [2], [26], [27], [28], [29], [30], [31], [32].

Beyond snake robots, substantial work has focused on contact modeling, deformable terrain interaction, and motion planning under uncertainty. Proprioceptive contact estimation has shown strong performance in identifying multi-contact forces [33]. Efficient collision-geometry computation, including GJK and KD-tree search, supports fast distance queries for articulated bodies [34], [35], [36]. Research on granular locomotion highlights the effects of yielding terrain on propulsion, with particle-scale DEM studies [37], [38], tumbling robots on loose ground [11], and

CHAPTER 1. INTRODUCTION

planning algorithms aware of ground uncertainty [10]. Perception-driven mobility has advanced through visual–inertial SLAM and onboard estimation frameworks for cluttered or GPS-denied environments [39], [40], [41]. Terramechanics studies introduced continuum-based models such as SCM [42], [43], [44], [45] while DEM research emphasized grain-scale forces and mass wasting [46], [47]. Finally, theoretical progress in non-smooth mechanics and contact time-stepping formed the basis of modern simulation systems used in robotics [15], [48], [49], [50].

Work from the Silicon Synapse Lab builds directly on these foundations and extends them into multi-modal, contact-rich locomotion across legged, aerial, and serpentine platforms. Husky Carbon demonstrated posture manipulation and thrust-vectoring control for steep-slope and narrow-path locomotion [51], [52], [53], [54]. QP-based force regulation and stability controllers further strengthened locomotion robustness [55], [56], [57], [58]. Parallel work on the Harpy platform explored thruster-assisted bipedal locomotion, reduced-order models, and real-time momentum-based disturbance estimation [59], [60], [61].

Aerial robotics research in the Lab introduced Aerobat, a high-DOF morphing-wing vehicle capable of navigating confined environments through unsteady aerodynamic interactions [62], [63], [64]. This line of work expanded into neural and physics-informed aerodynamic models, contributing insights into maneuverability in dynamic morphing-wing flight [65], [66], [67], [68].

The Lab also advanced articulated and serpentine systems. Vision-guided loco-manipulation and large-scale navigation were demonstrated on snake robots operating in cluttered terrain [69], [70]. Contact-aware optimization frameworks were introduced for non-impulsive loco-manipulation [71], [72]. Learning-based methods improved terrain prediction and dynamic parameter identification [73], [74], [75]. COBRA-specific research examined granular physics, tumbling stability, and high-energy ground interaction [76], [77]. Additional work explored dynamic modeling and control for multi-modal planetary and transformable robots [78], [79], [80], [81].

Together, these efforts from the wider research community and the SS Lab form a cohesive body of knowledge that informs the modeling, perception, and control methods used in this thesis.

Finally, COBRA has also been used as a perception-enabled loco-manipulation testbed through the Master’s Project titled *Real-Time Gap Function Computation, Contact Estimation, and Object Pose Estimation for Snake Robots in Loco-Manipulation Tasks*. This system integrated FoundationPose-based tracking, SAM2 segmentation, and a geometry-based contact estimator relying on GJK [34] and KD-tree search [35]. Running onboard a Jetson Orin NX with visual–inertial sensing, this framework enabled real-time contact estimation that supports future contact-implicit planning.

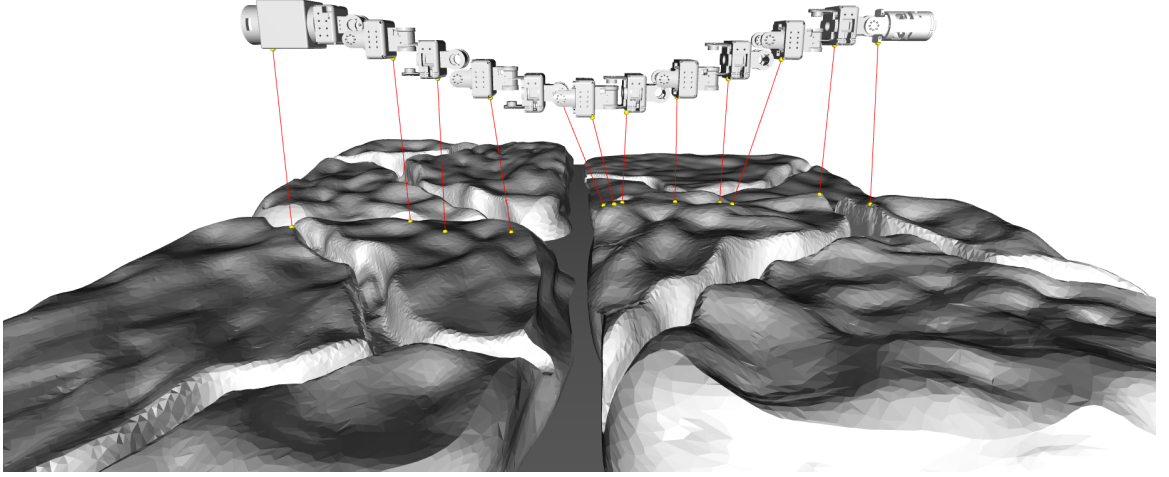


Figure 1.3: Gap function computation from the Master’s Project (April 2025), showing projection lines from each COBRA segment to the terrain surface for real-time distance and contact estimation.

Unlike earlier work that emphasized gait synthesis, perception, or hardware validation, this thesis focuses primarily on the modeling and simulation of snake-robot locomotion across deformable terrains. Specifically, it advances:

- The contact-implicit modeling framework for snake locomotion introduced in the RA-L 2026 study,
- The implementation and parameterization of SCM-based continuum simulations in Project Chrono, and
- The integration of particle-resolved DEM simulations for high-fidelity terrain interaction analysis.

Together, these components establish a unified computational framework for studying, validating, and extending contact-rich sidewinding locomotion across rigid, compliant, and granular environments.

1.4 Thesis Contributions and Outline

This thesis consolidates and deepens work on deformable-terrain locomotion for modular snake robots using the COBRA platform. While the core mathematical formulation of the contact-implicit locomotion model in our *IEEE RA-L* submission was developed by Adarsh Salagame in collaboration with Professor Alireza Ramezani, my primary contributions lie in (i) the creation of high-fidelity simulation environments in Project Chrono for compliant and granular terrain, (ii) extensive hardware data collection for validation, and (iii) integration of these components into a unified evaluation framework. These enable direct comparison of analytical modeling assumptions against physically grounded simulation and real-world performance.

1.4.1 Primary Contributions

1. **Project Chrono Simulation Software Development.** I built the Chrono-based simulation environment from the ground up, including custom configuration for GPU execution, collision model setup, and a modular simulation loop for loading the COBRA URDF, applying gait commands, resolving terrain interaction, and logging high-frequency state and contact data.
2. **Integration and Calibration of Chrono’s Soil Contact Model (SCM).** I incorporated SCM terrain into the COBRA simulation framework, tuned soil parameters using hardware sand experiments, and generated the compliant-surface datasets used for model comparison in the RA-L study.
3. **Simulation of Tumbling Locomotion Using Chrono DEME (AISJ 2025).** I implemented the DEM-based tumbling simulation used in the AISJ study, configuring granular terrain and slope settings to analyze particle-level resistance forces, sinkage, and flow behavior during multimodal locomotion.
4. **Hardware Data Collection and Simulation Validation.** I led the collection of experimental datasets used for validating the simulation models, including RGB-D + IMU data from COBRA on loose sand and motion-capture data on rigid ground. I also produced Chrono-based simulation datasets that were used to evaluate ground stiffness, contact patterns, and locomotion performance.

Together, these contributions provide the practical computational and experimental framework required to evaluate deformable-surface locomotion, forming the core foundation of this the-

sis.

1.4.2 Thesis Outline

The remainder of this thesis is structured as follows:

- **Chapter 1: Introduction** Presents the motivation behind studying snake-robot locomotion on diverse terrain types, provides an overview of the COBRA platform, reviews related work, and summarizes the thesis contributions and structure.
- **Chapter 2: Literature Review** Summarizes prior work on contact modeling, deformable terrain simulation, and relevant techniques in locomotion analysis for hyper-redundant robots.
- **Chapter 3: Methodology** Details the modeling and simulation frameworks used in this thesis. This includes:
 - the contact-implicit locomotion model used for sidewinding analysis,
 - MATLAB Simulink rigid-ground simulation for sidewinding,
 - Project Chrono SCM deformable-terrain simulation pipeline,
 - hardware experiment setup for validation,
 - MATLAB Simulink modeling for tumbling,
 - Chrono DEM-Engine granular simulation, including numerical contact mechanics and particle-based terrain generation.
- **Chapter 4: Results** Provides qualitative and quantitative comparison of simulation and hardware performance for sidewinding and tumbling gaits. Contact forces, slip behavior, sinkage, and locomotion efficiency are analyzed across rigid, compliant, and granular terrains.
- **Chapter 5: Conclusion** Summarizes key findings, discusses the relevance of the developed simulation frameworks, and outlines future directions including perception-enhanced control, adaptive terrain reasoning, and planetary field deployment.

Chapter 2

Literature Review

The development of sophisticated control systems for snake robots has progressed substantially through the integration of biologically inspired learning mechanisms, rhythmic control architectures, and modern optimization-based frameworks. Early research drawing inspiration from cerebellar learning demonstrated that adaptive internal models can improve serpentine coordination by continuously refining motion patterns in response to unexpected frictional variations or disturbances, thereby offering a foundation for agile and resilient locomotion [82]. Building on this perspective, Central Pattern Generator (CPG) frameworks introduced compact oscillatory structures capable of producing rich families of 3D slithering motions, and their tunability enabled smooth transitions between gaits along with real-time modulation of locomotion speed and direction [83]. As the community sought greater predictability and constraint awareness, simplified averaged representations of snake robot dynamics enabled Model Predictive Control (MPC) approaches capable of respecting inequality constraints, environmental interactions, and path-following requirements while still maintaining computational tractability [84]. More recent optimal control and data-driven methods have further pushed this direction by incorporating friction uncertainty estimation and efficient numerical solvers to achieve robust trajectory tracking even under unknown surface conditions [85]. Parallel efforts in amphibious robotics have shown that gradient-free online optimization can autonomously discover high-performance gaits in both swimming and crawling modes without detailed analytical models, providing strong evidence that learning and optimization can complement biological inspiration [86]. Nonlinear MPC (NMPC) studies have emphasized the importance of computational feasibility, revealing how constraint-handling frequency and update rates must align with the robot's intrinsic dynamics to ensure stable operation [87]. Reinforcement learning formulations using path integrals have offered an alternative means of generating smooth curvature

CHAPTER 2. LITERATURE REVIEW

sequences for crawler locomotion, yielding robust performance across diverse terrains [31]. Lastly, the integration of safe reinforcement learning with robust MPC has shown that high-performance adaptive controllers can be equipped with formal safety guarantees, helping advance snake robot locomotion toward real-world application domains [32]. Collectively, these studies trace a clear trajectory from biologically inspired control principles toward predictive and learning-based optimization frameworks that support adaptive and constraint-aware snake robot control.

The progress made in snake robot control also connects with a growing body of work focused on extraterrestrial mobility, where robots must navigate highly irregular and extreme environments. The frontier of planetary exploration has been significantly shaped by robotic systems capable of traversing complex terrains such as lunar craters, Martian regolith, and subsurface caves. A prominent example is the Crater Observing Bioinspired Rolling Articulater (COBRA), a multi-modal snake robot designed for variable lunar landscapes, where its ability to transition between slithering and tumbling locomotion provides unique mobility compared with wheeled platforms on steep crater slopes and loose sediments [16]. Complementary research on thruster-assisted legged mobility for Mars has demonstrated that small, strategically applied thrust forces can help maintain balance and enforce safety constraints in low-gravity environments, with reference governors ensuring reliable control during dynamic maneuvers [61]. The growing interest in aerial reconnaissance has led to parametric studies of Mars helicopters that clarify aerodynamic, mass, and geometric constraints necessary for stable flight in the thin Martian atmosphere [88]. Broad surveys of rotorcraft designs further highlight their value for high-resolution mapping, terrain scouting, and scientific support operations [89]. At the aerodynamic level, detailed analyses of coaxial rotors under Martian-relevant conditions have revealed how rotor spacing, interference mechanisms, and induced flow behavior influence lift and efficiency [90]. Earlier foundational work also provided critical insights into ultralight rotorcraft suitable for Martian exploration long before current missions [91]. Supporting geological studies have identified ridge-like Martian lava tubes with notable internal stability, highlighting their relevance for future exploration and habitation [92]. Along similar lines, numerical modeling of ice cave stability has revealed the persistence of buried ice reservoirs, guiding scientific interest toward subsurface environments with astrobiological significance [93]. Together, these contributions show a research landscape where planetary mobility increasingly relies on biologically inspired systems, hybrid locomotion strategies, and aerial capabilities that address extraterrestrial constraints.

Alongside these developments, machine learning has steadily reshaped how robots acquire adaptive behaviors, making it possible for controllers to improve performance directly from

CHAPTER 2. LITERATURE REVIEW

interaction data. Machine learning has introduced a transformative paradigm to robot control by enabling systems to learn robust behaviors directly from data and to adapt to unknown dynamics without relying only on handcrafted models. Online-learning-augmented MPC has shown that combining predictive modeling with policy refinement allows robots to preserve baseline stability while improving performance through real-world feedback [94]. In manipulation, Sim2Real strategies using tactile-based reinforcement learning have demonstrated that training on diverse simulated objects and contact scenarios can produce manipulation skills that transfer reliably to hardware, closing long-standing gaps between simulation and physical systems [95]. End-to-end learning applied to quadrupedal robotics has revealed that locomotion and local navigation can be jointly optimized in unified frameworks, allowing robots to traverse unstructured terrain using energy-efficient learned gaits that require minimal tuning [96]. For snake robots, Koopman operator-based MPC has shown that linear embeddings of nonlinear dynamics can support effective and model-free path following, extending predictive control methods to systems with complex body-terrain interactions [29]. Reinforcement learning integrated into scenario-tree MPC has allowed autonomous surface vehicles to reliably handle uncertainty in obstacle avoidance and pursuit tasks, illustrating the broader value of combining learning with predictive planning [97]. In surgical robotics, learning-based MPC approaches comparing reinforcement learning and imitation learning have highlighted the potential of data-driven control in delicate tissue manipulation tasks that demand safe but precise motions [2]. Collectively, these studies show that learning-enabled controllers can effectively complement predictive frameworks in robots operating in uncertain and dynamic environments.

Reliable autonomy depends not only on control and learning but also on the ability to understand and map the surrounding environment, which has driven rapid advances in SLAM and perception. The evolution of Simultaneous Localization and Mapping (SLAM) has been shaped by progress in semantic representation, perception-driven planning, and multisensor fusion. Real-time semantic SLAM for large-scale autonomous flight has shown that identifying high-level structures such as trunk clusters, canopy density, and ground planes improves navigation robustness in forested environments with poor visibility [98]. Visual-inertial SLAM frameworks using submapping approaches have extended this capability by supporting long-duration flight in GPS-denied environments through continuous re-localization and map refinement [99]. In high-speed navigation, adaptive search-based replanning has enabled drones to refine sampling resolution and update trajectories based on environmental complexity, which increases reliability during aggressive maneuvers [100]. For snake robots, perception-aware locomotion has employed onboard LiDAR to reconstruct local environments and support planning in confined and low-visibility conditions [101]. Classic

CHAPTER 2. LITERATURE REVIEW

work introducing the virtual chassis concept provided a simplified representation for snake robot deformation and control by defining a representative frame based on averaged link orientations, which enabled more interpretable and stable state estimation [8]. Laser-visual-inertial odometry has achieved extremely low drift over multi-kilometer trajectories, demonstrating the capability of tightly coupled multisensor fusion for precise navigation [39]. Stereo visual-inertial odometry using MSCKF methods has further shown that lightweight perception pipelines can support stable flight at speeds exceeding 17 meters per second [40]. The RAPPIDS planning framework added to this ecosystem by enabling efficient collision checks and trajectory generation from a single depth image, providing a practical tool for fast navigation through clutter [102]. Together, these works show a steady progression toward SLAM systems that are increasingly semantic, adaptive, and tightly integrated with planning.

Insights from biology further broaden the design space of robotics, showing how natural systems achieve efficient and adaptive motion across air, land, and complex terrain. The field of bio-inspired robotics has expanded significantly through detailed study of how animals achieve efficient, adaptive, and versatile locomotion. A notable example is the Bat Bot (B2), which demonstrated that articulated morphing wings with only a small number of actuators can reproduce the aeroelastic behavior necessary for stable and maneuverable bat-like flight [103]. Earlier biomechanical studies showed how bat wings feature coupled interactions between compliant skin, skeletal flexibility, and aerodynamic loading, suggesting that mechanical intelligence arises naturally from the synergy between morphology and actuation [104]. Principal component analysis applied to bat kinematic data identified dominant modes of biological motion and enabled robotic designs that replicate key aerodynamic effects while reducing actuation complexity [105]. Additional computational structure designs introduced armwing mechanisms capable of producing biologically meaningful flapping motions with relatively little mechanical overhead [106]. Inspired by reptiles, research on rolling locomotion has shown that manipulating the center of gravity can produce energy-efficient rolling motion, which is a promising complement to traditional undulatory gaits for snake-like robots [107]. Studies of helical gaits have shown that combining rolling and bending can enhance end-effector dexterity, allowing snake robots to perform complex manipulation tasks alongside locomotion [108]. Modular snake robots equipped with docking mechanisms have expanded operational capabilities by allowing robots to connect, extend their body, and increase available degrees of freedom [109]. Comparative dynamic analyses have shown that sinus-lifting and sidewinding gaits often provide better energy efficiency relative to lateral undulation, which informs gait selection for real-world applications [110]. Collectively, these works demonstrate how studying biological systems contin-

CHAPTER 2. LITERATURE REVIEW

ues to inspire new forms of mechanical intelligence and multifunctional locomotion.

Translating biological inspiration into physical machines requires strong attention to structure and mechanical design, especially for robots expected to operate in demanding or unfamiliar environments. Advanced structural analysis and mechanical design continue to shape modern robotic systems, particularly those intended for use in complex terrains. Geological investigations of lunar and Martian lava tubes have shown that large-scale voids, sometimes exceeding one kilometer in diameter, may remain structurally stable, which emphasizes the need for robotic platforms that can navigate subsurface structures. In aerial robotics, synergistic mechanical designs have combined biological insights with multi-body dynamic modeling to produce flapping-wing mechanisms that reproduce key aspects of bat flight kinematics and control [111]. Optimization-based frameworks have identified kinematic synergies that reduce the number of required actuators while preserving aerodynamic functionality, blending computational design with biologically inspired principles. In legged and hybrid robots, generative design methods have addressed the Mobility Value of Added Mass problem by optimizing morphology and structure to reduce transport cost while maintaining mechanical robustness [112]. The redesigned *Serpens* robot employs series elastic actuators and modular 3D-printed components to achieve compliance, robustness, and ease of assembly, representing a practical approach to scalable snake robot design [113]. Broader discussions of self-reconfigurable modular robots have highlighted rolling mechanisms inspired by the Golden Wheel Spider, which offer promising strategies for developing scalable and shape-changing planetary robots [114]. Multi-loop linkage robots have shown that closed-chain mechanical designs can achieve rolling and direction-switching capabilities without the need for sophisticated actuation or control [115]. Research on series elastic snake robots has also explored improved sensing, advanced actuation strategies, and the potential use of augmented reality to enhance teleoperation and situational awareness [116]. Together, these studies show how structural insight, mechanical intelligence, and modularity are shaping the next generation of resilient robotic platforms.

In parallel with ground and subterranean systems, aerial robots have seen major progress through improved dynamics modeling, real-time planning, and mechanically intelligent designs. The domain of autonomous aerial systems has advanced rapidly through improvements in perception, dynamic modeling, and real-time trajectory generation. The MIMIC framework showed that integrating mechanical intelligence into flapping-wing structures allows bat-like robots to perform agile and stable mid-air maneuvers, illustrating how embodied morphology can reduce control complexity [117]. Direct-collocation-based trajectory planning methods have enabled bat-inspired robots to execute feasible transitions and aerobatic motions while respecting aerodynamic and struc-

CHAPTER 2. LITERATURE REVIEW

tural constraints [118]. In legged locomotion, thruster-assisted balancing has shown that small controlled thrust pulses can prevent falls, enable traversal of challenging obstacles, and support high-dynamics maneuvers that would otherwise be infeasible [59]. Safe corridor planning for quadrotors has reframed trajectory generation as a constrained quadratic program, which provides real-time navigation through cluttered spaces with formal safety guarantees [119]. High-speed autonomous flight systems have demonstrated navigation at speeds above 18 meters per second in GPS-denied indoor and outdoor settings, supported entirely by onboard perception and computation [41]. RAPIDS contributed a lightweight planning method using single-depth-image collision checking, making it well suited for compact, resource-limited aerial platforms [36]. Aerodynamic studies have clarified how coaxial rotor performance depends on rotor separation and induced interactions under Martian atmospheric conditions, guiding the design of next-generation extraterrestrial drones. Long-term surveys of Mars rotorcraft configurations have synthesized research innovations across two decades, offering a clear roadmap for future planetary aerial exploration [120]. Collectively, these developments illustrate how flapping-wing intelligence, thrust-assisted mobility, and safe real-time planning are advancing aerial autonomy.

Research in robotic manipulation highlights another dimension of mobility, emphasizing how robots interact physically with objects and surfaces in controlled yet flexible ways. The development of advanced robotic manipulation capabilities has benefited significantly from innovations in tactile sensing, compliant actuation, and contact-aware planning. Biologically inspired flapping-wing robots using gear-driven and linkage-based mechanisms have shown how robotic systems can replicate multi-degree-of-freedom wing kinematics, providing insights that extend beyond aerial locomotion into compliant mechanical design [121]. One-finger manipulation research has demonstrated that carefully planned pushing actions can achieve complex object repositioning tasks in three dimensions, highlighting the capabilities of minimal-contact manipulation strategies [6]. Soft robotic systems equipped with optical fiber-based tactile sensor sleeves have achieved high-resolution distributed sensing, enabling manipulators to detect subtle contact forces and surface deformations during delicate interactions [122]. Probabilistic contact estimation methods for quadrupeds have enabled reliable detection of ground contact events and impacts without dedicated sensors, improving robustness during dynamic motion [123]. In snake robots, wheel-mounted three-axis force sensors have enhanced environmental awareness by providing direct feedback on surface interactions [124]. Contact-aware non-prehensile manipulation techniques have shown that cluttered or confined spaces can be navigated by leveraging controlled interactions with the environment, reducing reliance on grasping alone [4]. Methods for prehensile pushing that exploit alter-

CHAPTER 2. LITERATURE REVIEW

nating sticking and slipping phases have enabled stable regrasping and in-hand object repositioning, extending manipulation capabilities with simple grippers [125]. Together, these efforts show that tactile intelligence and contact-based reasoning play a central role in developing dexterous robotic manipulation.

Robust locomotion and manipulation also rely on accurate computational models, and advances in simulation and numerical optimization have become essential tools for modern robotics research. The advancement of computational methods has reshaped how robotic systems are modeled, optimized, and simulated across many physical domains. Neural-network-based surrogate models combined with cubature techniques have enabled efficient approximation of high-dimensional morphing-wing dynamics, which makes real-time control and optimization feasible for systems with complex aeroelastic behavior [65]. In locomotion on structured terrain, neural scene representation methods have allowed model predictive controllers to incorporate richer environmental features directly into decision-making processes, improving performance in settings with predictable structure [126]. Evolutionary computation studies using genetic programming have shown that coordinated sidewinding behaviors can emerge from simple segmented robots when subject to selection pressures, providing insight into both biological evolution and automated gait discovery [30]. Gauss-principle-based dynamic formulations have provided efficient methods for computing whole-body dynamics of free-floating humanoids, supporting advanced simulation and control for space robotics and microgravity environments [127]. NeuFlow has demonstrated that high-fidelity optical flow can be computed in real time on resource-limited embedded platforms, which enables robust perception pipelines for small aerial and mobile robots [128]. Sensor-based control in modular-loop robots has produced impressive rolling speeds of up to 26 module lengths per second, demonstrating how mechanical design and feedback control can jointly enable extreme dynamic performance [129]. The Chrono multi-physics engine supports unified simulation of rigid bodies, granular media, deformable terrain, and fluid-structure interactions, making it a critical tool for researchers who require accurate multi-domain simulation [130]. Real-time deformable-ground simulation methods have extended these capabilities by allowing vehicles and legged robots to train, test, and evaluate performance on soft terrain without prohibitive computational cost [44]. Together, these contributions demonstrate how computational innovation is driving advances in simulation fidelity, design optimization, and real-time control.

Recent work has started to unify these developments, pushing toward robotic systems that combine multiple forms of mobility, share information across teams, and make decisions based on rich perception. The robotics field continues to evolve through the integration of new mobility

CHAPTER 2. LITERATURE REVIEW

strategies, exploration paradigms, and perception-driven decision making. Geological analyses of Martian lava tube systems have revealed structurally stable subterranean networks with significant scientific and habitation potential, which motivates robotic systems capable of subterranean access [131]. Hybrid locomotion planning has shown that combining legged, rolling, and flying capabilities within a single platform enables safe and versatile navigation across difficult terrains when coordinated using probabilistic roadmaps and reference governors that enforce constraints [132]. Distributed flight arrays composed of autonomous rotor units have demonstrated the feasibility of modular aerial platforms that can dock, separate, and fly cooperatively, suggesting innovative directions for swarm-based planetary exploration [133]. Surveys of perception-driven obstacle-aided locomotion for snake robots have emphasized the importance of environmental interaction, showing how deliberate contact with features such as walls and rocks can improve stability and traction [134]. Multi-robot coordination strategies have employed error-constrained formation-following rules to maintain synchronized motion among multiple snake robots, enabling cooperative exploration and manipulation [135]. Traversability-aware planning frameworks have demonstrated that fusing robot internal states with environmental difficulty metrics provides safer trajectory selection in mountainous or uneven terrain [10]. The SenSnake platform, with its 3D bending capabilities and distributed force sensors, has also created new opportunities for controlled experimental studies of contact-rich locomotion strategies, offering a benchmark system for future research [136]. Together, these developments highlight a fast-moving trend toward multimodal, perception-driven, and cooperative robotic systems that are capable of operating in the most demanding environments.

Chapter 3

Methodology

This chapter presents the complete methodological framework used to study sidewinding and tumbling locomotion of the COBRA robot across rigid, compliant, and granular terrains. The material is organized to provide a coherent progression from analytical modeling to simulation tools that capture different modes of contact and terrain behavior.

Sidewinding Gait. Section 3.1 introduces the contact-implicit modeling formulation that establishes the compliant contact dynamics and the continuous-time equations of motion used throughout this thesis. This formulation serves as the analytical foundation for the subsequent simulation environments.

Section 3.3 describes the MATLAB Simulink implementation developed for sidewinding locomotion on rigid ground. In this setting, the robot’s collision geometry, frictional interactions, and distributed body contacts are handled through Level-2 S-functions that compute geometric relations and contact quantities in real time.

Section 3.6 then extends the analysis to compliant soil interaction by introducing the Project Chrono Soil Contact Model (SCM) pipeline. This simulation environment captures continuum-style deformation and enables the study of sidewinding on yielding terrain without relying on particle-resolved granular physics.

Tumbling Gait. To broaden the study from serpentine locomotion to multi-modal rolling, this chapter also includes a tumbling simulation developed in MATLAB Simulink. Here, the terrain is rigid and high-energy impacts are resolved through a compliant spring–damper contact law with velocity-dependent friction. This model provides a controlled reference case for evaluating the effects of terrain compliance.

Finally, Section 3.14 introduces the Chrono DEM Engine framework used for particle-

resolved granular terrain simulation. This includes the procedures for generating the granular bed, configuring slope geometry, and coupling the robot’s kinematics with the dynamics of individual particles. Together, these tools allow detailed investigation of how rolling locomotion interacts with fully deformable terrain.

Taken together, these components form a unified multi-resolution analysis pipeline that spans analytical modeling, rigid-ground simulation, compliant terrain modeling, and granular physics. This layered structure enables a systematic comparison across terrain types while maintaining a consistent treatment of the robot’s motion and contact interactions.

3.1 Modeling



Figure 3.1: Closeup view of robot sand surface interactions. *Image courtesy of Adarsh Salagame*

The modeling framework presented in this section follows the full contact-implicit formulation developed in the IEEE RA-L 2026 study. The goal is to capture how distributed body segments of the COBRA robot interact with deformable ground through compliant normal and tangential forces, while maintaining an explicit and differentiable structure suitable for simulation and

CHAPTER 3. METHODOLOGY

comparison with real terrain behavior. The formulation retains all geometric, kinematic, and force components required for evaluating sidewinding locomotion on rigid and soft substrates. For completeness, the full continuous-time equations and the semi-implicit integration scheme are included.

Configuration and dynamics without contact. We begin by describing the rigid-body dynamics of the snake robot in the absence of terrain interaction. Let $q \in \mathbb{R}^n$ denote the generalized coordinates, $v = \dot{q}$ the generalized velocities, and $\tau \in \mathbb{R}^{m_\tau}$ the actuator torques applied at the robot's joints. The unconstrained equations of motion are

$$M(q) \dot{v} + C(q, v) v + G(q) = B(q) \tau + \sum_{i=1}^{m_c} J_i(q)^\top f_i, \quad (3.1)$$

$$\dot{q} = v. \quad (3.2)$$

The matrices M , C , and G represent the standard inertial, Coriolis, and gravitational contributions. The matrix $B(q)$ maps commanded joint torques to generalized coordinates. Each potential ground contact point is indexed by $i \in \{1, \dots, m_c\}$, with J_i denoting the corresponding geometric Jacobian and f_i the spatial force imparted by the terrain. These forces are not known a priori; rather, they are determined through the compliant contact laws introduced below.

Signed distance, frames, and relative velocity. To compute ground interaction forces, the model relies on a smooth signed distance function $g_i(q)$ that measures separation or penetration between each contact point and the terrain surface. A positive signed distance indicates separation, zero indicates contact, and a negative value implies virtual penetration used for penalty-based compliance. At each contact location, an orthonormal triad is defined using the outward terrain normal \hat{n}_i and two orthogonal tangent vectors $\hat{t}_{i,1}$ and $\hat{t}_{i,2}$. These vectors form the rotation matrix

$$R_i(q) = \begin{bmatrix} \hat{n}_i & \hat{t}_{i,1} & \hat{t}_{i,2} \end{bmatrix}, \quad R_i^\top R_i = I.$$

Projecting the Cartesian relative velocity $u_i = J_i(q) v$ into this basis gives

$$\tilde{u}_i := R_i^\top u_i = \begin{bmatrix} u_{N,i} \\ u_{T,i} \end{bmatrix},$$

where $u_{N,i}$ is the normal approach speed and $u_{T,i}$ is the two-dimensional tangential velocity. The contact force is similarly decomposed as $\tilde{f}_i = R_i^\top f_i$.

This separation of normal and tangential components allows independent modeling of compression, shear, and friction.

Compliant normal force (penalty + damping). The normal interaction between the robot and the terrain is modeled using a linear spring and damper acting only during compression. Let the penetration depth be

$$\delta_{N,i} := \max\{0, -g_i(q)\},$$

with penetration rate

$$\dot{\delta}_{N,i} := -\dot{g}_i(q) = -\frac{\partial g_i}{\partial q}(q) v = -W_i(q)^\top v.$$

The normal force is then defined as

$$f_{N,i} = \begin{cases} k_{n,i} \delta_{N,i} + d_{n,i} \dot{\delta}_{N,i}, & \delta_{N,i} > 0, \\ 0, & \delta_{N,i} = 0 \text{ and } \dot{\delta}_{N,i} \geq 0, \end{cases} \quad (3.3)$$

where $k_{n,i}$ and $d_{n,i}$ are stiffness and damping parameters. This penalty-based force ensures that contact is one-sided (compression only) and that the reaction grows with penetration depth and impact velocity.

Compliant tangential force with Coulomb cap. To capture shear deformation at the contact interface, a tangential spring state $\sigma_i \in \mathbb{R}^2$ is introduced. This state accumulates tangential displacement when the contact is in a sticking regime, governed by

$$\dot{\sigma}_i = u_{T,i}. \quad (3.4)$$

A linear spring and damper provide a proposed tangential force

$$\tilde{f}_{T,i}^{\text{prop}} = -k_{t,i} \sigma_i - d_{t,i} u_{T,i}, \quad (3.5)$$

but this force must remain consistent with Coulomb friction. The final applied tangential force is

$$f_{T,i} = \begin{cases} \tilde{f}_{T,i}^{\text{prop}}, & \|\tilde{f}_{T,i}^{\text{prop}}\| \leq \mu_i f_{N,i}, \\ -\mu_i f_{N,i} \frac{u_{T,i}}{\max\{\|u_{T,i}\|, \epsilon_v\}}, & \|\tilde{f}_{T,i}^{\text{prop}}\| > \mu_i f_{N,i}, \end{cases} \quad (3.6)$$

which smoothly transitions between stick and slip. During slip, the shear state is frozen or decayed to avoid artificial energy buildup. This formulation captures shear hysteresis that is characteristic of locomotion on sand and other yielding substrates.

Contact force mapping to generalized coordinates. Reassembling the forces into the world frame gives

$$f_i = R_i \tilde{f}_i \quad (3.7)$$

$$= \hat{n}_i f_{N,i} + \hat{t}_{i,1} [f_{T,i}]_1 + \hat{t}_{i,2} [f_{T,i}]_2, \quad (3.8)$$

and the total contribution to the generalized coordinates is $J_i(q)^\top f_i$. Substitution into (3.1) and (3.2) yields the complete compliant-contact dynamics.

Compact closed-form equations of motion (continuous time). For convenience, define the activation indicator $\chi_i(q)$ to identify active contacts. The full closed-form system is

$$M \dot{v} + H = B(q) \tau + \sum_{i=1}^{m_c} J_i^\top R_i \begin{bmatrix} f_{N,i}(q, v) \\ f_{T,i}(q, v, \sigma_i) \end{bmatrix}, \quad (3.9)$$

$$\dot{q} = v, \quad (3.10)$$

$$\dot{\sigma}_i = \begin{cases} u_{T,i}(q, v), & \chi_i = 1 \text{ and } \|\tilde{f}_{T,i}^{\text{prop}}\| \leq \mu_i f_{N,i}, \\ -\alpha_i \sigma_i, & \chi_i = 1 \text{ and } \|\tilde{f}_{T,i}^{\text{prop}}\| > \mu_i f_{N,i}, \\ -\alpha_i \sigma_i, & \chi_i = 0, \end{cases} \quad (3.11)$$

with $H = C v + G$. These equations describe a coupled set of rigid-body dynamics and compliance-induced deformation modes across many distributed contacts.

Energetics and passivity note. The combination of normal and tangential damping, along with the Coulomb projection, ensures that the ground interaction does not introduce artificial energy into the system. The total power transferred through all contacts satisfies

$$\sum_i \tilde{f}_i^\top \tilde{u}_i = \sum_i (f_{N,i} u_{N,i} + f_{T,i}^\top u_{T,i}) \leq 0,$$

aside from the work done by actuators and storage in the elastic components. This passivity property plays an important role in maintaining numerical stability during simulation.

Semi-implicit (symplectic) Euler step (optional). To simulate the dynamics efficiently, a semi-implicit time-stepping scheme may be used. Given $(q_k, v_k, \{\sigma_{i,k}\})$ and step size h :

$$\begin{aligned}
q_{k+1} &= q_k + h v_{k+1}, \\
\delta_{N,i,k+1} &= \max\{0, -g_i(q_{k+1})\}, \\
u_{i,k+1} &= J_i(q_{k+1}) v_{k+1}, \\
f_{N,i,k+1} &= [k_{n,i} \delta_{N,i,k+1} + d_{n,i} (-W_i(q_{k+1})^\top v_{k+1})]_+, \\
\tilde{f}_{T,i,k+1}^{\text{prop}} &= -k_{t,i} \sigma_{i,k} - d_{t,i} u_{T,i,k+1}, \\
f_{T,i,k+1} &= \text{Proj}_{\|\cdot\| \leq \mu_i f_{N,i,k+1}}(\tilde{f}_{T,i,k+1}^{\text{prop}}), \\
v_{k+1} &= v_k + h M(q_{k+1})^{-1} \left(B(q_{k+1}) \tau_k - C(q_{k+1}, v_{k+1}) v_{k+1} - G(q_{k+1}) \right. \\
&\quad \left. + \sum_i J_i(q_{k+1})^\top R_i(q_{k+1}) \begin{bmatrix} f_{N,i,k+1} \\ f_{T,i,k+1} \end{bmatrix} \right), \\
\sigma_{i,k+1} &= \begin{cases} \sigma_{i,k} + h u_{T,i,k+1}, & \|\tilde{f}_{T,i,k+1}^{\text{prop}}\| \leq \mu_i f_{N,i,k+1}, \\ (1 - h\alpha_i) \sigma_{i,k}, & \text{otherwise } \delta_{N,i,k+1} = 0. \end{cases}
\end{aligned}$$

The scheme solves a small nonlinear system at each step and is well suited for stiff ground-contact conditions. It is the basis for all compliant-contact simulations presented in later chapters.

3.2 Sidewinding Gait Analysis

Sidewinding is the primary mode of locomotion examined in this thesis and serves as the basis for understanding efficient propulsion over flat and moderately compliant terrain. The gait emerges from coordinated pitching and yawing waves that travel along the length of the robot, creating controlled regions of contact while keeping non-supporting links elevated to reduce drag. Through these alternating patterns of contact and lift, the robot generates directional reaction forces that support stable and efficient motion.

To study this behavior in a consistent manner, three complementary platforms are used throughout the analysis. Rigid-ground modeling is carried out in Simscape Multibody, which offers a control-oriented environment for evaluating distributed contacts and wave coordination. Compliant terrain behavior is then investigated using Chrono SCM, allowing soil deformation to be incorporated in a continuum-style manner and enabling the evaluation of sinkage and load redistribution effects. Finally, hardware experiments on laboratory flooring and loose sand provide physical validation, with trajectory estimation obtained from the Intel RealSense D435i through visual inertial odometry.

These combined studies enable a direct comparison of sidewinding performance across rigid, compliant, and granular terrain conditions. The results highlight how the gait responds to reduced support stiffness, increased slip, and terrain yielding, while also demonstrating that rigid-ground models remain sufficiently predictive for short-horizon planning tasks that rely on estimating the net direction and magnitude of motion.

3.3 MATLAB Simulink Simulation for Rigid Ground

To evaluate sidewinding locomotion under idealized terrain conditions, a rigid ground model is first implemented using MATLAB Simscape Multibody. This environment provides a computationally efficient setting for validating the baseline dynamics of the COBRA platform without the additional complexity associated with soil deformation. The insights obtained here establish a useful reference when the compliant and granular terrain models are introduced in Sections 3.6 and 3.14.

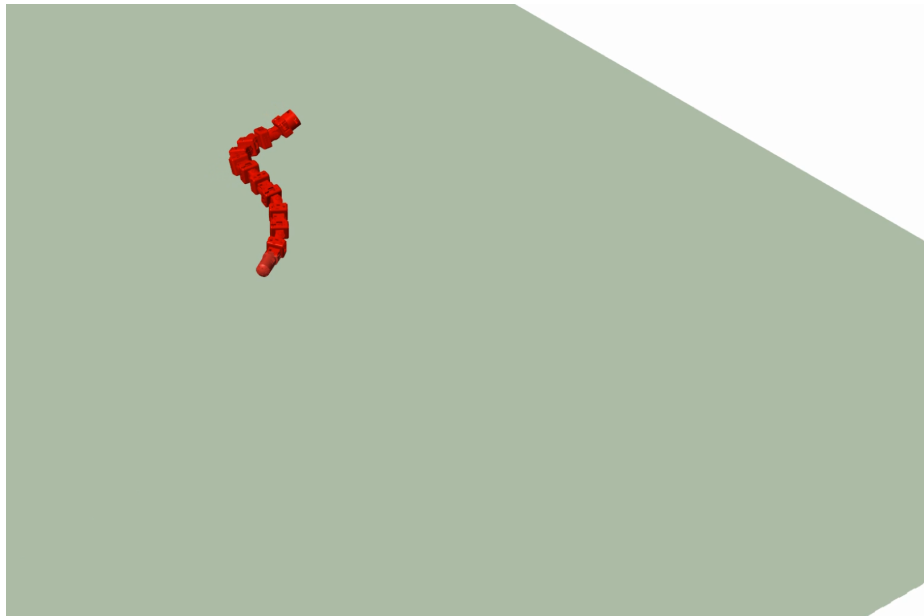


Figure 3.2: Hard-ground contact simulation results in MATLAB: normal and tangential force behavior during rigid surface interaction.

Rigid ground simulations are particularly valuable when designing control frameworks that require real-time feasibility, such as receding horizon optimization. In these settings, the model must remain lightweight yet capable of capturing the essential translational behavior produced by

CHAPTER 3. METHODOLOGY

distributed frictional contacts along the body. As a result, the rigid-ground environment serves as an efficient platform for prototyping gait strategies and verifying expected motion direction and displacement during sidewinding.

Ground Contact Model in Simscape Multibody

Contact interactions are modeled through a nonlinear spring–damper formulation for both normal and tangential directions. The normal reaction force is expressed as

$$f_n = s(d, w) (k d + b \dot{d}), \quad (3.12)$$

where d denotes the penetration depth of the link into the ground plane and \dot{d} is its rate of change. The stiffness parameter k determines the magnitude of the elastic restoring force, while the damping coefficient b regulates the rate-dependent component that absorbs energy during impact. The smoothing function $s(d, w)$ introduces a gradual transition into contact over a width w , ensuring that forces increase continuously rather than appearing abruptly at $d = 0$. This avoids numerical instabilities while still imposing strong resistance against penetration.

Tangential contact behavior is governed by a friction model defined through

$$\|f_t\| = \mu_{\text{eff}}(u_t) \|f_n\|, \quad (3.13)$$

where u_t is the tangential slip velocity at the contact point. The quantity $\mu_{\text{eff}}(u_t)$ represents the effective friction coefficient, which varies smoothly between the static value μ_s at very low slip speeds and the dynamic value μ_d at larger slip speeds. This dependency reflects the physical tendency of surfaces to resist motion strongly when nearly stationary, followed by reduced resistance once slipping occurs. Introducing a critical slip velocity creates a smooth transition between these regimes and prevents abrupt switching between sticking and sliding.

Simulation Configuration

To produce a clean baseline for rigid terrain, the contact model parameters are selected to approximate a stiff, non-compliant surface. The normal stiffness is set to $k = 10^4$ and the damping to $b = 10^3$, providing strong resistance to penetration with moderate dissipation of impact energy. The smoothing width is chosen as $w = 10^{-3}$ m to maintain continuous contact transitions. The

CHAPTER 3. METHODOLOGY

friction coefficients are assigned values of $\mu_s = 0.5$ and $\mu_d = 0.3$, while the critical slip speed is set to 10^{-3} m/s so that the transition between static and dynamic friction occurs smoothly.

These values produce a terrain model that behaves effectively rigid during sidewinding and prevents unrealistic sinkage or deformation, which is essential when isolating the locomotion mechanics associated purely with frictional contact.

Simulation Outputs and Usage

The Simscape implementation provides time-synchronized measurements that include joint states, actuator torques, and estimated ground reaction forces at each link, along with the motion of the robot’s center of mass. These outputs enable assessment of gait efficiency under idealized ground conditions and form the basis for comparisons with the compliant and granular terrain simulations discussed later. They also support early controller validation by allowing sidewinding wave parameters to be tested in a setting where the terrain introduces no additional complexity.

Although this model captures the principal frictional interactions that drive sidewinding, it does not reproduce effects such as sinkage, shear failure, or redistribution of support forces caused by soil yielding. These behaviors are instead addressed in higher-fidelity simulations in subsequent sections. As a result, the rigid-ground Simscape environment functions as an essential reference against which the influence of terrain deformability on COBRA locomotion can be quantified.

3.4 Project Chrono

Project Chrono is an open-source multi-physics simulation framework designed for high-fidelity modeling of articulated mechanisms, contact interactions, deformable media, and large-scale multi-body dynamics [130]. Its modular architecture allows different physical domains to be incorporated within a single environment, ranging from rigid-body dynamics and soft material models to granular flow, fluid interaction, and external cosimulation.

A key feature of Chrono is its comprehensive terrain modeling library, which supports several distinct representations of ground behavior. These models span a spectrum of complexity, beginning with simple idealized planes and extending to fully deformable particle-based media. Flat terrain provides an infinite, perfectly rigid surface with uniform elevation and is appropriate for idealized locomotion validation. Rigid terrain introduces arbitrary geometric variations through height maps, enabling controlled testing over structured surfaces. CRG terrain extends this idea

CHAPTER 3. METHODOLOGY

further by supporting curvilinear road profiles that are commonly used in automotive and structured environment simulations.

For deformable ground modeling, Chrono offers multiple options. The Soil Contact Model (SCM) approximates continuum-style soft soil by allowing vertical sinkage and permanent deformation under load, creating a realistic intermediate representation of compliant terrain. Granular terrain is captured through the Discrete Element Method, where individual particles interact through collision-based forces and produce complex behaviors such as shear bands, slip layers, and localized compaction. At the highest fidelity, Chrono includes finite element terrain models based on the Absolute Nodal Coordinate Formulation, which allow deformable solids to be represented with detailed elastic and plastic responses.

This breadth of terrain models enables the selection of an appropriate level of fidelity for each experiment in this thesis. Rigid-ground validation is carried out in MATLAB Simulink, soft-terrain behavior is studied through the SCM framework, and high-resolution granular effects are analyzed using DEM. Chrono therefore forms the foundation of the multi-resolution simulation pipeline developed in later sections and allows terrain complexity to be increased in a controlled and systematic manner.

3.5 Setting up Project Chrono

A custom Chrono build environment was prepared for this thesis and published internally for the Silicon Synapse Lab. The repository provides a validated configuration of Chrono v9.0.1 with all required dependencies, module settings, and source adjustments needed for GPU acceleration, Multicore physics, and both SCM and DEM terrain models [130]. The complete setup is available at:

`https://github.com/SS-Lab-at-NU/chrono-custom`

To support deformable terrain simulation for snake-robot locomotion, Chrono was built with the Vehicle module for soil interaction, the Multicore and GPU modules for parallelized and CUDA-accelerated computation, and the VSG visualization stack for high-performance rendering. Parsers were enabled for mesh import, and the Irrlicht demos were included to assist with quick validation runs. Several small source-level updates were required to ensure compatibility with recent hardware. Chrono’s default CUDA version checks were extended so that the RTX 4050 and

CHAPTER 3. METHODOLOGY

CUDA 12.4 toolchain would be recognized, and Thrust version validation was broadened to accommodate newer releases used in Multicore builds. These updates prevent the build system from incorrectly disabling GPU features.

The VSG visualization stack was compiled manually because upstream scripts contained version conflicts. All VSG packages were installed under a dedicated local prefix, and a stable release of `vsgImGui` was checked out to guarantee reliable GUI operation on Ubuntu 22.04 with CUDA 12.4. A validated CMake configuration was then generated, enabling both GPU and Multi-core physics, specifying architecture 89 for Ada-Lovelace GPUs, and explicitly referencing Blaze and Thrust to avoid auto-detection errors. This profile served as the basis for all SCM and DEM simulations presented later in Sections 3.6 and 3.14. All required patches, instructions, and dependency scripts are included in the `chrono-custom` repository, ensuring that future researchers can rebuild the environment without configuration issues and maintain a consistent simulation platform across the lab.

3.6 Deformable SCM (Soil Contact Model)

The SCM implementation in Project Chrono provides a deformable soil model that captures terramechanical effects important for locomotion on loose terrain. In contrast to rigid or penalty-based compliant surfaces, SCM explicitly models sinkage, plastic yield, shear deformation, and bulldozing flow, while remaining computationally efficient for multi-body simulation [130]. This enables realistic soil-robot interaction during sidewinding, where ground compliance strongly influences propulsion, stability, and body shaping throughout the gait.

The terrain is represented as a Cartesian grid defined over the horizontal coordinates of a local frame. Each grid node stores its undeformed elevation $z_0(x, y)$, the current vertical deformation $z(x, y)$, contributions from elastic and plastic sinkage, the accumulated shear state, and the associated normal pressure and shear stress. To avoid allocating the full grid, Chrono creates nodes only when the robot interacts with the surface, maintaining a sparse hash-mapped structure that scales with the area of deformation rather than the total terrain size. This allows large domains to be simulated without excessive memory cost.

At every time step, vertical rays are cast from active terrain nodes toward the robot. When a ray intersects the geometry, penetration depth is computed and contact forces are applied. Ray casting is multi-threaded for speed and is restricted to the oriented bounding box of the robot so that empty regions are not tested unnecessarily.

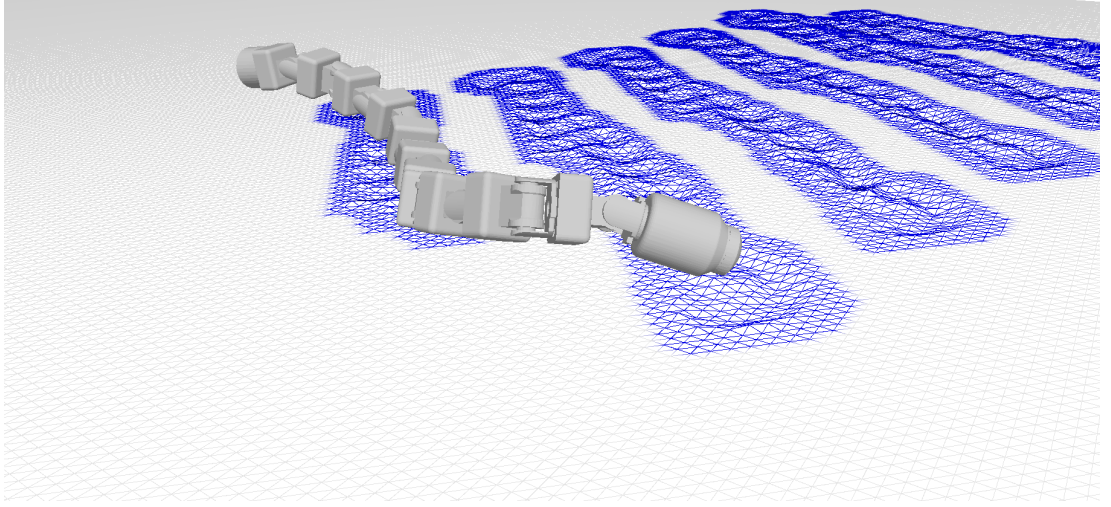


Figure 3.3: SCM simulation showing vertical deformation of terrain nodes under the COBRA robot during sidewinding. The mesh illustrates permanent soil depressions, shear displacement, and berm accumulation across multiple gait cycles.

Vertical soil response is governed by the Bekker–Wong relationship:

$$\sigma = (k_c b + k_\phi) y^n, \quad (3.14)$$

where σ is the normal pressure, y the sinkage, k_c and k_ϕ the cohesive and frictional stiffness parameters, n a compaction-dependent exponent, and b a characteristic contact width. For non-rectangular contact patches, b is approximated using the area A and perimeter L of the contact region:

$$b \approx \frac{2A}{L}.$$

Shear deformation contributes to traction through a Janosi–Hanamoto law:

$$\tau = (c + \sigma \tan \varphi) \left(1 - e^{-\frac{j}{K}}\right),$$

where c is cohesion, φ the soil friction angle, j the accumulated shear displacement, and K the characteristic shear deformation length. The model captures the transition from elastic shear to plastic flow as the traction limit is approached and exceeded.

SCM tracks permanent deformation produced when the robot overruns a region of soil. Material is pushed laterally, forming berms and ruts that influence future contacts. Parameters such as erosion angle, lateral flow factor, and the number of refinement steps per update can be adjusted to match different soil types.

CHAPTER 3. METHODOLOGY

Viscous damping contributes to the stability of terrain response through

$$f_d = -R \cdot \dot{y},$$

where R is the vertical damping per unit area. This term is particularly important for fast motions or aggressive gaits, where numerical stability may otherwise degrade.

The deformable terrain is implemented through the class `chrono::vehicle::SCMTerrain`. It supports initialization from flat surfaces, heightmaps, or input triangle meshes. Soil parameters can be assigned globally or spatially, and detailed contact information can be queried for either individual bodies or specific nodes. The API also provides access to all modified grid nodes for visualization and to overlays that display sinkage, pressure, yield state, and bulldozing effects. A co-simulation mode is also available when terrain forces need to be exported without being applied internally.

SCM achieves near real-time performance by storing only active nodes, limiting collision checks to the robot’s immediate vicinity, parallelizing ray casting, and updating visualization incrementally. When Chrono is built with CUDA, additional GPU acceleration is available for certain components.

SCM provides a mid-fidelity terrain model situated between rigid or penalty ground, which cannot capture soil deformation, and particle-based DEM, which offers high predictive accuracy at significantly greater computational cost. This middle ground enables systematic exploration of gait behavior under varying soil strengths and supports direct comparison with experimental data on loose sand.

3.7 SCM Terrain Mathematical Formulation

Chrono’s SCM implementation is built on semi-empirical soil mechanics models originally developed by the German Aerospace Center (DLR) [42], [43] and later generalized to support arbitrary rigid geometries in real-time simulation environments [44]. The underlying principle is to relate the deformation of the soil at each terrain node to the normal and tangential reaction forces that oppose penalties to the surface and resist shear motion. In this manner, SCM captures the core terramechanical behavior that governs locomotion over loose or deformable terrain.

Normal pressure–sinkage relationship. SCM treats the soil as a vertically deformable elastic–plastic medium. At each terrain node lying beneath the contact footprint, the normal stress

CHAPTER 3. METHODOLOGY

is computed using the Bekker–Wong pressure–sinkage equation:

$$p = \left(\frac{K_c}{b} + K_\phi \right) z^n, \quad (3.15)$$

which relates the sinkage depth z to the normal pressure p generated by the terrain. The quantity z is the vertical displacement of the soil relative to its undeformed state and measures how far the surface has been compressed by the robot. As z increases, the material compresses more densely, resulting in higher terrain resistance.

The parameter K_c is the cohesive modulus and captures the contribution of soil cohesion to the resulting pressure. Cohesion represents intermolecular forces or cementation in the soil grains and produces resistance even when the normal load is small. The term K_ϕ is the frictional modulus and incorporates resistance due to internal friction of the soil. Soils with higher friction exhibit greater stiffness when compressed.

The exponent n controls the degree of nonlinearity in the pressure–sinkage law. A value of $n < 1$ corresponds to a material that stiffens slowly, while $n > 1$ corresponds to a material that rapidly becomes rigid with penetration. Loose dry sand typically exhibits n between 0.5 and 1.0, giving the terrain a moderately nonlinear response.

The patch size b introduces the effect of footprint geometry into the pressure–sinkage relationship. Smaller contact widths concentrate force over a narrower area and therefore increase pressure for the same sinkage depth. Since snake robots do not form rectangular footprints, b is estimated from the area A and perimeter L of the contact region:

$$b \approx \frac{L}{2A}. \quad (3.16)$$

This expression arises from Bekker’s adaptation for arbitrary geometries and produces an effective width consistent with the observed terramechanics of complex footprints.

The form of (3.15) ensures that pressure rises sharply as the sinkage grows, in agreement with field observations that sand becomes markedly stiffer once particles compact and interlock under deeper penetration.

Tangential shear resistance and yield. SCM computes tangential shear stress generated by horizontal slip using the Janosi–Hanamoto law:

$$\tau = \tau_{\max} (1 - e^{-j/k}), \quad (3.17)$$

where τ is the shear stress opposing motion along the soil surface. The variable j denotes the accumulated shear displacement and measures how far the soil at a node has been dragged relative to

CHAPTER 3. METHODOLOGY

its original position. The parameter k is a characteristic shear deformation length scale, determining how quickly soil transitions from elastic response to plastic yield.

The maximum attainable shear stress,

$$\tau_{\max} = c + p \tan(\phi), \quad (3.18)$$

follows a Mohr–Coulomb relationship. The cohesion c captures the inherent shear strength of the soil in the absence of normal pressure. The term $p \tan \phi$ adds a pressure-dependent contribution due to friction, where p is the normal pressure and ϕ is the internal friction angle. This angle describes the resistance of soil grains to sliding past each other and grows with particle roughness and angularity.

At small values of j , the exponential term in (3.17) is close to zero, and τ increases almost linearly with shear displacement. In this regime, the soil behaves elastically: deformation is reversible, and grains undergo small displacements relative to neighbors. As j becomes large, the exponential term approaches one, and τ saturates at τ_{\max} , indicating plastic failure. Once the soil yields, particles rearrange irreversibly, developing ruts and displaced material. This transition is fundamental to sidewinding traction, as it governs how effectively the robot uses lateral force generation to propel itself.

Grid-based vertical deformation model. SCM restricts deformation to the vertical axis, assuming that lateral displacement of soil appears primarily through mound and berm formation rather than through large-scale horizontal compression. Under this assumption, each terrain node stores the net vertical deflection, separated into elastic and plastic components. Plastic deformation persists after the load is removed, preserving ruts generated by the robot and enabling cumulative deformation across multiple gait cycles. Elastic recovery appears only in the decompression phase when the robot unloads the soil.

This vertical-only deformation model efficiently captures the principal effects of sinkage and berm growth, which play dominant roles in locomotion over dry granular media.

Contact identification through ray casting. Terrain nodes cast vertical rays toward the robot’s geometry to detect contact. If a ray intersects the robot, the penetration depth is calculated, and the node’s deformation state is updated accordingly. The accumulated sinkage and shear history are then used to compute normal and tangential forces, which are mapped back to the robot through standard rigid-body force accumulation. Ray-casting is limited to nodes inside the oriented bounding box of the robot to avoid unnecessary geometric queries, and the procedure is parallelized to maintain efficiency.

CHAPTER 3. METHODOLOGY

Parameter selection for loose sand sidewinding. The SCM parameters used in this thesis are calibrated from experiments on dry natural sand:

$$\begin{aligned} n &= 0.6, & K_c &= 25 \text{ N/m}^{(1+n)}, & K_\phi &= 5 \times 10^4 \text{ N/m}^{(2+n)}, \\ k &= 0.04 \text{ m}, & c &= 100 \text{ Pa}, & \phi &= 28^\circ. \end{aligned}$$

The exponent $n = 0.6$ reflects the moderate nonlinear hardening typical of granular soil. The cohesive modulus K_c is small relative to the frictional modulus K_ϕ , consistent with cohesionless media such as dry sand. The shear deformation length $k = 0.04 \text{ m}$ sets the scale over which shear stress builds up before yielding. The cohesion $c = 100 \text{ Pa}$ and internal friction angle $\phi = 28^\circ$ align with conventional terramechanics data for loose sand [137] and are validated for snake-robot simulation in recent Chrono studies [44]. These parameters produce realistic sinkage depths, slip patterns, and pressure fields consistent with experimental sidewinding trials.

Locomotion parameterization for SCM simulations. The robot's motion is driven by prescribed pitching and yawing waves along the backbone. The joint trajectories for vertical and horizontal articulation are:

$$q_{\text{ver}}(t) = A_{\text{ver}} \sin\left(2\pi ft + \frac{\pi}{6}i\right), \quad i = 0, 2, 4, \dots, 10 \quad (3.19)$$

$$q_{\text{hor}}(t) = A_{\text{hor}} \sin\left(2\pi ft + \frac{\pi}{6}j\right), \quad j = 1, 3, 5, \dots, 11 \quad (3.20)$$

where A_{ver} and A_{hor} are the vertical and horizontal amplitudes, and f is the gait frequency. Two gait patterns are used:

$$\text{Gait 1: } A_{\text{ver}} = 40^\circ, A_{\text{hor}} = 20^\circ \quad \text{Gait 2: } A_{\text{ver}} = 60^\circ, A_{\text{hor}} = 30^\circ.$$

Larger amplitudes increase the lift of non-contacting segments and concentrate forces on the subset of links in contact. This modulation of load distribution creates varying sinkage depths, shear displacement patterns, and bulldozing behavior that allow SCM to reveal how terrain strength influences propulsion.

3.8 Empirical Parameters from Simulation Code

The Chrono SCM simulations in this thesis rely on a specific set of numerical, material, and soil parameters that were tuned to reproduce the locomotion behavior observed in loose sand experiments. All values reported in this section are taken directly from the simulation implementation and correspond exactly to the configuration used during terrain testing. The purpose of this

section is to document these parameters and to explain the physical role of each, particularly those that are not standard continuum mechanics quantities.

3.8.1 SCM Terrain and Soil Properties

The SCM terrain is initialized as a flat patch whose dimensions are chosen to comfortably contain several full sidewinding cycles of the COBRA robot. The terrain extent is set to $9 \text{ m} \times 8 \text{ m}$ so that the robot can execute multiple gait cycles without reaching the boundary or reusing already disturbed terrain in the primary analysis window. The reference level of the terrain is placed at $z = -0.5 \text{ m}$, which provides sufficient vertical clearance for visualization and ensures that terrain deformation remains within a well-behaved numerical range. The grid spacing is chosen as $\Delta = 0.02 \text{ m}$, which offers a balance between spatial resolution and computational cost: this resolution is fine enough to capture contact patches under individual links while still allowing simulations to run at a reasonable speed.

The soil response parameters used in the SCM formulation are summarized in Table 3.1. Each of these plays a distinct role in shaping how the terrain reacts to loading from the robot.

Parameter	Symbol	Value
Frictional modulus	K_ϕ	$0.05 \times 10^6 \text{ N/m}^{2+n}$
Cohesive modulus	K_c	25 N/m^{1+n}
Sinkage exponent	n	0.6
Cohesion	c	25 Pa
Internal friction angle	ϕ	28°
Janosi shear coefficient	k	0.04 m
Elastic foundation stiffness	K	$2.5 \times 10^6 \text{ Pa/m}$
Vertical damping coefficient	R	$5 \times 10^3 \text{ Pa} \cdot \text{s/m}$

Table 3.1: SCM deformable soil model parameters used in simulation.

The frictional modulus K_ϕ and cohesive modulus K_c appear in the Bekker–Wong pressure–sinkage law and together control how strongly pressure rises with increasing sinkage. A larger K_ϕ increases stiffness associated with internal friction between grains, while K_c represents the part of the stiffness that can be attributed to cohesive forces. The exponent $n = 0.6$ determines the

CHAPTER 3. METHODOLOGY

nonlinearity of the pressure–sinkage relationship: a value less than one corresponds to a material that stiffens gradually and is consistent with loose dry sand.

The cohesion $c = 25 \text{ Pa}$ is relatively small, which reflects the near cohesionless nature of dry granular material. The internal friction angle $\phi = 28^\circ$ sets the slope of the Mohr–Coulomb failure envelope and captures how much shear resistance increases with normal pressure. The Janosi shear coefficient $k = 0.04 \text{ m}$ defines the characteristic shear displacement over which shear stress grows from zero to its maximum value. A smaller k would cause shear stress to saturate rapidly with very little slip, whereas a larger k would require more slip before yielding occurs. The chosen value was selected so that the amount of slip before failure matches the observed motion of the sand under the robot in physical experiments.

The elastic foundation stiffness $K = 2.5 \times 10^6 \text{ Pa/m}$ acts as an additional vertical stiffness term that stabilizes the terrain when deformation is small and avoids overly soft response at negligible sinkage. This parameter does not originate directly from classical terramechanics, but is used practically in Chrono to maintain numerical robustness. The vertical damping coefficient $R = 5 \times 10^3 \text{ Pa} \cdot \text{s/m}$ governs the rate dependent component of the vertical soil reaction. It introduces viscous-like damping in the vertical direction, which suppresses oscillations in surface height when the robot steps on and off the terrain and helps the simulation remain stable when gait frequencies increase. These values were tuned so that the simulated sinkage, recovery speed, and damping of the terrain matched the qualitative appearance and time scales observed in video recordings of the physical experiments.

Beyond the pressure–sinkage and shear laws, SCM includes several parameters that control lateral redistribution of soil due to bulldozing. The erosion angle is set to 25° . This angle defines the slope at which soil is no longer able to support itself and begins to slide sideways, forming berms along the edges of ruts. A larger erosion angle would permit steeper walls in the deformed terrain, while a smaller one would cause material to spread more readily. The chosen value was selected to produce berm profiles that visually matched the side piles of sand observed in the experiments.

The flow factor is assigned a value of 1.0. This factor scales the amount of material redistributed laterally during each erosion update. A flow factor less than one would reduce the amount of soil that moves outward in each step, leading to sharper, more localized depressions, while a value greater than one would overemphasize lateral spreading and flatten the terrain too quickly. By setting the flow factor to unity, the simulation preserves a direct correspondence between the computed deformation and the empirical terramechanics model, and we avoid artificially amplifying or suppressing lateral flow.

CHAPTER 3. METHODOLOGY

The erosion iterations per time step are set to 2. Each erosion iteration applies the bulldozing update rules once over the currently affected nodes. Running more iterations per time step allows soil to evolve toward a smoother, more equilibrated shape, whereas a single iteration yields a more jagged surface. We found that two iterations strike a good compromise between visual smoothness and computational cost, while still maintaining features such as berm edges and rut depth that closely resemble the experimental terrain profiles.

The erosion propagation rings are chosen as 3. This parameter controls how far the bulldozing effect can extend beyond the immediate contact area. A ring corresponds to one layer of neighboring nodes in the terrain grid. With three rings, soil displaced under the robot can influence nodes up to three cells away in each direction. This allows berms to grow laterally beyond the exact contact footprint but prevents material from spreading unrealistically far. We selected three rings based on visual comparison with experiment, ensuring that berm widths and overall disturbed regions match the footprint of the robot and the observed spread of sand.

3.8.2 Robot Geometry and Contact Material

The COBRA robot bodies and passive rollers are modeled in Chrono using convex collision shapes that approximate the actual link geometry. The contact material parameters are chosen to emulate the behavior of 3D printed polymer components interacting with sand. The Young’s modulus of the robot material is set to $E = 3.5 \times 10^9$ Pa, which corresponds to a relatively stiff plastic. The Poisson ratio $\nu = 0.36$ reflects the near-incompressibility typical of many polymers. These two parameters determine the effective contact stiffness when combined with the soil response.

The coefficient of friction between the robot and the soil is set to $\mu = 0.45$. This value was selected such that the ratio of tangential to normal forces obtained in simulation yields slip patterns comparable to those seen on sand, without causing unrealistic sticking or excessive sliding. The coefficient of restitution $e = 0.02$ is very small, which reflects the highly inelastic nature of impacts when a heavy robot interacts with granular soil. Kinetic energy is rapidly dissipated during contact, and the robot does not bounce noticeably, as also observed in experiments.

Each link is assigned an effective contact area

$$A_{\text{eff}} = 5.5 \times 10^{-3} \text{ m}^2.$$

This area acts as a representative footprint used when estimating the contact patch width b for the Bekker–Wong formulation. The value was chosen based on the projected area of the link regions

CHAPTER 3. METHODOLOGY

that most consistently interact with the terrain during sidewinding, and it aligns the simulated sinkage depth with what is measured in the physical tests.

3.8.3 Motion Control and Gait Execution

The robot model is imported into Chrono from a URDF description using `ChParserURDF`. Joint motion is driven in position control mode using precomputed sinusoidal trajectories stored in a time-indexed CSV file. This ensures that the same gait parameters used in other simulation platforms and in experiments are precisely reproduced.

Before locomotion begins, the simulation is run for a 2 s settling period with the gait either at zero amplitude or slowly ramped. This allows the robot to come to rest on the deformable terrain, ensuring that initial conditions do not contain spurious transients or unrealistically large oscillations in sinkage. The alternating sign convention in the joint commands enforces a lateral rolling constraint that replicates the desired sidewinding pattern: neighboring joints are driven with phase offsets and sign changes so that the body forms the characteristic sideways-traveling wave with vertical and horizontal components.

3.8.4 Numerical Solver and Visualization

The Chrono simulations are integrated with a fixed time step of $\Delta t = 0.001$ s. This time step is small enough to resolve the contact dynamics between the robot and the deformable terrain while remaining large enough to keep overall simulation runtimes manageable. Contact constraints are solved using a Barzilai–Borwein non-smooth iterative method, with a maximum of 200 solver iterations per time step. The Barzilai–Borwein scheme accelerates convergence for the non-smooth complementarity problems that arise in contact and friction, and the iteration cap prevents excessive computation if convergence slows in difficult configurations.

Visualization is handled through the Vulkan Scene Graph backend. This backend provides hardware-accelerated rendering suitable for detailed terrain meshes and for visualizing node-level deformation and contact forces during locomotion. During all simulations, full spatial wrenches for each body are logged at every time step. These time series contain forces and torques at the body frame and are later used for offline analysis of load distribution, traction patterns, and energy transfer between the robot and the terrain.

Together, these empirical parameters and numerical settings have been validated by comparing Chrono SCM results against experimental sidewinding data. The configuration documented

here defines the baseline used for all deformable terrain simulations in this thesis and provides a reproducible reference for future studies.

3.9 Simulation Loop

The Chrono–SCM simulation operates through a sequential update loop that advances the multibody dynamics, computes terrain deformation, and applies contact forces at each timestep. The pseudo code below summarizes the execution structure implemented in this work:

Algorithm 1 Project Chrono SCM Simulation Loop

- 1: **Initialize Chrono system** and set gravity: $\mathbf{g} = (0, 0, -9.81) \text{ m/s}^2$
 - 2: Load robot multibody model from URDF using `ChParserURDF`
 - 3: Assign material properties and contact geometry to all link bodies
 - 4: Create SCM terrain with dimensions $(9 \times 8) \text{ m}$ and grid resolution $\Delta = 0.02 \text{ m}$
 - 5: Set soil mechanical parameters $\{K_c, K_\phi, n, c, \phi, k, K, R\}$
 - 6: Configure bulldozing model and terrain visualization options
 - 7: Load joint trajectory input (time-indexed sinusoidal gait)
 - 8: Initialize time $t \leftarrow 0$
 - 9: **while** $t < T_{\text{final}}$ **do**
 - 10: Read current pose of each link body
 - 11: Apply joint position commands at time t (position-controlled actuation)
 - 12: Perform ray-casting from terrain grid nodes to collision shapes
 - 13: Identify active contact patches and compute:
 - 14: Sinkage z
 - 15: Contact area A and perimeter L
 - 16: Normal stress p
 - 17: Shear stress τ
 - 18: Update terrain vertical deformation and bulldozing side flows
 - 19: Accumulate nodal contact forces and apply to rigid bodies
 - 20: Integrate multibody dynamics for timestep Δt
 - 21: Log contact forces, joint states, and body kinematics
 - 22: **if** visualization enabled **then**
 - 23: Update VSG render scene
 - 24: **end if**
 - 25: $t \leftarrow t + \Delta t$
 - 26: **end while**
 - 27: **Terminate** simulation and export datasets for analysis
-

This loop ensures consistent coupling between deformable terrain response and sidewind-
ing locomotion kinematics. Terrain deflection evolves only where contact occurs, while high-
frequency wrench logging enables post-processing of distributed contact mechanics along the COBRA

body.

3.10 Simulation Details

The Project Chrono SCM environment developed in this thesis integrates custom snake robot modeling, deformable soil mechanics, GPU-supported multibody simulation, and high-frequency contact logging. The overall architecture in Figure 3.4 organizes these elements into clean modules that support consistent data flow and reproducible experiments.

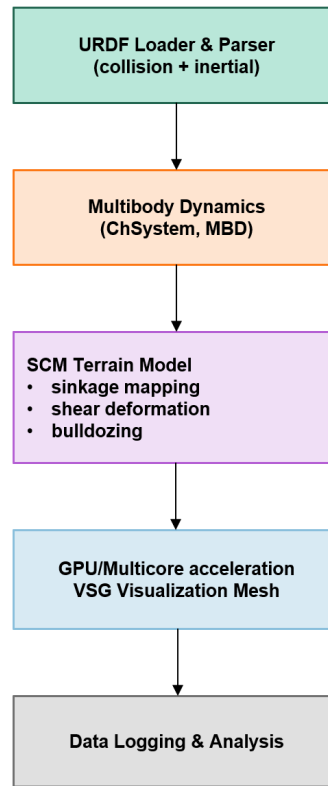


Figure 3.4: Software architecture of the Chrono-based SCM simulation environment for COBRA.

3.10.1 Core Components

Chrono’s Multibody Dynamics engine computes rigid-body motion, joint constraints, and system updates at each timestep. Robot geometry, inertial values, and joint information are imported

CHAPTER 3. METHODOLOGY

directly from the URDF file, ensuring consistency with ROS and Gazebo without maintaining separate geometry.

The SCM subsystem models deformable terrain by applying pressure–sinkage relations, shear deformation, bulldozing behavior, and damping effects. Terrain states such as sinkage and shear displacement are updated continuously and influence future contacts. GPU and multicore acceleration are used to handle the large number of terrain nodes. Visualization is provided by the Vulkan Scene Graph, which renders the robot and evolving terrain fields in real time.

3.10.2 Required Input Assets

The simulation uses the COBRA URDF model for link hierarchy, inertial tensors, actuator frames, and simplified convex collision meshes. Joint trajectories are loaded as time-indexed CSV files containing the sinusoidal commands used for sidewinding. SCM parameters specify the soil patch size, grid resolution, and soil constants such as pressure–sinkage coefficients, shear properties, bulldozing factors, and damping terms. These inputs define the mechanical environment experienced by the robot.

3.10.3 Simulation Execution Pipeline

The simulation begins with initialization of the multibody system, materials, and parsers. The robot is loaded from URDF, its joints are linked to the control subsystem, and collision shapes are added to the scene. The SCM grid is then created and assigned all soil and bulldozing parameters, which determine how displaced material spreads.

Logging channels are initialized, and the main loop advances the robot and terrain states together. SCM updates sinkage, shear deformation, and plastic displacement, while the solver computes forces and integrates the multibody motion. Outputs are written continuously to disk for later analysis.

3.10.4 Logging and Output Data

The system records link trajectories, orientations, and joint states at roughly five hundred hertz. SCM logs nodal forces, sinkage depths, shear displacement, and vertical deformation, creating a detailed record of terrain response. Additional metadata such as the number of active nodes, ray casting counts, and solver statistics is stored for diagnostics.

This modular design runs reliably on both local workstations and GPU clusters. All configuration files and build scripts used in this thesis are available through the SSLab GitHub repository, providing a stable platform for studying locomotion on deformable terrain using Chrono and SCM.

3.11 Hardware Tests

To evaluate the locomotion performance of the COBRA robot on real terrain, two controlled sets of hardware experiments were conducted. The first involved rigid laboratory flooring equipped with high-precision external motion capture, while the second involved an outdoor loose-sand environment in which state estimation relied entirely on onboard visual-inertial odometry. The objective was to compare physical behavior against the predictions of the rigid-ground Simulink model in Section 3.3 and the deformable SCM terrain simulations in Section 3.6. These experiments provide the empirical basis needed to judge how well the simulation pipeline reproduces both locomotion efficiency and terrain-robot interaction effects.

3.11.1 Laboratory Rigid-Ground Experiments

The rigid-ground experiments were conducted inside the motion-capture space of the Northeastern University Silicon Synapse Lab. The environment provides a flat, hard floor with negligible compliance, making it suitable for validating the rigid-ground assumptions used in the Simulink model. A twelve-camera OptiTrack system, sampling at one hundred and twenty hertz, tracked the robot’s head link using reflective markers. This setup supplies highly accurate six-degree-of-freedom ground-truth trajectories and enables direct comparison between measured and simulated forward progression, lateral drift, and body heading changes.

The commanded joint motions were identical to those used in simulation. They were produced from the same sinusoidal trajectory generator and executed by the robot’s onboard motor drivers. Each experimental condition was repeated multiple times to mitigate motion-capture dropouts, brief occlusions, or minor variations in actuator response. Repeated trials help ensure that deviations between simulation and experiment reflect modeling limitations rather than random measurement noise.



Figure 3.5: Snapshots of the snake robot operating in rigid laboratory conditions using motion capture and on loose outdoor sand using onboard visual–inertial odometry. Both setups are used to benchmark the predicted behavior from rigid and deformable terrain simulations. *Image courtesy of Adarsh Salagame.*

3.11.2 Loose-Sand Experiments with Onboard VIO

The loose-sand tests were performed in an outdoor environment consisting of dry, unconsolidated sand with grain sizes in the approximate range of zero point one to one millimeter. Such terrain is continuously reshaped by the robot’s motion, producing sinkage, shear trenches, berm build-up, and other topographical changes that make external markers or fiducial-based tracking unreliable. Further, a laboratory-style motion-capture system cannot be deployed outdoors under these conditions.

For this reason, trajectory estimation was achieved using onboard monocular visual–inertial

CHAPTER 3. METHODOLOGY

odometry based on ORB-SLAM3 [138]. A RealSense D435i camera supplied synchronized RGB frames and inertial measurements at thirty hertz. The system constructs a locally consistent trajectory by combining image features and accelerometer readings with a state estimator that manages drift over short time windows. This method provides reliable motion estimates when visual features remain stable in the field of view and when the robot’s motion does not produce excessive blur.

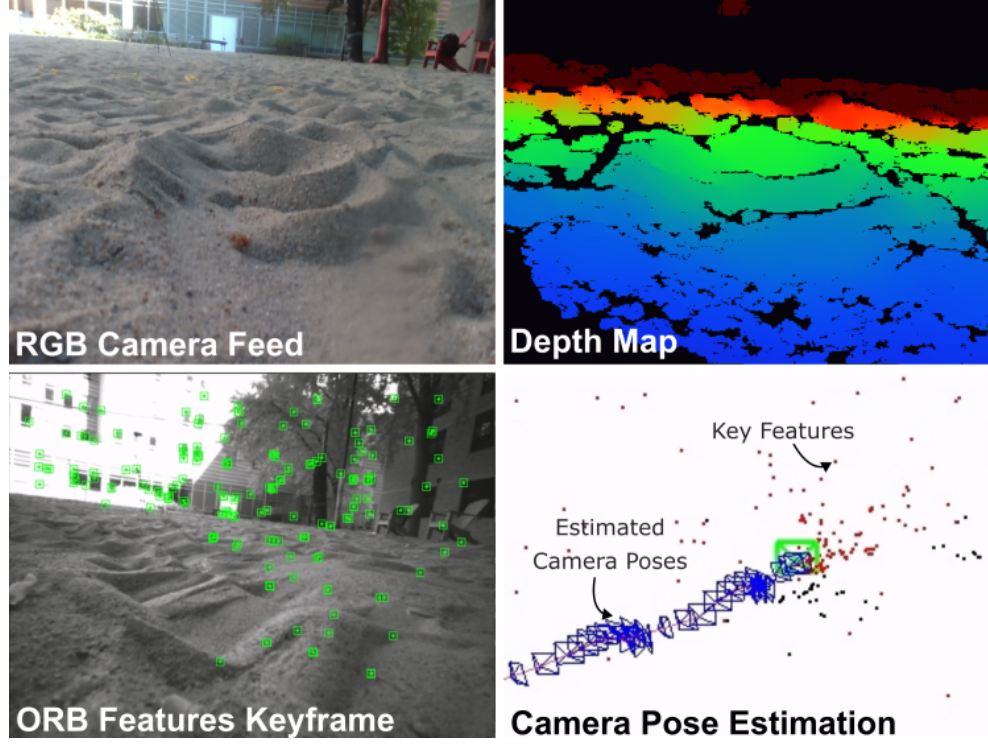


Figure 3.6: Onboard sensing during loose-sand tests. The RGB stream, depth reconstruction, and the visual–inertial odometry pose estimation illustrate how robot motion is tracked in environments where external motion capture is not feasible. *Image courtesy of Adarsh Salagame.*

Visual–inertial odometry performance was sensitive to image quality, terrain appearance, and the robot’s instantaneous motion. Large roll or pitch movements increased motion blur and could reduce the number of trackable features in the scene. In addition, self-occlusion from nearby links occasionally disrupted the feature-tracking pipeline. Trials in which the estimator drifted excessively or lost track altogether were removed from the dataset to prevent corrupted trajectories from influencing the comparison with simulated predictions.

3.11.3 Gaits and Test Conditions

Four combinations of gait and frequency were commanded across the two environments. These correspond to the two gait shape parameters used throughout this work, each executed at two distinct frequencies:

$$\text{Gait 1: } \{0.4, 0.2\} \text{ Hz} \quad \text{Gait 2: } \{0.3, 0.1\} \text{ Hz.}$$

These frequencies were chosen by balancing two competing needs. Higher frequencies promote faster forward travel and more pronounced sidewinding deformations, increasing the stress applied to the soil. Lower frequencies increase the likelihood of stable visual–inertial odometry performance because image blur is reduced and features remain more easily trackable between frames. The lowest-frequency case of Gait 2 at zero point one hertz consistently produced unstable odometry, often leading to rapid drift; such trials were excluded from the final analysis.

3.11.4 Dataset Summary

In each environment, a consistent suite of measurements was gathered to support comparison with simulation. For the rigid laboratory surface, the head-link position and orientation were recorded throughout each trial. Commanded joint trajectories and encoder-reported joint measurements were stored in parallel to diagnose discrepancies between intended and realized motion. In the loose-sand environment, the onboard visual–inertial odometry provided relative motion estimates, which were stored together with joint data and timestamps. In both environments, qualitative observations were documented, including visible sinkage, slip patterns, link–soil interaction, and notable terrain disturbances. These records also include notes about visual–inertial odometry reliability in order to distinguish between estimator degradation and genuine differences in locomotion behavior.

The combined hardware dataset serves as both a validation reference for the simulation models and an empirical foundation for understanding how gait amplitude, frequency, and terrain compliance shape the robot’s overall locomotion performance.

3.12 Tumbling Gait Analysis

Tumbling is a high-energy locomotion mode used by the COBRA robot to descend steep slopes where sidewinding becomes ineffective or unstable. In this mode, the robot mechanically links its head and tail to form a closed-loop barrel configuration. This shape converts the body into a protective rolling shell that shields sensitive components and allows the vehicle to descend

CHAPTER 3. METHODOLOGY

slopes primarily through gravitational potential energy rather than through precision-controlled shape changes. The closed-loop structure stabilizes the center of mass inside the body cavity and distributes external impacts over the outer links, making tumbling particularly well suited for rapid descent on slippery, steep, or yielding terrain.

To understand the physics of downhill tumbling, this thesis uses two modeling approaches that complement one another. The first is a rigid-ground model built in MATLAB Simulink. This representation isolates the pure rotational dynamics of the barrel-like structure, allowing analysis of angular acceleration, normal impact forces, and slip-induced motion when the robot rolls over a hard inclined plane. By neglecting soil deformation, this model emphasizes the effects of gravity, contact stiffness, and the placement of the center of mass. It provides a lightweight environment in which impacts, rebound behavior, and momentum transfer can be studied without the numerical complexity of deformable media.

The second modeling approach uses the Chrono DEM Engine to simulate tumbling on granular terrain. DEM represents the soil as an ensemble of discrete particles that interact through collision laws, friction, and cohesive or cohesionless force models. During tumbling, each body link interacts with hundreds or thousands of particles, causing localized sinkage, particle rearrangement, drag, and mass-wasting effects. Soil yields beneath the robot, redistributes under its weight, and may even avalanche downslope depending on slope angle, grain size, and local compaction. This method captures the detailed mechanics that cannot be approximated with rigid-surface or simple compliance models, including complex stick–slip transitions, intermittent burial of the rolling shell, and velocity-dependent drag forces generated by particle impacts.

The rigid-ground and granular-terrain models together provide a validation framework that spans simple to highly detailed physical representations. The rigid model reveals how tumbling initiates, how body shape influences rotational stability, and how gravity and impact govern descent speed. The DEM model extends this analysis to real soils, uncovering the influence of particle size, compaction, yield strength, and depth-dependent resistance on overall mobility. By comparing results across the two approaches, it becomes possible to separate the roles of pure rigid-body dynamics from terrain-mediated effects such as sinkage, drag, and energy dissipation through soil deformation.

This combined analysis enables high-fidelity assessment of downhill mobility for snake robots and provides the physical foundation needed to evaluate their suitability for future off-road or planetary exploration scenarios, where complex terrain and unreliable footing can restrict the effectiveness of more traditional gaits.

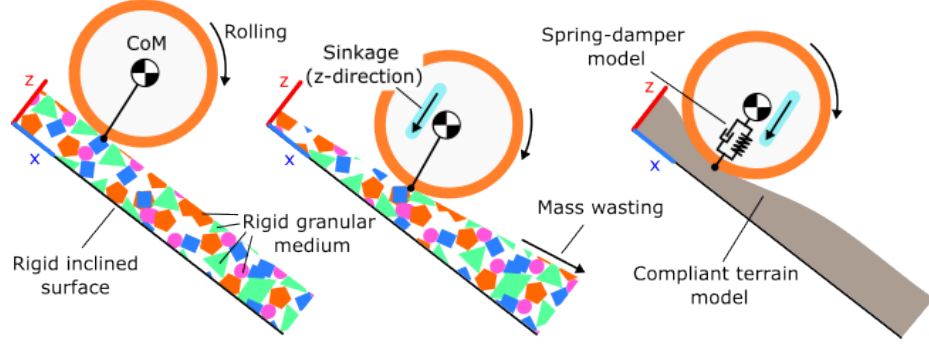


Figure 3.7: Comparison of terrain–interaction models during downhill tumbling. Left: Rigid inclined surface dominated by rotational inertia and hard impact. Center: Granular medium with depth-dependent sinkage and slip. Right: Compliant deformable material exhibiting spring–damper response and terrain reshaping due to mass wasting. *Image courtesy of Adarsh Salagame.* [16]

3.13 MATLAB Simulink Tumbling Model for Rigid Ground

To establish a fast and interpretable reference for the COBRA robot’s rolling locomotion, a rigid-ground tumbling simulation was developed in MATLAB Simscape Multibody. This model provides a simplified environment in which tumbling dynamics can be analyzed without the additional complexity of soil deformation. It allows direct examination of how the robot’s geometry, mass distribution, and contact forces govern its rotational motion during downhill travel. The model functions as a counterpart to the granular simulations presented later in Section 3.14, and together the two frameworks separate pure rigid-body effects from terrain-mediated phenomena.

In this Simulink setting, the robot is configured into its circular barrel shape, produced by mechanically linking the head and tail modules. This closed-loop configuration relocates the center of mass toward the interior and distributes impacts over the outer surface of the body. The terrain is modeled as a perfectly rigid plane, meaning no soil deformation, sinkage, or granular flow occurs during contact. Instead, forces arise solely from elastic and dissipative interactions between the shell of the robot and the rigid surface. These interactions are captured through a nonlinear spring–damper formulation in the normal direction and a velocity-dependent Coulomb friction law in the tangential direction. The same mathematical structure appears in the rigid contact model used for sidewinding in Section 3.3, ensuring consistency between the two locomotion modes.

Normal forces are governed by a spring–damper contact law of the form

$$f_n = s(d, w) (k d + b \dot{d}),$$

CHAPTER 3. METHODOLOGY

in which the penetration depth d and its time derivative \dot{d} are used to compute the instantaneous force transmitted through the ground. The constant k represents the normal stiffness of the contact, which determines how strongly the robot resists penetration. Higher stiffness values cause the contact to behave more like a hard collision, leading to more abrupt changes in angular velocity during tumbling. The coefficient b provides dissipation that converts impact energy into heat, reducing rebound and smoothing the transient response. The smoothing function $s(d, w)$, which transitions between non-contact and contact states over a characteristic width w , ensures that the normal force evolves continuously as the robot rolls, preventing numerical instabilities associated with sharp contact transitions.

Tangential forces follow a velocity-dependent Coulomb friction law,

$$\|f_t\| = \mu_{\text{eff}}(u_t) \|f_n\|,$$

where u_t is the relative slip velocity at the contact point. The effective friction coefficient $\mu_{\text{eff}}(u_t)$ interpolates smoothly between static and dynamic friction. When the tangential slip is small, the contact acts in a nearly sticking regime with $\mu_{\text{eff}} \approx \mu_s$. As slip increases, friction decreases toward the dynamic coefficient μ_d . This transition is important for modeling the interplay between sticking, slipping, and momentary micro-impacts that occur when the barrel rotates over its contact edge. The ability to capture these slip transitions is essential for predicting how rotation accelerates or decays during descent.

The rigid-ground Simulink model therefore provides a computationally efficient framework for evaluating tumbling behavior when terrain does not deform. By removing soil mechanics, the model exposes the influence of rigid-body inertia, geometry, and contact parameters on the rolling trajectory. It predicts nominal rolling speed, angular acceleration, and the stability of the descent path when the robot travels over firm ground. These predictions establish a baseline that can be directly compared with the more complex responses observed in granular terrain.

The outputs of the model include time histories of angular velocity, forward translational velocity, and the normal and tangential contact forces that govern energy exchange during impacts. The rolling trajectory on inclined rigid surfaces is recorded to assess whether the robot maintains a stable descent or exhibits lateral drift. These results provide a clear reference for evaluating the degree to which granular processes, such as sinkage and particle rearrangement, alter the expected motion.

In summary, the rigid-ground Simscape tumbling model acts as a fast predictive tool for rolling locomotion on hard terrain. Granular DEM simulations extend the same gait analysis to

realistic soil conditions by adding mass wasting, depth-dependent drag, and particle-scale deformation effects. Together, these models form the comparative foundation used throughout the thesis to understand the mechanics of tumbling on rigid and deformable terrain.

3.14 Introduction to Project Chrono DEM-Engine

To investigate the highly dynamic interaction between the COBRA robot and loose granular terrain during tumbling, this thesis incorporates simulations based on the Discrete Element Method (DEM). DEM provides a particle-level representation of soil mechanics and allows the terrain to deform, collapse, compact, and redistribute in response to robot motion. Although the primary emphasis of this thesis is sidewinding on deformable but continuum-style terrain models presented earlier in Sections 3.6 through 3.10, analysis of tumbling in granular media is included due to its strong relevance to understanding contact mechanics under high energy, large deformation, and partially submerged conditions.

Prior to engaging with the granular model, a rigid-ground baseline for tumbling was established using MATLAB Simulink, as described in Section 3.13. This baseline isolates the geometric and inertial effects of tumbling on hard slopes and provides a clean reference against which the additional challenges posed by loose soil may be interpreted. These challenges include increased slip as particles rearrange beneath the rolling shell, deeper sinkage that changes the effective rolling radius, and momentum loss due to drag forces generated by particle impacts.

The Chrono DEM-Engine is a GPU-accelerated granular simulation system designed for high-throughput computation with large particle counts [37]. In DEM, the soil is represented as a collection of discrete spherical or polyhedral particles that interact through explicit contact laws. These interactions include normal and tangential collision forces, frictional resistance, cohesive behavior if specified, and velocity-dependent damping. Because the method resolves particle contacts directly rather than through continuum approximations, DEM naturally captures phenomena such as localized shear planes, non-uniform sinkage, intermittent yielding, and particle flow that forms around bodies undergoing rapid motion.

This level of modeling detail is essential for tumbling because the robot operates in a regime where its outer shell repeatedly strikes, compresses, and shears through layers of granular material. As the closed-loop body descends a slope, particles are displaced both vertically and laterally, forming temporary force chains that bear load until they collapse under stress. These force chains strongly influence stability by either supporting the robot briefly or allowing rapid loss of

CHAPTER 3. METHODOLOGY

support when they fail. DEM is capable of reproducing these effects because each grain contributes individually to the evolving stress network within the soil.

Further, DEM captures depth-dependent reaction forces that arise when parts of the robot become partially buried during tumbling. The resistance experienced by the shell depends on the number, depth, and compaction of particles in contact, all of which evolve dynamically as the body rolls. The rigid-ground model cannot reproduce these effects, since it assumes uniform contact with no penetration or granular flow. DEM therefore serves as the high-fidelity tool required to evaluate how loose sand modifies the descent trajectory, reduces overall momentum, and shapes the stability of rolling on steep inclines.

Including the DEM analysis in this thesis provides a complementary perspective on terrain–robot interaction. While the SCM model describes soft soil behavior using continuum-inspired pressure–sinkage and shear laws appropriate for sidewinding, DEM extends the modeling fidelity to situations involving deep penetration, large soil displacements, and rapid particle rearrangement. This multi-resolution approach, combining rigid, compliant, and particle-resolved terrain models, supports a holistic understanding of COBRA’s mobility across its full range of gaits.

Validated DEM simulation results are summarized in Chapter 4, where they are compared with experimental behavior to assess how well particle-level terrain modeling reproduces the contact forces and motion characteristics observed during physical tumbling trials.

3.15 DEM Terrain Workflow

To support the contact modeling perspective of this thesis, this section presents the GPU-accelerated Discrete Element Method (DEM) simulations used to analyze tumbling locomotion in granular terrain. These simulations were originally developed and validated in the AISJ tumbling study [16], and although no new DEM computations were generated specifically for this thesis, the results remain essential because tumbling involves deep penetration, rapid momentum exchange, and large soil displacements that cannot be approximated by any continuum model such as SCM. DEM’s particle-resolved formulation is uniquely capable of capturing these behaviors, making it the correct tool for analyzing high-energy rolling motion in loose sand.

DEM models the terrain as an ensemble of discrete grains whose positions, velocities, and contact forces evolve according to history-dependent interaction laws. This representation is critical for tumbling, because rolling motion causes soil to compact, dilate, shear, and collapse beneath the robot, forming force chains that intermittently support the body before failing under load. As the

CHAPTER 3. METHODOLOGY

robot rotates downslope, particles are displaced both vertically and laterally, creating drag forces, sinkage gradients, and slip episodes that strongly influence stability and descent speed.

The DEM Engine used in this work implements a dual-thread GPU architecture that separates geometry updates from granular physics evaluation. Two asynchronous threads operate in parallel: the Kinematic Thread (kT) and the Dynamic Thread (dT). The kT is responsible for updating the robot's rigid-body motion and feeding the geometry into the granular solver, while the dT handles particle collisions, contact forces, and time integration. A conceptual overview of this architecture is shown in Figure 3.8. The separation of these responsibilities increases throughput and allows the simulation to handle millions of particles efficiently, which is essential for capturing deep penetration and large soil deformation during tumbling.

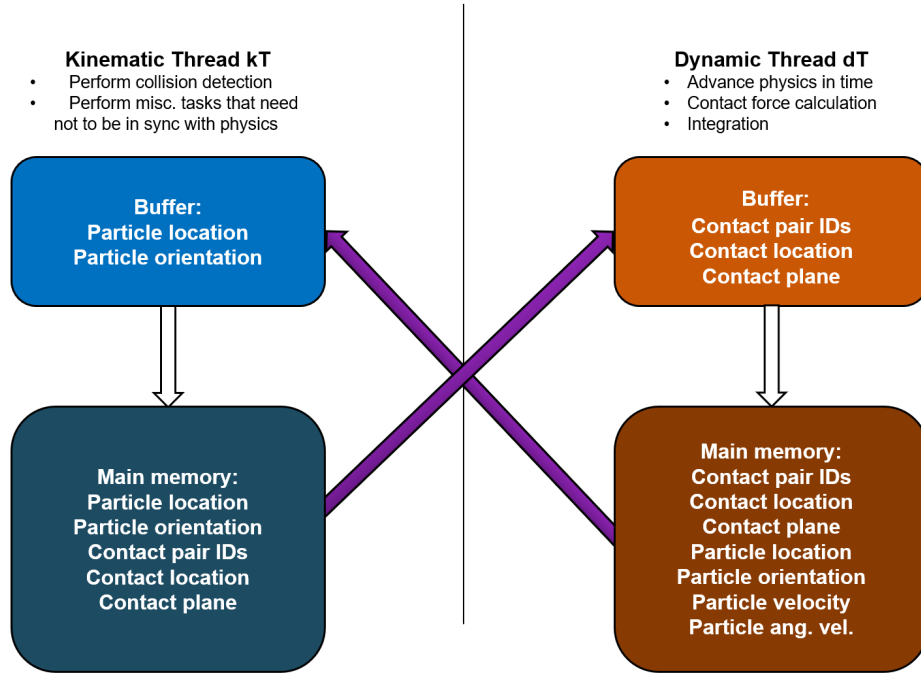


Figure 3.8: Conceptual dual-thread GPU architecture used by the DEM Engine. The Kinematic Thread supplies robot geometry and motion, while the Dynamic Thread resolves particle contacts and integrates the granular system. Inspired by [37].

3.15.1 Simulation Workflow Overview

The DEM simulations used in the AISJ study [16] follow a structured workflow that separates material definition, terrain generation, and robot motion input. This pipeline, illustrated in Figure 3.9, proceeds in several stages. First, the material properties of the granular medium are defined, including particle density, Young’s modulus, Poisson ratio, and friction. These parameters control how stiff or compliant grain–grain collisions are and govern the angle of repose of the resulting granular bed. A Young’s modulus that is too large causes excessively rigid collisions and unrealistic bouncing. A modulus that is too small produces overly soft grains that absorb too much energy and flatten under load. Poisson ratio influences the lateral expansion of particles under compression and therefore affects packing behavior and bulk density. Friction determines the resistance to sliding between grains and directly controls the angle of repose and shear stability of the slope.

Next, clump templates are created. A clump is a rigid aggregate of spheres that moves as a single body. Clumps capture the irregularity of real sand grains better than single spheres do. Real grains are angular and interlock under load, and clumps approximate this behavior by presenting multiple overlapping contact patches. Using clumps increases computational cost slightly but dramatically improves bulk soil behavior, especially during shear and slope failure.

The granular domain is then populated by randomly depositing clumps into a virtual container and allowing them to settle under gravity. This procedure generates a realistic sand bed whose density and porosity depend on friction, grain shape, and the deposition protocol. Once settled, the container boundaries are removed or reconfigured to form the experimental terrain.

The robot geometry is imported next. The COBRA rolling configuration is added as a collision shape. Because the tumbling motion is prescribed in these simulations, actuation is not necessary. Instead, a motion input is applied at the head link to rotate the connected circular structure. This prescribed motion ensures that the robot follows a consistent tumbling pattern and allows direct comparison across different soil conditions.

As the simulation proceeds, the kinematic thread updates the robot’s position and orientation according to the prescribed tumbling motion. The dynamic thread computes particle contacts and integrates all grain trajectories. Forces arising from grain impacts, drag, sinkage, and mass redistribution are recorded and mapped onto the robot. Output particle trajectories, grain velocities, collisions, and reaction forces form the basis for later analysis.

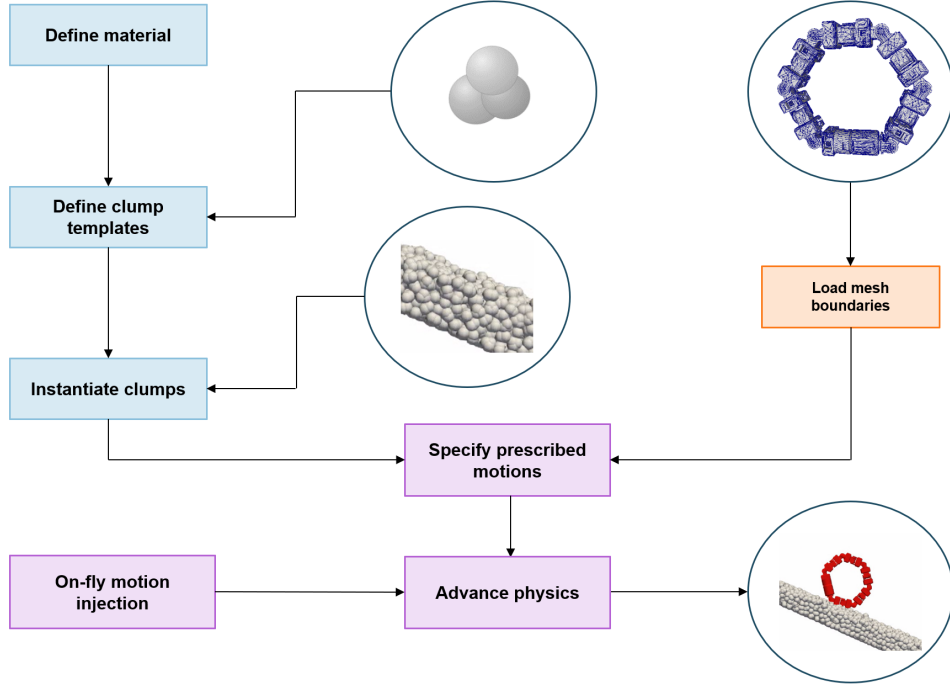


Figure 3.9: Conceptual workflow of a DEM simulation including grain generation, clump instantiation, boundary settling, and motion prescription. Adapted from [37].

3.15.2 Particle–Particle Contact Mechanics

DEM represents the interaction between particles using nonlinear contact laws in both the normal and tangential directions. Figure 3.10 illustrates the conceptual model. When two particles overlap, the penetration depth δ_n represents how far their surfaces intersect. This overlap is a numerical construct used to compute elastic and damping forces. The normal force is given by

$$F_n = k_n \delta_n - d_n \dot{\delta}_n,$$

where k_n is the normal stiffness and determines how strongly particles push back as they compress. A larger stiffness produces sharper collisions and higher energy transfer. The damping parameter d_n dissipates kinetic energy and reduces rebound, ensuring that particles do not oscillate unrealistically during settling or impacts.

Tangential forces arise from shear displacement. The DEM engine maintains a history variable j , which stores tangential slip accumulated over the contact duration. The tangential force is computed as

$$F_t = \min(\mu F_n, k_t j),$$

where k_t is the tangential stiffness and determines how shear resistance builds up as grains attempt to slide. The friction coefficient μ provides a Coulomb limit. When $k_t j < \mu F_n$, grains stick and shear elastically. When the threshold is exceeded, grains slide, producing plastic shear and rearranging the granular structure. This formulation is essential for modeling slope collapse, intermittent jamming, and the highly discontinuous nature of rolling motion through sand.

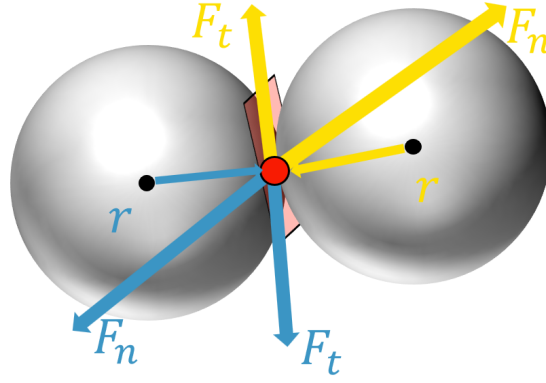


Figure 3.10: Conceptual representation of DEM particle contact mechanics, showing normal and tangential components of the interaction. Inspired by [37].

3.15.3 DEM Clump Types

Chrono DEM supports different clump styles for representing grains. Single-sphere clumps compute quickly but unrealistically smooth out shear resistance and underestimate angle-of-repose behavior. Irregular multi-sphere clumps, used in the AISJ work [16], offer a closer approximation to natural sand grains by producing multiple contact surfaces and greater interlocking. More advanced grain templates based on measured sand geometry have also been studied in [37]. For the purposes of the tumbling analysis, three-sphere clump templates were chosen because they balance computational efficiency with realistic bulk shear strength and sinkage properties. These templates were tuned so that the resulting granular bed matches observed sinkage depths and resistance forces encountered during hardware tumbling tests of the COBRA robot.

Although the DEM results used in this thesis originate from earlier work rather than newly

executed simulations, their inclusion is essential because they provide detailed insight into extreme granular interactions that complement the SCM-based sidewinding analysis. Together, SCM and DEM demonstrate how soil mechanics influence the spectrum of COBRA’s mobility modes, from smooth, low-energy sidewinding on soft terrain to vigorous rolling through deep, yielding sand.

3.16 DEM Terrain Mathematical Formulation

The granular terrain model used in this thesis follows the same Discrete Element Method (DEM) formulation that was developed for the COBRA tumbling study. It is included here because the particle-resolved physics directly support the contact modeling viewpoint of this work, particularly in situations involving deep penetration, rolling impacts, and nonlinear soil resistance. Although no new DEM experiments were generated specifically for this thesis, the validated formulation is reproduced here for clarity and reproducibility.

DEM treats the soil as a collection of discrete particles whose interactions are resolved using history-dependent contact mechanics. Each particle may represent a single grain or a clump of spheres, and its motion evolves according to Newton’s laws subject to contact forces, damping, and friction. This approach is crucial for modeling tumbling, where the robot rolls into and through loose sand, causing grains to rearrange, compact, and flow in ways that continuum models such as SCM cannot capture. DEM naturally reproduces jamming, force-chain formation, dilatancy, and yielding, all of which strongly influence tumbling behavior.

Normal Contact Force. Consider two spheres with radii r_i and r_j , positions \mathbf{x}_i and \mathbf{x}_j , and relative velocity \mathbf{v}_{ij} . The unit normal vector at the point of contact is

$$\hat{\mathbf{n}} = \frac{\mathbf{x}_i - \mathbf{x}_j}{\|\mathbf{x}_i - \mathbf{x}_j\|},$$

and the normal overlap, or penetration depth, is

$$\delta_n = r_i + r_j - \|\mathbf{x}_i - \mathbf{x}_j\|.$$

The overlap δ_n is not a physical interpenetration but a numerical device used to compute the elastic repulsion between grains. When $\delta_n > 0$, a force in the normal direction is applied:

$$\mathbf{F}_n = k_n \delta_n \hat{\mathbf{n}} - d_n (\hat{\mathbf{n}} \cdot \mathbf{v}_{ij}) \hat{\mathbf{n}} \quad (3.21)$$

CHAPTER 3. METHODOLOGY

where k_n is the normal stiffness and determines how strongly grains push back against compression. Higher stiffness produces sharper, more impact-like collisions and increases the effective bulk stiffness of the granular bed. The damping coefficient d_n controls the rate at which kinetic energy is lost during collisions. A sufficiently large d_n prevents unrealistic bouncing and ensures stable settling of particles under gravity.

The quantity $\hat{\mathbf{n}} \cdot \mathbf{v}_{ij}$ represents the approach speed between particles along the line of action. The damping term opposes this approach velocity, absorbing energy and dissipating oscillations. Together, the elastic and damping components define the normal repulsive behavior and play a critical role in the formation and collapse of force chains beneath the robot.

Tangential Contact Force with Shear Accumulation. Tangential forces are derived from the history of shear deformation. The DEM engine maintains a shear displacement vector $\boldsymbol{\xi}$ at every active contact, which evolves according to the tangential slip velocity:

$$\dot{\boldsymbol{\xi}} = \mathbf{v}_t, \quad \mathbf{v}_t = \mathbf{v}_{ij} - (\hat{\mathbf{n}} \cdot \mathbf{v}_{ij}) \hat{\mathbf{n}}.$$

The vector \mathbf{v}_t captures the sliding motion that occurs as particles move past each other, and $\boldsymbol{\xi}$ accumulates over time, representing how far the grains have sheared since contact was initiated. This shear history enables DEM to capture displacement-dependent stick–slip transitions and nonlinear tangential resistance.

The proposed tangential force before friction limiting is

$$\mathbf{F}_t^{\text{prop}} = -k_t \boldsymbol{\xi} - d_t \mathbf{v}_t,$$

where k_t is the tangential stiffness. This parameter determines how rapidly shear resistance builds up as grains resist sliding. The tangential damping d_t dissipates energy associated with lateral motion and prevents high-frequency oscillations. Together, these terms model the elastic and viscous components of shear interaction.

The actual tangential force must satisfy Coulomb friction:

$$\mathbf{F}_t = \begin{cases} \mathbf{F}_t^{\text{prop}}, & \|\mathbf{F}_t^{\text{prop}}\| \leq \mu \|\mathbf{F}_n\|, \\ -\mu \|\mathbf{F}_n\| \frac{\mathbf{v}_t}{\|\mathbf{v}_t\| + \epsilon_v}, & \text{otherwise,} \end{cases} \quad (3.22)$$

where μ is the friction coefficient, controlling the maximum tangential force before sliding occurs. The small constant ϵ_v ensures numerical stability when \mathbf{v}_t is close to zero. When $\|\mathbf{F}_t^{\text{prop}}\| <$

CHAPTER 3. METHODOLOGY

$\mu\|\mathbf{F}_n\|$, particles remain in a sticking regime and move together elastically. When the bound is exceeded, particles enter sliding, producing granular flow, shear bands, and avalanche-type behavior. These transitions are fundamental to tumbling, where rolling motion induces rapid shear stresses that propagate through the terrain.

Clump-Based Terrain Representation. Each DEM particle is modeled as a rigid clump composed of overlapping spheres. This representation allows the grains to exhibit angularity, local interlocking, and realistic dilatancy without the cost of polygonal mesh collisions. Clumps maintain a fixed internal structure, while individual sphere–sphere interactions between clumps generate distributed contact forces and torques. As the robot rolls, these interactions create complex load paths and transient support patterns. Clumps also enhance the angle-of-repose behavior of the granular bed, ensuring that slopes collapse and reform in ways consistent with real sand.

Clump-based terrain is particularly important for modeling tumbling, because the robot experiences momentary partial burial and must push through grains that compact and shear around its body. The ability to represent force chains and localized yielding enables DEM to capture the intricate terrain responses that arise during high-energy, multi-contact rolling motion.

This DEM formulation underlies all tumbling simulations referenced in this thesis. Although the simulations originate from prior published work, they are included here because the particle-level mechanics they capture provide high-fidelity insight into soil–robot interactions that cannot be reproduced using continuum approximations alone.

3.17 Empirical Parameters from Simulation Code

The DEM-based tumbling parameters presented here correspond exactly to the validated configuration used in the previously published COBRA tumbling study. Although no new granular simulations were produced specifically for this thesis, the same parameter set is reproduced to maintain transparency, enable reproducibility, and support the broader contact–interaction analysis developed throughout this work. These parameters govern particle stiffness, contact damping, friction, wheel dynamics, terrain generation, and solver behavior, all of which collectively determine the fidelity of the DEM environment.

3.17.1 Material Parameters

Two material classes are used: one to represent the robot link (approximated as a rigid wheel during tumbling) and one to describe the granular bed. These parameters regulate how stiff the interacting bodies are, how much energy is lost during collisions, and how strongly particles resist sliding.

Wheel Material.

$$E = 1 \times 10^9 \text{ Pa}, \quad \nu = 0.3, \quad \text{CoR} = 0.4, \quad \mu = 0.6, \quad C_{rr} = 0.02$$

Here, E is the Young's modulus providing normal stiffness of the wheel, ν is the Poisson ratio determining lateral contraction under load, CoR is the coefficient of restitution governing post-impact energy retention, μ is the friction coefficient controlling shear resistance, and C_{rr} is the rolling-resistance coefficient modeling micro-slip and internal losses during rotation.

Terrain Material.

$$E = 1 \times 10^8 \text{ Pa}, \quad \nu = 0.3, \quad \text{CoR} = 0.1, \quad \mu = 0.67, \quad C_{rr} = 0.05$$

For the granular bed, E is softer to represent yielding regolith, $\text{CoR} = 0.1$ reflects highly dissipative grain impacts, $\mu = 0.67$ matches typical dry sand friction, and the larger C_{rr} captures energy lost to grain rearrangement and void collapse.

Pairwise wheel-terrain interaction parameters are

$$\mu_{\text{wheel/terrain}} = 0.67, \quad \text{CoR}_{\text{wheel/terrain}} = 0.2.$$

Here, $\mu_{\text{wheel/terrain}}$ is the friction coefficient at the interface, and $\text{CoR}_{\text{wheel/terrain}}$ dictates impact dissipation between rigid and granular bodies.

3.17.2 Gravitational and World Settings

The simulation uses Earth gravity

$$g = 9.8 \text{ m/s}^2,$$

where g denotes gravitational acceleration. The domain dimensions are

$$L_x = 5 \text{ m}, \quad L_y = 1 \text{ m}, \quad L_z = 3 \text{ m},$$

CHAPTER 3. METHODOLOGY

with L_x, L_y, L_z representing the longitudinal, lateral, and vertical extents of the granular bed. The inclined plane angle

$$\theta = 24^\circ$$

defines the slope on which tumbling occurs and determines the gravitational component driving downhill motion.

Wheel (Tumbling Body) Properties

The tumbling body is modeled as a rigid cylindrical wheel with

$$r = 0.20 \text{ m}, \quad w = 0.12 \text{ m}, \quad m = 6.0 \text{ kg},$$

where r is radius, w is width, and m is total mass.

The principal moments of inertia are

$$I_{yy} = 0.75 mr^2, \quad I_{xx} = I_{zz} = m \left(0.4r^2 + \frac{w^2}{12} \right),$$

where I_{yy} corresponds to rotation about the axis of rolling, and I_{xx}, I_{zz} correspond to lateral and vertical rotational axes. These inertia values dictate angular acceleration, rotational stability, and momentum exchange with the terrain.

3.17.3 Particle-Based Terrain Settings

The granular bed uses particle density

$$\rho = 2600 \text{ kg/m}^3,$$

where ρ is the intrinsic mass density of sand-like grains. Before scaling, each clump template has volume

$$V = 4.2520508 \text{ m}^3,$$

with V denoting the multisphere aggregate volume. The scale factor

$$s = 0.02$$

uniformly shrinks particle dimensions so that actual DEM grains reach millimeter-scale sizes. The triangular-flat multisphere clump shape introduces angularity to model shear resistance, and `HCP-Sampler` initializes a hexagonal close-packed distribution to minimize voids.

3.17.4 Time Integration Settings

The timestep used is

$$h = 5 \times 10^{-6} \text{ s},$$

where h ensures stability during stiff collisions. Velocity caps

$$|v|_{\max} = 20 \text{ m/s}, \quad |v|_{\text{error}} = 35 \text{ m/s},$$

limit excessive particle acceleration; $|v|_{\max}$ is the physical bound, while $|v|_{\text{error}}$ is a safety threshold for unstable events. Collision detection updates occur every 40 solver iterations, and adaptive frequency is disabled to ensure consistent numerical behavior.

3.17.5 Wheel Actuation in Tumbling Mode

The prescribed angular velocity is

$$\omega_r = \frac{\pi}{4} \text{ rad/s}, \quad v_{\text{ref}} = \omega_r r,$$

where ω_r sets the rolling rate and v_{ref} is the tangential speed at the wheel's rim. The wheel is constrained to translate only along the y -axis and rotate only about the y -axis, ensuring motion remains planar.

3.17.6 Output Logging

Simulation outputs are captured at

$$10 \text{ FPS},$$

where FPS denotes frames per second. Logged data include particle positions (CSV), contact mesh states (VTK), and wheel force and kinematic histories. The simulation runs until

$$t_{\text{end}} = 14 \text{ s},$$

where t_{end} specifies total simulated duration.

This parameter set provides the complete specification necessary to reproduce the granular tumbling simulations and is included here because it characterizes the extreme terrain–interaction regimes that complement the primary sidewinding analysis presented in this thesis.

3.18 Simulation Loop

The DEM tumbling simulation follows a high-frequency update loop where particle dynamics, collision resolution, and wheel motion are integrated in parallel on the GPU. Algorithm 2 summarizes the simulation workflow used for COBRA rolling locomotion.

Algorithm 2 DEM Simulation Loop (GPU-Accelerated)

Require: Clump templates, particle distribution, robot wheel geometry,

- 1: soil material parameters (k_n, k_t, μ, d_n) , gravity g ,
 - 2: simulation time step h , total duration T

 - 3: Initialize Chrono DEM system and spatial hashing grid
 - 4: Load granular bed (multi-sphere clumps) into domain
 - 5: Assign wheel rigid-body properties and initial pose
 - 6: Apply inclined boundary plane at slope θ
 - 7: Configure GPU contact kernels and logging channels
 - 8: **for** $t = 0 \rightarrow T$ **with step** h **do**
 - 9: Update wheel kinematic constraint: $\omega_r \leftarrow \pi/4$ rad/s
 - 10: Advance wheel motion DOF (translation constrained, rotation free)
 - 11: Kinematic thread (kT) updates geometry positions in GPU buffers
 - 12: **Dynamic thread (dT):**
 Detect particle–wheel and particle–particle neighbors
 Compute overlaps δ_n and shear increments $\dot{\xi}$
 Resolve normal/tangential forces via Eqs. (3.21)–(3.22)
 Accumulate per-body contact wrench on wheel
 - 13: Velocity and position update using explicit integration
 - 14: Enforce domain bounds and delete escaped particles
 - 15: **if** frame_output triggered **then**
 - 16: Export particle states (CSV) and terrain mesh (VTK)
 - 17: Log wheel COM trajectory, forces, and slip state
 - 18: **end if**
 - 19: **end for**
 - 20: Save final dataset and performance statistics
-

The dual-thread GPU execution (kinematic vs. dynamic updates) ensures efficient neighbor search and force computation even for large particle counts. With a timestep of $h = 5 \times 10^{-6}$ s and optimized broad-phase culling, the solver maintains stable dynamics under transient impact and deep soil penetration conditions, which are characteristic of COBRA’s tumbling mode.

3.19 Simulation Details

The DEM-based tumbling simulation is implemented in a modular Chrono setup that allows granular physics to interact with a simplified rigid-body representation of the robot in its circular tumbling configuration. The modular design keeps the system easy to configure, reproduce, and extend, while also ensuring that the granular terrain and the wheel-shaped robot body exchange forces in a physically meaningful way.

The core components of the simulation include the DEM physics engine, the rigid-body wheel model, the broad-phase collision system, and the logging interface. The DEM engine runs entirely on the GPU and computes particle interactions, collision forces, and momentum transfer at every timestep. The wheel model represents the closed-loop shape formed when the head and tail of the robot are connected, and it experiences the same soil resistance and impact forces as it would during real tumbling. A spatial hashing grid is used for broad-phase collision detection so that only nearby particles are considered for contact evaluation, which keeps computational cost manageable. The logging interface continuously records particle states, wheel kinematics, and force histories so that the resulting data can be analyzed afterward.

Several input assets are required to initialize the simulation. These include multi-sphere clump templates that approximate the shape and frictional behavior of granular particles, a terrain initialization routine that distributes particles using a hexagonal close-packing pattern, and wheel geometry with mass and inertia properties matching the tumbling configuration. Material parameters for both particles and the wheel reflect loose sand behavior and are selected to match real sinkage and shear responses. A control script defines the slope angle, the permitted degrees of freedom for the wheel, and the format of the output data.

The execution pipeline begins with the creation of the granular domain, assignment of gravity, and definition of the inclined plane. Motion constraints are then imposed on the wheel so that it rolls down the slope in a controlled manner. Once the solver begins running, particle contacts and wheel interactions are evaluated at every timestep using the GPU kernels. All relevant outputs, including particle rearrangement, wheel motion, and contact forces, are written to log files. After

CHAPTER 3. METHODOLOGY

the simulation completes, the data are processed to extract sinkage trends, rolling distance, and other behavioral metrics.

The output data describe the evolution of wheel position, velocity, and orientation, along with detailed measurements of particle flow patterns and mound formation around the rolling body. The contact force history provides insight into how the wheel interacts with loose soil during each phase of the tumble, while solver performance statistics indicate how efficiently the GPU-based system handled the simulation.

These simulations illustrate the particle-scale mechanisms that govern tumbling on loose terrain. They complement the SCM-based analysis of sidewinding by providing a higher fidelity view of soil resistance, flow, and momentum exchange that cannot be captured with a continuum model. The combination of both approaches establishes a coherent and consistent understanding of how COBRA interacts with soft terrain across its different locomotion modes.

Chapter 4

Results

This chapter presents a comprehensive evaluation of the COBRA robot’s locomotion across two distinct gait modalities, namely sidewinding and tumbling. The analyses combine rigid-ground modeling, deformable-terrain simulations, and physical experiments conducted on real sand. Taken together, these studies illustrate how changes in terrain mechanics, from fully rigid support to compliant continuum deformation and finally to fully particulate flow, influence the robot’s ability to generate traction, maintain stability, and move effectively in unstructured environments.

The sidewinding results compare Simscape Multibody rigid-ground simulations, Project Chrono SCM deformable-terrain simulations, and hardware experiments on both laboratory flooring and loose sand. These comparisons highlight how compliance alters load transfer, contact persistence, and stride efficiency. The tumbling results combine Simscape rigid-ground models with high-fidelity Chrono DEM simulations, enabling detailed study of rolling stability, granular drag, and mass-wasting behavior on steep slopes. Together, these results span the transition from structured frictional contact to fully granular yielding, offering a unified perspective on COBRA’s locomotion mechanics.

The overarching objective of this chapter is to determine how different terrain models influence predicted kinematics, contact forces, and overall locomotion performance. By quantifying the divergence between rigid, continuum, and particle-based models—and validating each against experiment—this chapter establishes when simplified contact models suffice for predictive reasoning and when high-fidelity granular simulation becomes necessary.

4.1 Qualitative Gait Replication in Simulation

Figures 4.1 and 4.2 illustrate sidewinding snapshots generated using Chrono SCM for two gait frequencies. In both cases, the traveling lateral wave is clearly reproduced, and the phase relationship between head and tail motion matches experimental observations. On deformable terrain, however, the robot's links leave visible permanent depressions as they press into the soil. These depressions deepen when amplitudes increase and produce detectable lateral berms along the swept path.

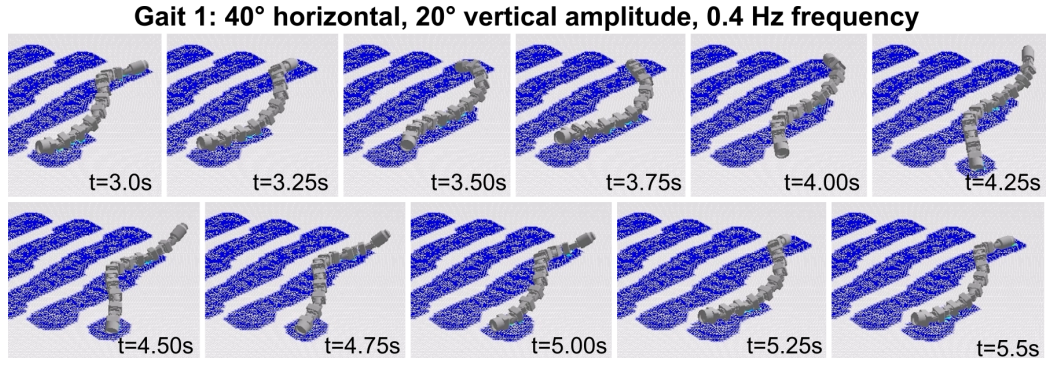


Figure 4.1: SCM simulation snapshots for Gait 1 (0.4 Hz). Blue shading highlights terrain depression caused by link loading. *Image courtesy of Adarsh Salagame.*

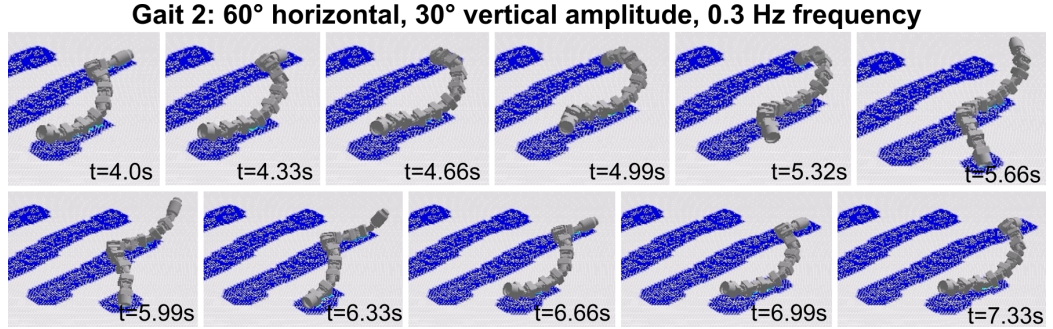


Figure 4.2: SCM simulation snapshots for Gait 2 (0.3 Hz). Increased amplitudes lead to greater sinkage and lateral soil displacement. *Image courtesy of Adarsh Salagame.*

This phenomenon is entirely absent in rigid-terrain simulations, where ground reaction forces act instantaneously without modifying the terrain. The SCM results therefore capture a key physical mechanism present in real sand: compliant ground reduces the firmness of the anchoring points that sidewinding relies upon, leading to reduced forward progression per cycle.

Despite the presence of sinkage and drag, the SCM model faithfully reproduces the high-level kinematic structure of the gait. The head, mid-body, and tail segments maintain the alternating tripod-like contact structure characteristic of efficient sidewinding. This indicates that although terrain compliance changes local force magnitudes, the global kinematic template remains stable, demonstrating that the gait is robust to moderate substrate deformability.

4.2 Contact Mechanics and Load Redistribution

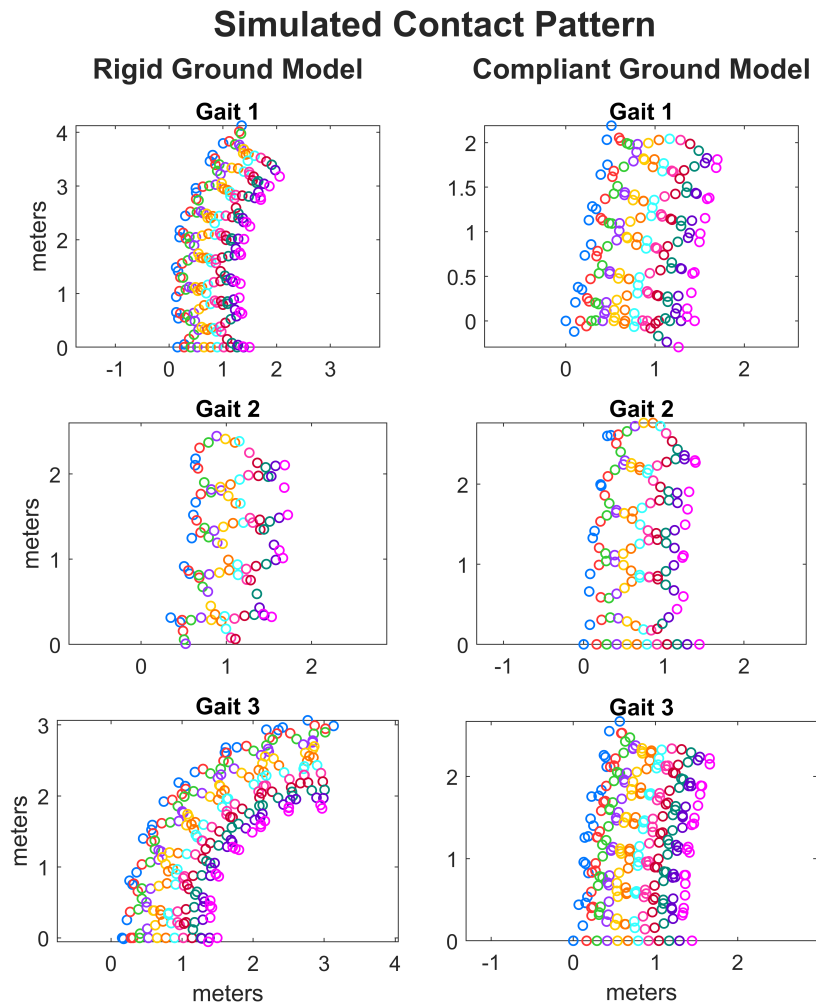


Figure 4.3: Contact distribution over one gait cycle. Deformable terrain results in wider and more diffused loading regions.

The contact-location comparison in Fig. 4.3 reveals a notable contrast between rigid and

CHAPTER 4. RESULTS

deformable terrain. On rigid ground, contact points are discrete and localized. Each link establishes a short-duration, high-stiffness contact that cleanly transfers load to the surface. In contrast, SCM produces spatially broader and temporally longer loading patches. As the body sinks, neighboring nodes share the load, distributing contact over a larger region. This diffused interaction reduces the sharp force spikes observed in rigid-ground simulations and experiments on hard surfaces.

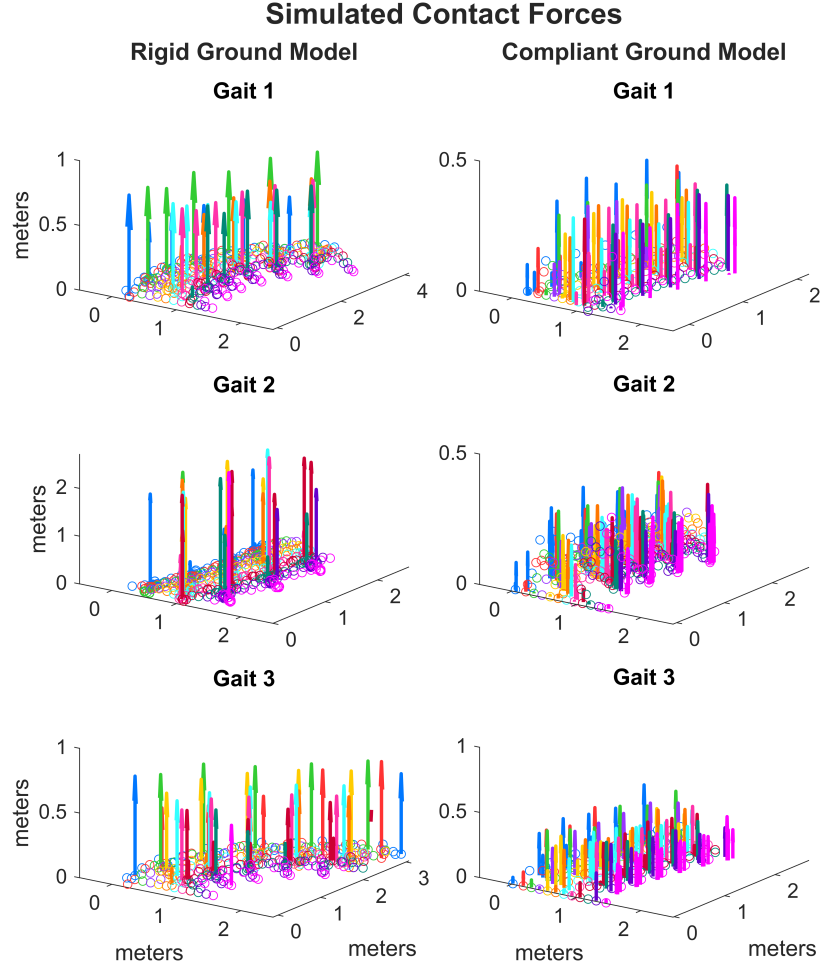


Figure 4.4: Comparison of ground reaction forces. Deformable terrain decreases peak forces and spreads loading temporally.

Normal force profiles in Fig. 4.4 further highlight this behavior. While all models exhibit periodic force oscillations aligned with the gait cycle, deformable terrain consistently lowers peak force magnitudes. This reduction arises because the soil deforms plastically under compression, effectively attenuating high-frequency impacts and providing a cushioned interaction. Hardware trials on loose sand show similar signatures, validating the SCM predictions.

CHAPTER 4. RESULTS

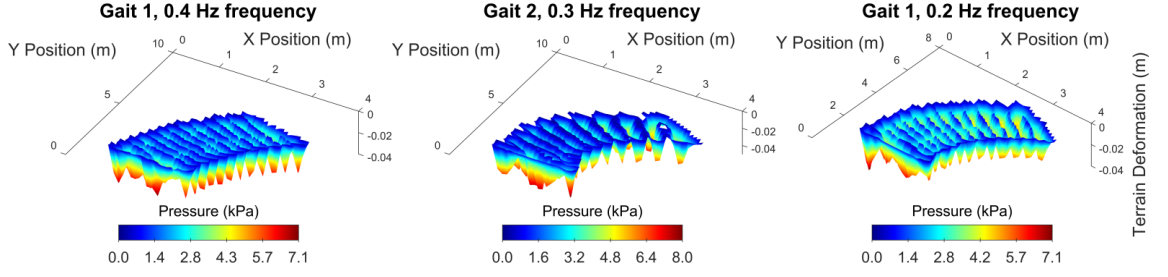


Figure 4.5: Contact pressure and permanent terrain depression over a gait cycle in Chrono SCM. Node-level sinking and smoothing are visible.

The pressure-field visualization in Fig. 4.5 gives additional insight into how local sinkage redistributes loading. Regions of high pressure cluster near inflection points in the body wave, where curvature is greatest and load transfer is most pronounced. Over time, these regions blend into smooth depressions due to plastic soil yielding. This permanent deformation mirrors experimental footage in which the robot leaves a characteristic sinusoidal trench along its path. The simulation therefore captures the essential terramechanics of sidewinding: contact patches expand, anchor quality decreases, and forward displacement per cycle diminishes.

4.3 Head Trajectory Comparisons

Figures 4.6 and 4.7 compare experimental and simulated head trajectories, revealing how terrain compliance alters both the magnitude and temporal structure of motion. The rigid-ground simulation closely matches laboratory rigid-surface experiments, demonstrating that frictional interaction alone is sufficient to predict high-level kinematics on hard floors. In contrast, SCM and real sand data show shorter forward displacement per cycle due to energy lost to soil deformation.

The normalized trajectories highlight that all cases preserve the alternating sweep-and-pause behavior intrinsic to sidewinding. However, compliant terrain introduces slight temporal delays in the sweeping phase as the body drags through displaced material. Experimental results show small deviations caused by reduced VIO reliability at low frequencies; nonetheless, the overall motion pattern remains consistent across environments. These comparisons establish that while terrain compliance alters locomotor efficiency, it does not destabilize the fundamental geometry of the gait.

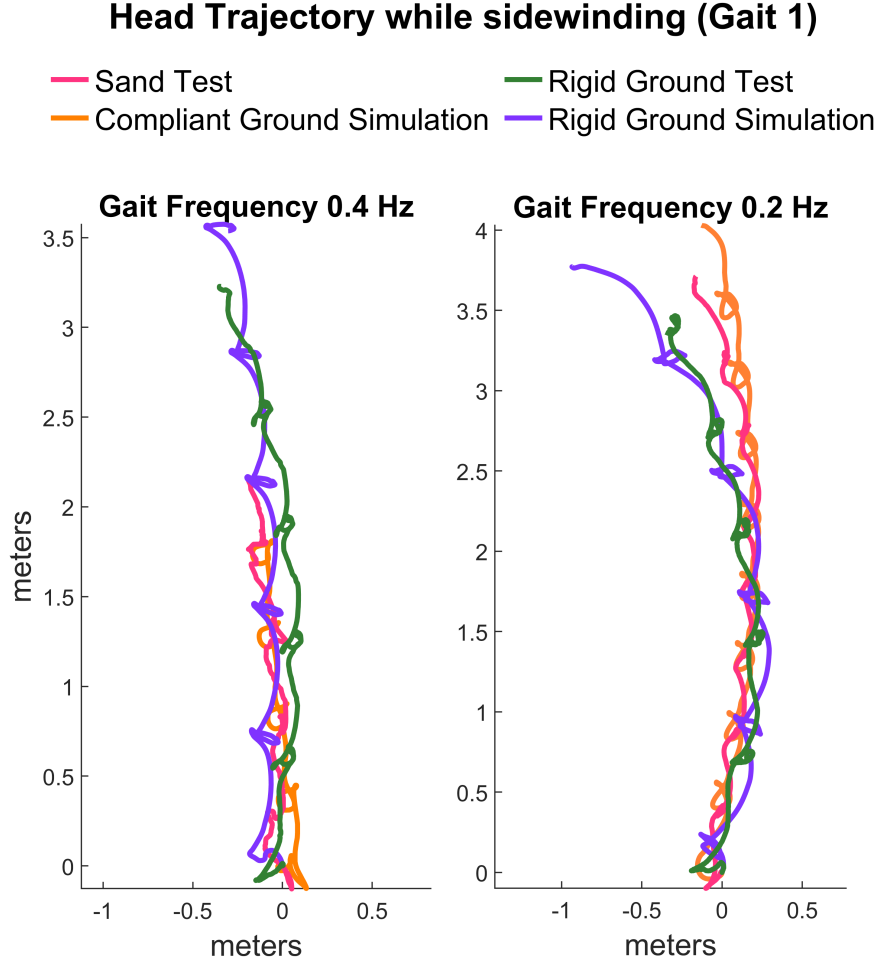


Figure 4.6: Comparison of head trajectories for Gait 1. Rigid-ground simulations closely match rigid-ground experiments; SCM captures compliant-ground trends.

4.4 Summary of Findings

The collective evidence from all simulations and experiments demonstrates that sidewinding is highly robust to substrate compliance. Directionality remains stable, the gait structure is preserved, and contact patterns follow the expected multi-anchor locomotion template. However, deformable terrain consistently reduces stride length due to slip, sinkage, and energy lost to soil re-arrangement. These findings justify a hierarchical modeling strategy: rigid-ground simplifications provide fast and reliable predictions for short-horizon control, while compliant models such as SCM are necessary when efficiency, traction limits, or long-duration behaviors are of interest.

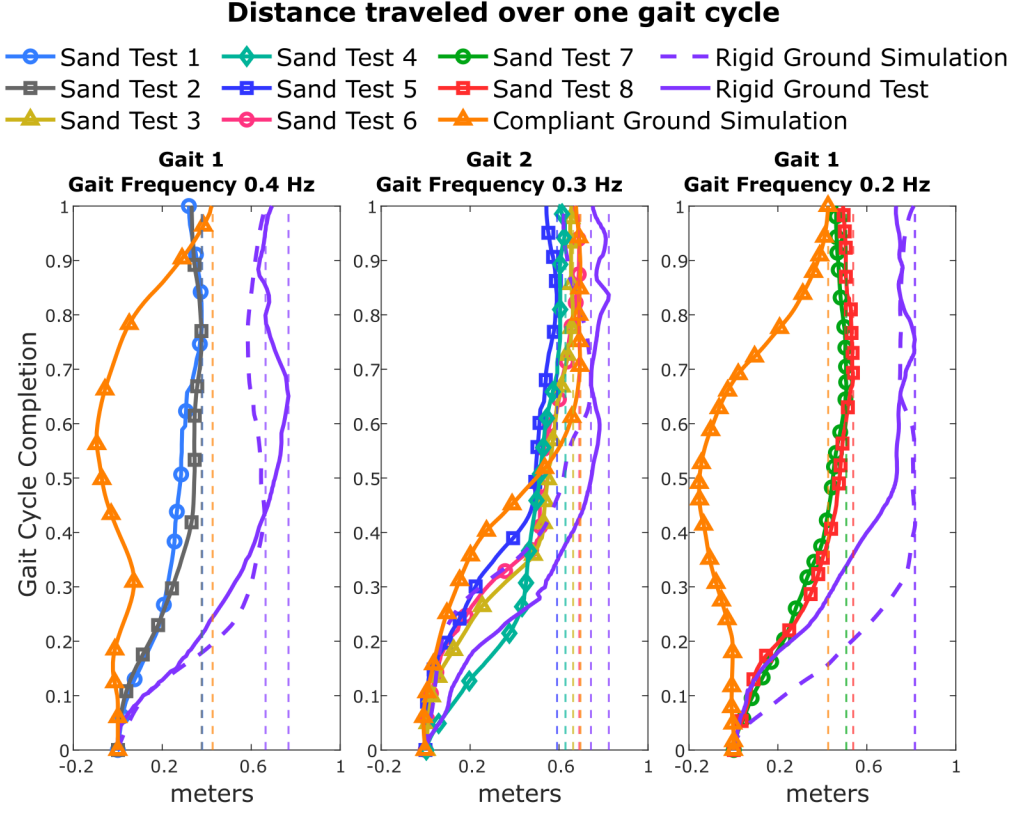


Figure 4.7: Normalized head trajectories over a gait cycle showing similar stationary and sweeping phases across all environments.

4.5 Tumbling Gait Results: Chrono DEM Engine

The tumbling analysis examines COBRA’s behavior on steep granular slopes, where rolling replaces sidewinding as the primary locomotion strategy. The DEM simulation in Fig. 4.8 reveals the complex particle–robot interactions that arise during this high-energy mode. As the robot descends a 24° slope, grains accumulate at the front surface, slide beneath the body, and disperse downslope as the shell rotates. These flows are hallmarks of mass-wasting phenomena observed in natural granular systems. The robot experiences partial burial during some phases, and local hills of displaced material form around its trajectory—behaviors impossible to capture with rigid or continuum soil models.

The quantitative comparison in Fig. 4.9 contrasts DEM with two Simscape models: a stiff rigid-ground case and a compliant-surface approximation. The rigid model predicts the fastest

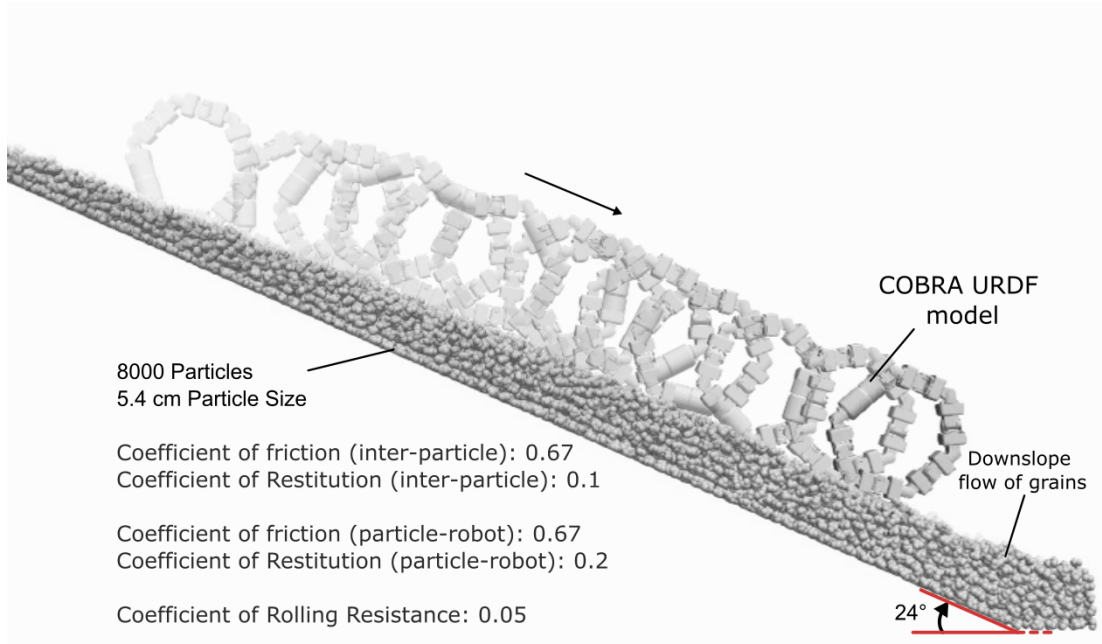


Figure 4.8: Chrono DEM simulation of COBRA tumbling downslope on loose granular terrain (24° inclination). Terrain deformation, mass-wasting, and body sinkage are visible. *Image courtesy of Adarsh Salagame.* [16]

descent because no energy is dissipated into the substrate. In contrast, the DEM simulation exhibits slower progression due to grain collision losses, slip at the contact interface, and drag arising from particle rearrangement. The compliant Simscape case is slowest because its damping forces are artificially large compared to true granular resistance, causing significant energy absorption that does not fully resemble physical sand behavior.

Vertical CoM motion offers further insight. In the DEM simulation, the CoM trajectory oscillates as the robot intermittently loses support while riding over sparse particle contact patches. These short ballistic phases correspond to airborne micro-transitions caused by local voids and grain slippage. Rigid models cannot replicate these effects because their support surface never fails under load. Compliant Simscape exhibits vertical oscillations but lacks the sharp discontinuities characteristic of true granular yielding.

Normal and friction forces reinforce this interpretation. On stiff ground, impacts generate very high-magnitude impulse spikes because collisions are perfectly localized and instantaneous. DEM attenuates these forces substantially, as grains absorb impact momentum by deforming, sliding, and scattering. The compliant Simscape model dampens impacts even further but does so

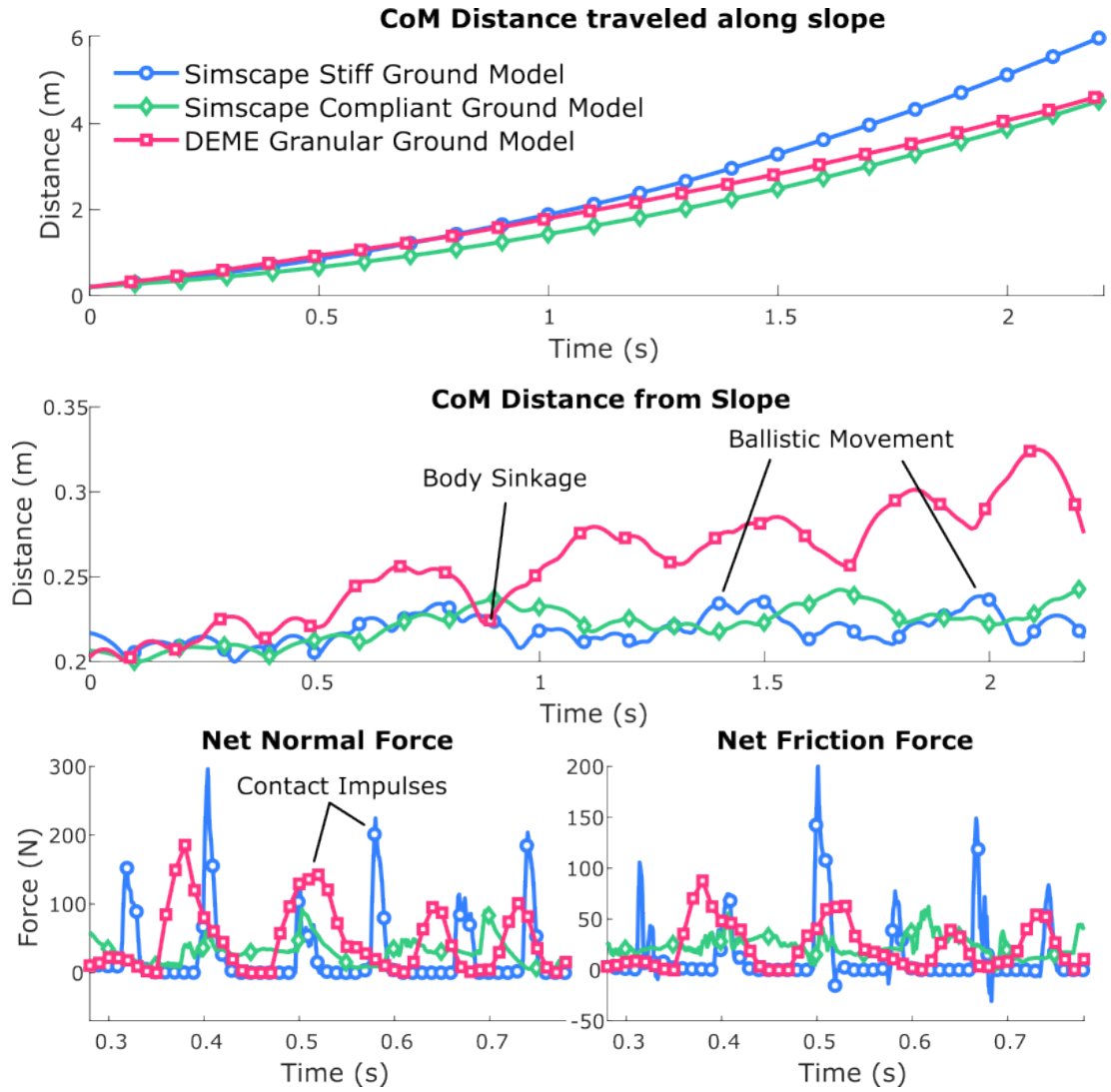


Figure 4.9: Comparison of tumbling dynamics across three models: Simscape stiff ground (blue), Simscape compliant ground (green), and Chrono DEM granular terrain (magenta). DEM results replicate body sinkage, dissipative energy loss, and reduced impact impulses observed in real sand. Image courtesy of Adarsh Salagame. [16]

CHAPTER 4. RESULTS

through a purely numerical mechanism, rather than physically meaningful grain-scale processes. DEM therefore provides a better qualitative and quantitative representation of the reaction loads expected during real rolling on sand.

Overall, the DEM results demonstrate that granular yielding plays a dominant role in moderating downhill acceleration and shaping the robot's rolling trajectory. The combination of reduced peak forces, intermittent lift, and drag-induced deceleration yields a physically realistic representation of tumbling mechanics on loose sand. Compared to Simscape models, DEM provides the only framework capable of capturing mass-wasting, energy dissipation through particle flow, and the emergent rheological behavior of real granular slopes.

Chapter 5

Conclusion

This thesis presented a unified modeling and simulation framework for analyzing the locomotion of the COBRA snake robot across rigid, compliant, and granular terrains. Two modes of mobility were studied: sidewinding for efficient planar traversal and tumbling for rapid descent on steep slopes. Together, these analyses demonstrated how terrain mechanics influence stability, slip, propulsion efficiency, and net displacement in contact-rich locomotion.

For sidewinding locomotion, MATLAB Simscape simulations on rigid ground accurately reproduced the primary kinematic patterns and directional movement of the robot. These results highlight that rigid-ground models are often sufficient for predictive control, where the objective is to estimate the net direction and magnitude of motion over short horizons. In contrast, simulations and experiments on soft sand showed that terrain yielding introduces slip and sinkage, reducing displacement per cycle. Project Chrono SCM simulations captured these effects by modeling normal and shear soil deformation, providing a closer representation of locomotion behavior on deformable ground.

In the high-energy tumbling locomotion mode, impacts and bulk soil flow become the dominant contributors to motion. While a rigid-ground Simulink model provides a clean baseline for motion prediction, the Chrono DEM engine revealed transient lift-off, grain rearrangements, and mass-wasting phenomena that strongly influence the descent rate and contact forces. These dynamics demonstrate that particle-level physics are required for accurate locomotion analysis during extreme terrain interactions and deep penetration events.

Across both locomotion modes, this work shows that the level of terrain fidelity required for simulation depends on the underlying mobility strategy:

CHAPTER 5. CONCLUSION

- **Rigid-ground models** remain well-suited for real-time planning and control design due to their computational efficiency and strong directional accuracy.
- **Continuum soil models** such as SCM enable correct prediction of slip, sinkage, and load redistribution effects that drive changes in locomotion efficiency.
- **DISCRETE particle-based models** such as DEM are necessary for high-energy and worst-case interactions where soil failure and bulk displacement dominate.

This hierarchical approach to locomotion modeling establishes a complete analysis pipeline that spans real-time motion prediction to high-fidelity terrain mechanics, forming a robust basis for future field deployment in uncertain environments.

5.0.1 Future Work

The research presented in this thesis opens multiple promising directions:

- **Closed-loop control on deformable terrain:** Integrating compliant-ground modeling into predictive controllers to improve slip compensation and stability.
- **Online terrain parameter estimation:** Using sensing and contact feedback to automatically adapt soil models for different substrates, improving robustness to environmental variability.
- **Multi-modal locomotion transitions:** Developing autonomous strategies for switching between sidewinding, tumbling, and other locomotion modes based on situational awareness.
- **GPU-accelerated granular simulation at larger scales:** Improving DEM resolution for more accurate representation of grain-scale failure and deep submersion events.
- **Field testing in planetary-analogue environments:** Extending validation beyond laboratory settings to steep slopes and crater-like sites with mixed and loose soil conditions.

5.0.2 Final Remarks

Through detailed modeling, rigorous simulation, and hardware validation, this thesis advances understanding of how a snake robot generates motion under varying terrain mechanics. The contributions support the long-term goal of deploying resilient, adaptive robotic systems capable of navigating challenging, unstructured environments where traditional mobility platforms fail. This

CHAPTER 5. CONCLUSION

work lays the foundation for reliable and versatile locomotion in robotics missions ranging from extraterrestrial exploration to search and rescue in disaster-stricken areas.

Bibliography

- [1] J. Whitman, N. Zevallos, M. Travers, and H. Choset, “Snake robots search for earthquake survivors in Mexico,” in *2018 IEEE International Symposium on Safety, Security, and Rescue Robotics (SSRR)*, IEEE, 2018, pp. 1–6.
- [2] C. Shin, P. W. Ferguson, S. A. Pedram, J. Ma, E. P. Dutson, and J. Rosen, “Autonomous Tissue Manipulation via Surgical Robot Using Learning Based Model Predictive Control,” in *2019 International Conference on Robotics and Automation (ICRA)*, May 2019, pp. 3875–3881.
- [3] J. Liu, Y. Tong, and J. Liu, “Review of snake robots in constrained environments,” *Robotics and Autonomous Systems*, vol. 141, p. 103 785, Jul. 2021.
- [4] Y. Jiang, Y. Jia, and X. Li, “Contact-Aware Non-Prehensile Manipulation for Object Retrieval in Cluttered Environments,” in *2023 IEEE/RSJ International Conference on Intelligent Robots and Systems (IROS)*, Oct. 2023, pp. 10 604–10 611.
- [5] N. Chavan-Dafle and A. Rodriguez, “Stable Prehensile Pushing: In-Hand Manipulation with Alternating Sticking Contacts,” in *2018 IEEE International Conference on Robotics and Automation (ICRA)*, May 2018, pp. 254–261.
- [6] M. Xiao, Y. Ding, and S. Fan, “One-Finger Manipulation of 3D Objects by Planning Start-to-Push Points and Pushing Forces,” *IEEE Robotics and Automation Letters*, vol. 9, no. 3, pp. 2694–2701, Mar. 2024.
- [7] M. Tesch et al., “Parameterized and Scripted Gaits for Modular Snake Robots,” *Advanced Robotics*, vol. 23, no. 9, pp. 1131–1158, Jan. 2009.
- [8] D. Rollinson, A. Buchan, and H. Choset, “Virtual Chassis for Snake Robots: Definition and Applications,” *Advanced Robotics*, vol. 26, no. 17, pp. 2043–2064, Dec. 2012.

BIBLIOGRAPHY

- [9] P. Wiriyacharoensunthorn and S. Laowattana, “Analysis and design of a multi-link mobile robot (Serpentine),” in *2002 IEEE International Conference on Industrial Technology, 2002. IEEE ICIT '02.*, vol. 2, Dec. 2002, 694–699 vol.2.
- [10] S.-W. Yoo, E.-I. Son, and S.-W. Seo, “Traversability-Aware Adaptive Optimization for Path Planning and Control in Mountainous Terrain,” *IEEE Robotics and Automation Letters*, vol. 9, no. 6, pp. 5078–5085, Jun. 2024.
- [11] D. D. K. Arachchige, D. M. Perera, U. Huzaifa, I. Kanj, and I. S. Godage, “Tumbling Locomotion of Tetrahedral Soft-Limbed Robots,” *IEEE Robotics and Automation Letters*, vol. 9, no. 5, pp. 4337–4344, May 2024.
- [12] G. Kim, D. Kang, J.-H. Kim, S. Hong, and H.-W. Park, *Contact-Implicit Model Predictive Control: Controlling Diverse Quadruped Motions Without Pre-Planned Contact Modes or Trajectories*, Oct. 2024.
- [13] M. Wang, A. Ö. Önel, P. Long, and T. Padır, “Contact-Implicit Planning and Control for Non-prehensile Manipulation Using State-Triggered Constraints,” in *Robotics Research*, Springer, Cham, 2023, pp. 189–204.
- [14] W.-C. Huang, A. Aydinoglu, W. Jin, and M. Posa, “Adaptive Contact-Implicit Model Predictive Control with Online Residual Learning,” in *2024 IEEE International Conference on Robotics and Automation (ICRA)*, May 2024, pp. 5822–5828.
- [15] J. J. Moreau, “Unilateral Contact and Dry Friction in Finite Freedom Dynamics,” en, in *Nonsmooth Mechanics and Applications*, J. J. Moreau and P. D. Panagiotopoulos, Eds., Vienna: Springer, 1988, pp. 1–82.
- [16] A. Salagame, H. Noyes, E. Sihite, A. Kalantari, and A. Ramezani, “Crater Observing Bioinspired Rolling Articulator (COBRA),” *Advanced Intelligent Systems*, vol. n/a, no. n/a, p. 2 500 352, Sep. 2025.
- [17] W. Huang, Y. Fang, X. Guo, H. Liu, and L. Liu, “A Unified Motion Modeling Approach for Snake Robot’s Gaits Generated With Backbone Curve Method,” *IEEE Transactions on Robotics*, pp. 1–15, 2024.
- [18] H. C. Astley et al., “Modulation of orthogonal body waves enables high maneuverability in sidewinding locomotion,” *Proceedings of the National Academy of Sciences*, vol. 112, no. 19, pp. 6200–6205, May 2015.

BIBLIOGRAPHY

- [19] H. Marvi et al., “Sidewinding with minimal slip: Snake and robot ascent of sandy slopes,” *Science*, vol. 346, no. 6206, pp. 224–229, Oct. 2014.
- [20] Z. Wang, B. Li, Y. Wang, and S. Ma, “Dynamic modeling for locomotion-manipulation of a snake-like robot by using geometric methods,” in *2009 IEEE/RSJ International Conference on Intelligent Robots and Systems*, Oct. 2009, pp. 3631–3636.
- [21] G. Yang, S. Ma, B. Li, and M. Wang, “A hierarchical connectionist CPG controller for controlling the snake-like robot’s 3-dimensional gaits,” in *2012 IEEE/RSJ International Conference on Intelligent Robots and Systems*, Oct. 2012, pp. 822–827.
- [22] F. Reyes and S. Ma, “Studying slippage on pushing applications with snake robots,” *Robotics and Biomimetics*, vol. 4, no. 1, p. 9, Nov. 2017.
- [23] F. Reyes and S. Ma, “On planar grasping with snake robots: Form-closure with enveloping grasps,” in *2014 IEEE International Conference on Robotics and Biomimetics (ROBIO 2014)*, Dec. 2014, pp. 556–561.
- [24] F. Reyes, W. Tang, and S. Ma, “Using a planar snake robot as a robotic arm taking into account the lack of a fixed base: Feasible region,” in *2015 IEEE/RSJ International Conference on Intelligent Robots and Systems (IROS)*, Sep. 2015, pp. 956–962.
- [25] M. Tanaka and F. Matsuno, “Cooperative control of two snake robots,” in *Proceedings 2006 IEEE International Conference on Robotics and Automation, 2006. ICRA 2006.*, May 2006, pp. 400–405.
- [26] N. M. Nor and S. Ma, “CPG-based locomotion control of a snake-like robot for obstacle avoidance,” in *2014 IEEE International Conference on Robotics and Automation (ICRA)*, May 2014, pp. 347–352.
- [27] J. Chen, B. Yin, C. Wang, F. Xie, R. Du, and Y. Zhong, “Bioinspired Closed-loop CPG-based Control of a Robot Fish for Obstacle Avoidance and Direction Tracking,” *Journal of Bionic Engineering*, vol. 18, no. 1, pp. 171–183, Jan. 2021.
- [28] Z. Yan, H. Yang, W. Zhang, Q. Gong, F. Lin, and Y. Zhang, “Bionic Fish Trajectory Tracking Based on a CPG and Model Predictive Control,” *Journal of Intelligent & Robotic Systems*, vol. 105, no. 2, p. 29, May 2022.
- [29] K. Zhu, L. Wu, C. Ren, X. Li, and S. Ma, “Path Following Controller for Snake Robots Based on Data-driven MPC and Extended State Observer,” in *2022 41st Chinese Control Conference (CCC)*, Jul. 2022, pp. 5592–5597.

BIBLIOGRAPHY

- [30] I. Tanev, T. Ray, and A. Buller, “Automated evolutionary design, robustness, and adaptation of sidewinding locomotion of a simulated snake-like robot,” *IEEE Transactions on Robotics*, vol. 21, no. 4, pp. 632–645, Aug. 2005.
- [31] R. Wang, W. Xi, X. Guo, and Y. Fang, “Path Following for Snake Robot Using Crawler Gait Based on Path Integral Reinforcement Learning,” in *2021 6th IEEE International Conference on Advanced Robotics and Mechatronics (ICARM)*, Jul. 2021, pp. 192–198.
- [32] M. Zanon and S. Gros, “Safe Reinforcement Learning Using Robust MPC,” *IEEE Transactions on Automatic Control*, vol. 66, no. 8, pp. 3638–3652, Aug. 2021.
- [33] J. Vorndamme, M. Schappler, and S. Haddadin, “Collision detection, isolation and identification for humanoids,” in *2017 IEEE International Conference on Robotics and Automation (ICRA)*, May 2017, pp. 4754–4761.
- [34] E. G. Gilbert, D. W. Johnson, and S. S. Keerthi, “A fast procedure for computing the distance between complex objects in three-dimensional space,” *IEEE Journal on Robotics and Automation*, vol. 4, no. 2, pp. 193–203, 1988.
- [35] J. L. Bentley, “Multidimensional binary search trees used for associative searching,” *Communications of the ACM*, vol. 18, no. 9, pp. 509–517, 1975.
- [36] N. Bucki, J. Lee, and M. W. Mueller, “Rectangular Pyramid Partitioning Using Integrated Depth Sensors (RAPPIDS): A Fast Planner for Multicopter Navigation,” *IEEE Robotics and Automation Letters*, vol. 5, no. 3, pp. 4626–4633, Jul. 2020.
- [37] G. Maurel and D. Negrut, “Chrono::DEME: A GPU-Accelerated Discrete Element Method Engine for Granular Dynamics,” *Computers & Geosciences*, vol. 184, p. 105 019, 2023.
- [38] C. Sunday et al., “Validation of the Chrono soft-sphere collision model for granular DEM simulations,” it, in DEU, 2019.
- [39] J. Zhang and S. Singh, “Laser–visual–inertial odometry and mapping with high robustness and low drift,” *Journal of Field Robotics*, vol. 35, no. 8, pp. 1242–1264, 2018.
- [40] K. Sun et al., “Robust Stereo Visual Inertial Odometry for Fast Autonomous Flight,” *IEEE Robotics and Automation Letters*, vol. 3, no. 2, pp. 965–972, Apr. 2018.
- [41] K. Mohta et al., “Experiments in Fast, Autonomous, GPS-Denied Quadrotor Flight,” in *2018 IEEE International Conference on Robotics and Automation (ICRA)*, May 2018, pp. 7832–7839.

BIBLIOGRAPHY

- [42] R. Krenn and G. Hirzinger, “SCM – A SOIL CONTACT MODEL FOR MULTI-BODY SYSTEM SIMULATIONS,” 2009.
- [43] R. Krenn and A. Gibbesch, “Soft Soil Contact Modeling Technique for Multi-Body System Simulation,” en, in *Trends in Computational Contact Mechanics*, Springer, Berlin, Heidelberg, 2011, pp. 135–155.
- [44] R. Serban, J. Taves, and Z. Zhou, “Real-Time Simulation of Ground Vehicles on Deformable Terrain,” *Journal of Computational and Nonlinear Dynamics*, vol. 18, no. 8, p. 081 007, Aug. 2023.
- [45] F. Buse, R. Lichtenheldt, and R. Krenn, *SCM - A Novel Approach for Soil Deformation in a Modular Soil Contact Model for Multibody Simulation*. May 2016.
- [46] T. Preclik and U. Rde, “Ultrascale simulations of non-smooth granular dynamics,” *Computational Particle Mechanics*, vol. 2, no. 2, pp. 173–196, Jun. 2015.
- [47] F. A. Tavares and M. E. Plesha, “Discrete element method for modelling solid and particulate materials,” *International Journal for Numerical Methods in Engineering*, vol. 70, no. 4, pp. 379–404, 2007.
- [48] C. Studer, *Numerics of Unilateral Contacts and Friction* (Lecture Notes in Applied and Computational Mechanics), F. Pfeiffer and P. Wriggers, Eds. Berlin, Heidelberg: Springer, 2009, vol. 47.
- [49] J. Hwangbo, J. Lee, and M. Hutter, “Per-Contact Iteration Method for Solving Contact Dynamics,” *IEEE Robotics and Automation Letters*, vol. 3, no. 2, pp. 895–902, Apr. 2018.
- [50] A. M. Castro, F. N. Permenter, and X. Han, “An Unconstrained Convex Formulation of Compliant Contact,” *IEEE Transactions on Robotics*, vol. 39, no. 2, pp. 1301–1320, Apr. 2023.
- [51] K. V. Krishnamurthy et al., *Enabling steep slope walking on Husky using reduced order modeling and quadratic programming*, 2024.
- [52] C. Wang et al., *Quadratic Programming-Based Posture Manipulation and Thrust-vectoring for Agile Dynamic Walking on Narrow Pathways*, 2025.
- [53] K. V. Krishnamurthy et al., *Thruster-Assisted Incline Walking*, 2024.

BIBLIOGRAPHY

- [54] K. V. Krishnamurthy, C. Wang, S. Pitroda, E. Sihite, A. Ramezani, and M. Gharib, *Optimization free control and ground force estimation with momentum observer for a multi-modal legged aerial robot*, 2024.
- [55] S. Pitroda et al., *Capture Point Control in Thruster-Assisted Bipedal Locomotion*, 2024.
- [56] S. Pitroda et al., *Quadratic Programming Optimization for Bio-Inspired Thruster-Assisted Bipedal Locomotion on Inclined Slopes*, 2024.
- [57] S. Pitroda et al., *Enhanced Capture Point Control Using Thruster Dynamics and QP-Based Optimization for Harpy*, 2024.
- [58] S. Pitroda et al., *Conjugate momentum based thruster force estimate in dynamic multimodal robot*, 2024.
- [59] P. Dangol, E. Sihite, and A. Ramezani, "Control of Thruster-Assisted, Bipedal Legged Locomotion of the Harpy Robot," *Frontiers in Robotics and AI*, vol. 8, 2021.
- [60] B. Gupta, E. Sihite, and A. Ramezani, *Conjugate Momentum-Based Estimation of External Forces for Bio-Inspired Morphing Wing Flight*, 2024.
- [61] P. Dangol and A. Ramezani, "Thruster-assisted legged robot control (Conference Presentation)," in *Unmanned Systems Technology XXII*, vol. 11425, International Society for Optics and Photonics, Apr. 2020, p. 1 142 507.
- [62] A. Ramezani and E. Sihite, *Aerobat, A Bioinspired Drone to Test High-DOF Actuation and Embodied Aerial Locomotion*, Dec. 2022.
- [63] E. Sihite and A. Ramezani, *Wake-Based Locomotion Gait Design for Aerobat*, Dec. 2022.
- [64] E. Sihite, P. Ghanem, A. Salagame, and A. Ramezani, *Unsteady aerodynamic modeling of Aerobat using lifting line theory and Wagner's function*, Jul. 2022.
- [65] P. Ghanem, Y. Bicer, D. Erdogmus, and A. Ramezani, "Efficient Modeling of Morphing Wing Flight Using Neural Networks and Cubature Rules," 2021.
- [66] B. Gupta, Y. Shah, T. Liu, E. Sihite, and A. Ramezani, *Banking Turn of High-DOF Dynamic Morphing Wing Flight by Shifting Structure Response Using Optimization*, 2024.
- [67] B. Gupta, E. Sihite, and A. Ramezani, *Modeling and Controls of Fluid-Structure Interactions (FSI) in Dynamic Morphing Flight*, 2024.
- [68] B. Gupta, M. Kim, A. Park, E. Sihite, K. Sreenath, and A. Ramezani, *Estimation of Aerodynamics Forces in Dynamic Morphing Wing Flight*, 2025.

BIBLIOGRAPHY

- [69] A. Salagame et al., *Vision-Guided Loco-Manipulation with a Snake Robot*, 2025.
- [70] S. Jiang, A. Salagame, A. Ramezani, and L. L. Wong, “Hierarchical RL-Guided Large-scale Navigation of a Snake Robot,” in *2024 IEEE International Conference on Advanced Intelligent Mechatronics (AIM)*, Jul. 2024, pp. 1347–1352.
- [71] A. Salagame, Z. Manchester, and R. Tedrake, “Non-Impulsive Contact-Implicit Trajectory Optimization,” *Autonomous Intelligent Machines*, vol. 1, no. 1, p. 100 074, 2024.
- [72] A. Salagame, K. Gangaraju, H. K. Nallaguntla, E. Sihite, G. Schirner, and A. Ramezani, *Loco-Manipulation with Nonimpulsive Contact-Implicit Planning in a Slithering Robot*, 2024.
- [73] A. Salagame, H. K. Nallaguntla, E. Sihite, G. Schirner, and A. Ramezani, *Reinforcement Learning-Based Model Matching to Reduce the Sim-Real Gap in COBRA*, en, Jun. 2024.
- [74] V. Gherold, I. Mandralis, E. Sihite, A. Salagame, A. Ramezani, and M. Gharib, *Self-supervised cost of transport estimation for multimodal path planning*, 2024.
- [75] P. Ghanem, A. Demirkaya, T. Imbiriba, A. Ramezani, Z. Danziger, and D. Erdogmus, *Learning Physics Informed Neural ODEs With Partial Measurements*, 2024.
- [76] A. Salagame, H. Noyes, E. Sihite, A. Kalantari, and A. Ramezani, “Crater Observing Bioinspired Rolling Articulator (COBRA),” *Advanced Intelligent Systems*, vol. n/a, no. n/a, p. 2 500 352, 2024.
- [77] A. Salagame, E. Sihite, and A. Ramezani, *Validation of Tumbling Robot Dynamics with Posture Manipulation for Closed-Loop Heading Angle Control*, 2024.
- [78] I. Mandralis, R. Nemovi, A. Ramezani, R. M. Murray, and M. Gharib, *ATMO: An Aerially Transforming Morphobot for Dynamic Ground-Aerial Transition*, 2025.
- [79] C. Wang et al., *Dynamic Quadrupedal Legged and Aerial Locomotion via Structure Repurposing*, 2025.
- [80] C. Wang, A. Viswanathan, E. Sihite, and A. Ramezani, *Guiding Energy-Efficient Locomotion through Impact Mitigation Rewards*, 2025.
- [81] C. Wang and A. Ramezani, *Thruster-Enhanced Locomotion: A Decoupled Model Predictive Control with Learned Contact Residuals*, 2025.
- [82] W. Ouyang, C. Li, W. Liang, Q. Ren, and P. Li, “Motion Control of a Snake Robot via Cerebellum-inspired Learning Control,” in *2018 IEEE 14th International Conference on Control and Automation (ICCA)*, Jun. 2018, pp. 1010–1015.

BIBLIOGRAPHY

- [83] Z. Bing, L. Cheng, G. Chen, F. Röhrbein, K. Huang, and A. Knoll, “Towards autonomous locomotion: CPG-based control of smooth 3D slithering gait transition of a snake-like robot,” *Bioinspiration & Biomimetics*, vol. 12, no. 3, p. 035 001, Apr. 2017.
- [84] H. Fukushima, T. Yanagiya, Y. Ota, M. Katsumoto, and F. Matsuno, “Model Predictive Path-Following Control of Snake Robots Using an Averaged Model,” *IEEE Transactions on Control Systems Technology*, vol. 29, no. 6, pp. 2444–2456, Nov. 2021.
- [85] H. Li, H. Wang, L. Cui, J. Li, Q. Wei, and J. Xia, “Design and Experiments of a Compact Self-Assembling Mobile Modular Robot with Joint Actuation and Onboard Visual-Based Perception,” *Applied Sciences*, vol. 12, no. 6, p. 3050, Jan. 2022.
- [86] A. Crespi and A. J. Ijspeert, “Online Optimization of Swimming and Crawling in an Amphibious Snake Robot,” *IEEE Transactions on Robotics*, vol. 24, no. 1, pp. 75–87, Feb. 2008.
- [87] P. Liljebäck, K. Y. Pettersen, Ø. Stavdahl, and J. T. Gravdahl, “A review on modelling, implementation, and control of snake robots,” *Robotics and Autonomous Systems*, vol. 60, no. 1, pp. 29–40, Jan. 2012.
- [88] K. Fujita, H. Karaca, and H. Nagai, “Parametric Study of Mars Helicopter for Pit Crater Exploration,” in *AIAA Scitech 2020 Forum*, American Institute of Aeronautics and Astronautics.
- [89] M. Radotich, S. Withrow-Maser, Z. deSouza, S. Gelhar, and H. Gallagher, “A Study of Past, Present, and Future Mars Rotorcraft,” Virtual.
- [90] P. Zhao, X. Gao, Z. Yan, Y. Li, J. Wu, and Z. Deng, “Investigation of Aerodynamic Performance of Coaxial Rotors for Mars Rotorcraft,” in *2023 IEEE International Conference on Mechatronics and Automation (ICMA)*, Aug. 2023, pp. 1275–1280.
- [91] L. Young, E. Aiken, V. Gulick, R. Mancinelli, and G. Briggs, “Rotorcraft as Mars Scouts,” in *Proceedings, IEEE Aerospace Conference*, vol. 1, Mar. 2002, 1–378 vol.1.
- [92] J. Zhao, J. Huang, M. D. Kraft, L. Xiao, and Y. Jiang, “Ridge-like lava tube systems in southeast Tharsis, Mars,” *Geomorphology*, vol. 295, pp. 831–839, Oct. 2017.
- [93] K. E. Williams, C. P. McKay, O. B. Toon, and J. W. Head, “Do ice caves exist on Mars?” *Icarus*, vol. 209, no. 2, pp. 358–368, Oct. 2010.

BIBLIOGRAPHY

- [94] G. Bellegarda and K. Byl, “An Online Training Method for Augmenting MPC with Deep Reinforcement Learning,” in *2020 IEEE/RSJ International Conference on Intelligent Robots and Systems (IROS)*, Oct. 2020, pp. 5453–5459.
- [95] E. Su et al., *Sim2Real Manipulation on Unknown Objects with Tactile-based Reinforcement Learning*, Mar. 2024.
- [96] N. Rudin, D. Hoeller, M. Bjelonic, and M. Hutter, “Advanced Skills by Learning Locomotion and Local Navigation End-to-End,” in *2022 IEEE/RSJ International Conference on Intelligent Robots and Systems (IROS)*, Oct. 2022, pp. 2497–2503.
- [97] A. B. Kordabad, H. N. Esfahani, A. M. Lekkas, and S. Gros, “Reinforcement Learning based on Scenario-tree MPC for ASVs,” in *2021 American Control Conference (ACC)*, May 2021, pp. 1985–1990.
- [98] X. Liu et al., “Large-Scale Autonomous Flight With Real-Time Semantic SLAM Under Dense Forest Canopy,” *IEEE Robotics and Automation Letters*, vol. 7, no. 2, pp. 5512–5519, Apr. 2022.
- [99] S. B. Laina et al., *Scalable Autonomous Drone Flight in the Forest with Visual-Inertial SLAM and Dense Submaps Built without LiDAR*, Mar. 2024.
- [100] L. Jarin-Lipschitz, X. Liu, Y. Tao, and V. Kumar, “Experiments in Adaptive Replanning for Fast Autonomous Flight in Forests,” in *2022 International Conference on Robotics and Automation (ICRA)*, May 2022, pp. 8185–8191.
- [101] W. Yang, G. Wang, and Y. Shen, “Perception-Aware Path Finding and Following of Snake Robot in Unknown Environment,” in *2020 IEEE/RSJ International Conference on Intelligent Robots and Systems (IROS)*, Oct. 2020, pp. 5925–5930.
- [102] J. Lee, X. Wu, S. J. Lee, and M. W. Mueller, *Autonomous Flight through Cluttered Outdoor Environments Using a Memoryless Planner*, Mar. 2021.
- [103] A. Ramezani, S.-J. Chung, and S. Hutchinson, “A biomimetic robotic platform to study flight specializations of bats,” *Science Robotics*, vol. 2, no. 3, eaal2505, Feb. 2017.
- [104] A. Ramezani, X. Shi, S.-J. Chung, and S. Hutchinson, “Bat Bot (B2), a biologically inspired flying machine,” in *2016 IEEE International Conference on Robotics and Automation (ICRA)*, Stockholm, Sweden: IEEE, May 2016, pp. 3219–3226.

BIBLIOGRAPHY

- [105] J. Hoff, A. Ramezani, S.-J. Chung, and S. Hutchinson, “Optimizing the structure and movement of a robotic bat with biological kinematic synergies,” *The International Journal of Robotics Research*, vol. 37, no. 10, pp. 1233–1252, Sep. 2018.
- [106] A. Ramezani, X. Shi, S.-J. Chung, and S. Hutchinson, “Bat Bot (B2), an Articulated-Winged Bat Robot,”
- [107] A. Yamano, Y. Ikeda, K. Imai, and M. Chiba, “Efficient rolling motion for snake-like robots utilizing center of gravity shift,” *Mechatronics*, vol. 94, p. 103 024, Oct. 2023.
- [108] B. A. Elsayed, T. Takemori, M. Tanaka, and F. Matsuno, “Mobile Manipulation Using a Snake Robot in a Helical Gait,” *IEEE/ASME Transactions on Mechatronics*, vol. 27, no. 5, pp. 2600–2611, Oct. 2022.
- [109] F. Qin et al., “Design and Experiments of Snake Robots with Docking Function,” in *2022 IEEE/RSJ International Conference on Intelligent Robots and Systems (IROS)*, Oct. 2022, pp. 1208–1214.
- [110] R. Ariizumi and F. Matsuno, “Dynamic Analysis of Three Snake Robot Gaits,” *IEEE Transactions on Robotics*, vol. 33, no. 5, pp. 1075–1087, Oct. 2017.
- [111] J. Hoff, A. Ramezani, S.-J. Chung, and S. Hutchinson, “Synergistic Design of a Bio-Inspired Micro Aerial Vehicle with Articulated Wings,” in *Robotics: Science and Systems XII*, Robotics: Science and Systems Foundation, 2016.
- [112] A. Ramezani, P. Dangol, E. Sihite, A. Lessieur, and P. Kelly, “Generative Design of NU’s Husky Carbon, A Morpho-Functional, Legged Robot,” *arXiv:2104.05834 [cs]*, Apr. 2021.
- [113] A. Duivon, P. Kirsch, B. Mauboussin, G. Mougard, J. Woszczyk, and F. Sanfilippo, “The Redesigned Serpens, a Low-Cost, Highly Compliant Snake Robot,” *Robotics*, vol. 11, no. 2, p. 42, Apr. 2022.
- [114] A. Western, M. Haghshenas-Jaryani, and M. Hassanalain, “Golden wheel spider-inspired rolling robots for planetary exploration,” *Acta Astronautica*, vol. 204, pp. 34–48, Mar. 2023.
- [115] Y. Tian, X. Kong, K. Xu, and X. Ding, “Multi-Loop Rover: A Kind of Modular Rolling Robot Constructed by Multi-Loop Linkages,” *Journal of Mechanisms and Robotics*, vol. 13, no. 1, Oct. 2020.
- [116] J. Seetohul and M. Shafiee, “Snake Robots for Surgical Applications: A Review,” *Robotics*, vol. 11, no. 3, p. 57, Jun. 2022.

BIBLIOGRAPHY

- [117] J. Delaune et al., *Mid-Air Helicopter Delivery at Mars Using a Jetpack*, Mar. 2022.
- [118] J. Hoff, U. Syed, A. Ramezani, and S. Hutchinson, “Trajectory planning for a bat-like flapping wing robot,” in *2019 IEEE/RSJ International Conference on Intelligent Robots and Systems (IROS)*, Nov. 2019, pp. 6800–6805.
- [119] S. Liu et al., “Planning Dynamically Feasible Trajectories for Quadrotors Using Safe Flight Corridors in 3-D Complex Environments,” *IEEE Robotics and Automation Letters*, vol. 2, no. 3, pp. 1688–1695, Jul. 2017.
- [120] A. Saez, M. Manzo, and M. Ciarcià, “Mars Drone Configurations And Approaches to Rotor Design: A Review,” American Society of Mechanical Engineers Digital Collection, Jan. 2022.
- [121] A. Lessieur, E. Sihite, P. Dangol, A. Singhal, and A. Ramezani, “Mechanical design and fabrication of a kinetic sculpture with application to bioinspired drone design,” in *Unmanned Systems Technology XXIII*, vol. 11758, SPIE, Apr. 2021, pp. 21–27.
- [122] S. Sareh et al., “Bio-inspired tactile sensor sleeve for surgical soft manipulators,” in *2014 IEEE International Conference on Robotics and Automation (ICRA)*, May 2014, pp. 1454–1459.
- [123] M. Camurri et al., “Probabilistic Contact Estimation and Impact Detection for State Estimation of Quadruped Robots,” *IEEE Robotics and Automation Letters*, vol. 2, no. 2, pp. 1023–1030, Apr. 2017.
- [124] S. R. Taal, H. Yamada, and S. Hirose, “3 axial force sensor for a semi-autonomous snake robot,” in *2009 IEEE International Conference on Robotics and Automation*, May 2009, pp. 4057–4062.
- [125] N. Chavan-Dafie and A. Rodriguez, “Regrasping by Fixtureless Fixturing,” in *2018 IEEE 14th International Conference on Automation Science and Engineering (CASE)*, Aug. 2018, pp. 122–129.
- [126] J. Wanner, E. Sihite, A. Ramezani, and M. Gharib, *Model Predictive Loitering and Trajectory Tracking of Suspended Payloads in Cable-Driven Balloons Using UGVs*, Jun. 2022.
- [127] K. Bouyarmane and A. Kheddar, “On the dynamics modeling of free-floating-base articulated mechanisms and applications to humanoid whole-body dynamics and control,” in *2012 12th IEEE-RAS International Conference on Humanoid Robots (Humanoids 2012)*, Nov. 2012, pp. 36–42.

BIBLIOGRAPHY

- [128] Z. Zhang, H. Jiang, and H. Singh, *NeuFlow: Real-time, High-accuracy Optical Flow Estimation on Robots Using Edge Devices*, Mar. 2024.
- [129] J. Sastra, S. Chitta, and M. Yim, “Dynamic Rolling for a Modular Loop Robot,” *The International Journal of Robotics Research*, vol. 28, no. 6, pp. 758–773, Jun. 2009.
- [130] A. Tasora et al., “Chrono: An Open Source Multi-Physics Dynamics Engine,” *Proceedings of the 1st Joint International Conference on Multibody System Dynamics*, pp. 19–49, 2016.
- [131] A. C. B. de Oliveira and A. Ramezani, “Thruster-assisted Center Manifold Shaping in Bipedal Legged Locomotion,” in *2020 IEEE/ASME International Conference on Advanced Intelligent Mechatronics (AIM)*, Jul. 2020, pp. 508–513.
- [132] E. Sihite, B. Mottis, P. Ghanem, A. Ramezani, and M. Gharib, “Efficient Path Planning and Tracking for Multi-Modal Legged-Aerial Locomotion Using Integrated Probabilistic Road Maps (PRM) and Reference Governors (RG),” in *2022 IEEE 61st Conference on Decision and Control (CDC)*, Dec. 2022, pp. 764–770.
- [133] R. Oung, A. Ramezani, and R. D’Andrea, “Feasibility of a Distributed Flight Array,” in *Proceedings of the 48th IEEE Conference on Decision and Control (CDC) held jointly with 2009 28th Chinese Control Conference*, Dec. 2009, pp. 3038–3044.
- [134] F. Sanfilippo, J. Azpiazu, G. Marafioti, A. A. Transeth, Ø. Stavdahl, and P. Liljebäck, “Perception-Driven Obstacle-Aided Locomotion for Snake Robots: The State of the Art, Challenges and Possibilities †,” *Applied Sciences*, vol. 7, no. 4, p. 336, Apr. 2017.
- [135] D. Li, B. Zhang, R. Law, E. Q. Wu, and X. Xu, “Error constrained-Formation path-following method with disturbance elimination for multi-snake robots,” *IEEE Transactions on Industrial Electronics*, pp. 1–10, 2023.
- [136] D. Ramesh, Q. Fu, and C. Li, *SenSnake: A snake robot with contact force sensing for studying locomotion in complex 3-D terrain*, Jun. 2022.
- [137] Z. JANOSI, “The Analytical Determination of Drawbar Pull as A Function of Slip for Trackcd Vehicles in Deformable Soils,” *International Society for Terrain-Vehicle Systems, 1st Int. Conf.*, vol. 707, 1961.
- [138] C. Campos, R. Elvira, J. J. G. Rodríguez, J. M. M. Montiel, and J. D. Tardós, “ORB-SLAM3: An Accurate Open-Source Library for Visual, Visual-Inertial and Multi-Map SLAM,” *IEEE Transactions on Robotics*, vol. 37, no. 6, pp. 1874–1890, Dec. 2021.